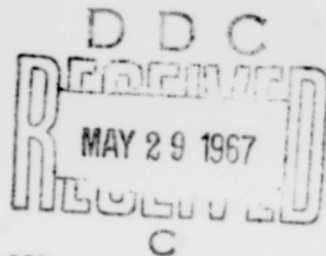


AD 655383

# APPLICATION OF GROUND TEST DATA TO REENTRY VEHICLE DESIGN

Alfred C. Thomas  
and  
Andrew Perlbachs

THE BOEING COMPANY



TECHNICAL REPORT AFFDL-TR-66-229

January 1967

Distribution of this document is unlimited.

RECEIVED

AUG 3 1967

CFSTI

Air Force Flight Dynamics Laboratory  
Research and Technology Division  
Air Force Systems Command  
Wright-Patterson Air Force Base, Ohio

138

NOTICES

When Government drawings, specifications, or other data are used for any purpose other than in connection with a definitely related Government procurement operation, the United States Government thereby incurs no responsibility nor any obligation whatsoever, and the fact that the Government may have formulated, furnished, or in any way supplied the said drawings, specifications, or other data, is not to be regarded by implication or otherwise as in any manner licensing the holder or any other person or corporation, or conveying any rights or permission to manufacture, use, or sell any patented invention that may in any way be related thereto.

ADDITIONAL TO

WHITE SECTION

GRAY SECTION

UNCLASSIFIED

CLASSIFIED

DATE: \_\_\_\_\_

AVAIL. AND IN SPECIAL: \_\_\_\_\_

Copies of this report should not be returned to the Research and Technology Division unless return is required by security considerations, contractual obligations, or notice on a specific document.

# **APPLICATION OF GROUND TEST DATA TO REENTRY- VEHICLE DESIGN**

**Alfred C. Thomas  
and  
Andrew Perlbachs**

**Distribution of this document is unlimited.**

## ABSTRACT

Methods and procedures have been developed for extrapolating ground-test aerothermodynamic data to flight conditions for four geometric elements. These elements are a sharp unyawed delta wing, deflected control surfaces in compression and expansion, surface roughness elements typified by shallow convex surface waves and rectangular grooves, and a yawed circular cylinder intersecting a sharp flat plate. Graphs and charts are provided for rapid numerical computation of factors to be used in extrapolating the wind-tunnel data for these geometric elements to flight conditions. An evaluation of the simulation capabilities of operational hypersonic ground facilities is also included.

## FOREWORD

This report was prepared by the Aerospace Group of The Boeing Company, Seattle, Washington, under USAF Contract AF33(615)-2516, Mr. A. L. Nagel, Program Manager. The contract was initiated under Program Element 62405334, Project No. 1366, Task No. 136607, BPSN 5(61136607-62405334). The work was administered under the direction of the Air Force Flight Dynamics Laboratory, Research and Technology Division, Wright-Patterson Air Force Base, Ohio, Mr. Richard D. Neumann, Air Force Project Engineer.

This report covers work conducted between June 1965 and December 1966.

The authors acknowledge Barbara J. Safley for her exceptional effort in assembling and checking the charts and curves contained in this report.

The manuscript was released by the authors for publication as an RTD technical report in January 1967.

This technical report has been reviewed and is approved.

*Philip P. Antonatos*

---

PHILIP P. ANTONATOS  
Chief, Flight Mechanics Division  
Air Force Flight Dynamics Laboratory

## TABLE OF CONTENTS

	<u>Page</u>
I. INTRODUCTION	1
II. GROUND-FACILITY FLIGHT CONDITION SIMULATION CAPABILITY	3
1. GROUND-TEST FACILITIES	4
a. Energy Simulation	4
b. Reynolds Number Simulation	5
c. Lewis Number and Knudsen Number Simulation	6
2. REAL-GAS EFFECTS IN GROUND FACILITY NOZZLE FLOW	7
III. EXTRAPOLATION METHODS	9
1. BASIC EXTRAPOLATION PROCEDURE	9
2. SHARP DELTA WINGS	11
a. Laminar Flow	12
b. Turbulent Flow	13
c. Off-Centerline	14
d. Dissimilar Flow-Field Effects	15
3. DEFLECTED CONTROL SURFACES	15
a. Compression Surfaces	16
b. Expansion Surfaces	17
4. INTERFERENCE GEOMETRIES	20
a. Swept-Cylinder Stagnation-Line Interference Heating	21
b. Dissimilar Flow Fields	25
5. ROUGHNESS ELEMENTS	26
a. Shallow Convex Waves	27
b. Rectangular Grooves	28
6. CHEMICAL NONEQUILIBRIUM EFFECTS ON EXTRAPOLATION FACTORS	29
a. Blunt Bodies	30
b. Slender Bodies	31
c. Effects of Catalytic Wall	32
IV. CONCLUDING REMARKS	33
APPENDIX A HEAT TRANSFER PREDICTION METHOD FOR SHARP UNYAWED DELTA WINGS	79

## TABLE OF CONTENTS (Concluded)

	<u>Page</u>
APPENDIX B    METHOD OF FLOW FIELD SOLUTION IN PROXIMITY TO THE CENTERLINE FOR SHARP UNYAWED DELTA WINGS	87
APPENDIX C    METHOD OF SPANWISE FLOW FIELD SOLUTION FOR SHARP UNYAWED DELTA WINGS	104
REFERENCES	119

## LIST OF ILLUSTRATIONS

### Figure

1.    Velocity Simulation in Ground Facilities	36
2.    Energy Simulation in Ground Facilities	37
3.    Free-Stream Reynolds Number Simulation in Ground Facilities	38
4.    Reynolds Number and Inviscid Mach Number Comparison on a Sharp Flat Plate	39
5.    Real-Gas Effects on Reynolds Number for Wedges and Sharp Unyawed Cones	40
6.    Orbital Reentry Corridor for Lifting Vehicles	42
7.    Sharp Delta Wing Laminar Extrapolation Factors for Air and Nitrogen Ground Facilities	43
8.    Sharp Delta Wing Laminar Extrapolation Factors for Helium Ground Facilities	44
9.    Sharp Delta Wing Centerline Laminar Heating for Flight Conditions	45
10.   Sharp Delta Wing Centerline Reynolds Number Distribution	48
11.   Reference Reynolds Number for Air and Nitrogen Ground Facilities	51
12.   Reference Reynolds Number for Flight Conditions	52
13.   Reynolds Number Function	54
14.   Sharp Delta Wing Spanwise Laminar Extrapolation Factors	55
15.   Sharp Delta Wing Centerline Sonic Flow Conditions	56

## LIST OF ILLUSTRATIONS (Continued)

<u>Figure</u>	<u>Page</u>
16. Maximum Heating Rate Increases for Positively Deflected Control Surfaces in Air and Nitrogen Flows	57
17. Maximum Heating Rate Increases for Positively Deflected Control Surfaces in Helium Ground Facilities	58
18. Pressure Distribution on Negatively Deflected Control Surfaces in Air and Nitrogen Flows	59
19. Compressibility Factor-Temperature Product for Sharp Flat Plates at Angle of Attack	61
20. Displacement-Thickness Heating Parameters for Sharp Flat Plates	63
21. Heating Distribution on Negatively Deflected Control Surfaces in Air and Nitrogen Flows	66
22. Interference Geometry Laminar Extrapolation Factors for Air and Nitrogen Ground Facilities	68
23. Interference Geometry Laminar Extrapolation Factors for Helium Ground Facilities	69
24. Interference Geometry Turbulent Extrapolation Factors for Air and Nitrogen Ground Facilities	70
25. Interference Geometry Maximum Laminar Heating Rate Ratios for Flight Conditions	71
26. Interference Geometry Maximum Turbulent Heating Rate Ratios for Flight Conditions	72
27. Boundaries Between Regions of Attached and Detached Shock Waves for Interference Geometries	73
28. Shallow Surface Wave Laminar Heating	74
29. Maximum Laminar Heating Near Rectangular Grooves	78
B1 Similarity Parameter for Sharp Unyawed Cones	96
B2 Similarity Parameter for Sharp Unyawed Delta Wings	97
B3 Correlation of Similarity Parameter for Sharp Delta Wings at High Angles of Attack	98
B4 Effect of Changes in Similarity Parameter on Centerline Shock Wave Geometry for Sharp Delta Wings	99
B5 Real-Gas Correction to Similarity Parameter for Sharp Delta Wings	100

LIST OF ILLUSTRATION (Concluded)

<u>Figure</u>		<u>Page</u>
B6	Shock Layer Pressure Ratio for Sharp Unyawed Cones	101
B7	Shock Layer Pressure Ratio for Sharp Unyawed Delta Wings	101
B8	Comparison of Surface Pressure with Modified Newtonian Values	102
B9	Correlation of Divergence Parameter for Sharp Delta Wings at High Angle of Attack	103
B10	Divergence Parameter for Sharp Delta Wings at Low and Intermediate Angles of Attack	103
C1	Correlation for Leading Edge Streamline Angles at High Angles of Attack	111
C2	Spanwise Streamline Angle Distribution at High Angles of Attack	112
C3	Spanwise Pressure Distribution at High Angles of Attack	112
C4	Correlation for Spanwise Streamline Angles at High Angles of Attack	113
C5	Correlation for Spanwise Pressure at High Angles of Attack	114
C6	Lower Surface Flow Field Regimes	115
C7	Spanwise Streamline Angle Profiles	116
C8	Spanwise Pressure Profiles	117
C9	Spanwise Location of Dividing Streamline	118

## SYMBOLS

$a$	local speed of sound
$a^*$	speed of sound at leading edge of delta wing
$b$	span width
$b_{eq}$	equivalent distance
$c$	specific heat of model skin
$C$	constant; coefficient; correction factor
$C_L$	lift coefficient
$c_P$	specific heat at constant pressure
$C_P$	pressure coefficient
$c_v$	specific heat at constant volume
$D$	diffusion coefficient
$\bar{E}$	momentum thickness parameter
$f$	streamline divergence parameter due to transverse pressure gradients
$F$	extrapolation factor
$F_x$	equivalent distance function, equation (A4c)
$h$	heat-transfer coefficient based on temperature, $\dot{q}/(T_{aw} - T_w)$
$h_{ref}$	stagnation point heat-transfer coefficient on a hemisphere of 1 foot radius
$h_\Lambda$	stagnation line heat-transfer coefficient on an infinite cylinder of sweep $\Lambda$
$\bar{h}$	normalized heat-transfer coefficient
$H$	heat-transfer coefficient based on enthalpy, $\dot{q}/(i_{aw} - i_w)$
$i$	enthalpy
$i_o$	total enthalpy
$i_D$	enthalpy absorbed in dissociation
$\bar{i}$	ratio of total wind tunnel enthalpy to total flight enthalpy at the same Mach number
$J$	streamwise pressure gradient parameter
$k$	thermal conductivity
$K$	constant

## SYMBOLS (Continued)

<b>Kn</b>	Knudsen number
<b><math>K_{SL}</math></b>	parameter defined by equation (25b)
<b><math>l</math></b>	characteristic body length
<b>Le</b>	Lewis number
<b><math>\mathcal{L}</math></b>	Lewis number function
<b>m</b>	exponent
<b><math>\dot{m}</math></b>	mass flow rate
<b>M</b>	Mach number
<b>n</b>	streamline divergence parameter, equation (B15); exponent
<b>[O]</b>	on the order of magnitude of
<b>P</b>	pressure
<b>Pr</b>	Prandtl number
<b><math>\dot{q}</math></b>	heating rate
<b><math>\hat{q}</math></b>	dynamic pressure
<b><math>q'</math></b>	pressure gradient function
<b>Q</b>	streamwise pressure gradient profile parameter
<b>r</b>	radius; flow divergence parameter related to body geometry
<b>R</b>	roughness element height; gas constant for particular gas
<b>Re</b>	Reynolds number, $\rho u l / \mu$
<b><math>R_r</math></b>	local reference Reynolds number defined by equation (A3)
<b><math>(R_r)_{ref}</math></b>	reference Reynolds number on a sharp flat plate at $\alpha = 20^\circ$ , $x = 1$ foot
<b>S</b>	similarity parameter, equation (B1); surface area
<b>T</b>	temperature
<b>u</b>	centerline surface velocity on sharp delta wing
<b>V</b>	velocity
<b>W</b>	roughness element width; weight
<b>x</b>	coordinate along body surface; surface distance
<b>x, y, z</b>	Cartesian coordinates
<b><math>x_{eq}</math></b>	heat-transfer equivalent distance
<b>y</b>	coordinate normal to body surface

### SYMBOLS (Continued)

Z	compressibility factor, $P/\rho RT$
$\alpha$	angle of attack; cone semi-vertex angle
$\beta$	angle defined as $(90^\circ - \Lambda)$ ; velocity gradient parameter
$\gamma$	ratio of specific heats, $c_p/c_v$
$\delta$	flow-deflection angle; boundary-layer thickness
$\delta^*$	boundary-layer displacement thickness
$\Delta$	finite increment operator; shock standoff distance
$\Delta F$	expansion surface turning angle
$\Delta x$	distance from control surface hinge line, $x - x_{HL}$
$\epsilon$	shock-layer thickness
$\eta$	coordinate in plane of sharp delta wing surface normal to centerline
$\theta$	shock wave angle; local streamline angle on sharp delta wing surface measured with respect to the centerline
$\theta^*$	delta wing leading edge streamline angle measured with respect to the centerline
$\lambda$	molecular mean free path
$\Lambda$	angle of sweep
$\mu$	absolute viscosity
$\nu$	Prandtl-Meyer angle
$\xi$	coordinate parallel to sharp delta wing centerline
$\rho$	density
$\rho_r \mu_r$	reference density-viscosity product
$\sigma_r$	Prandtl number evaluated at enthalpy and pressure corresponding to $\rho_r \mu_r$
$\Upsilon$	delta wing flow parameter, $[a^*/u] \sec \Lambda$
$\phi$	local ray angle on sharp delta wing surface

#### Subscripts

atm	evaluated at sea level condition
aw	adiabatic wall
C	cone
d	leading edge shock detachment

## SYMBOLS (Continued)

e	at boundary-layer edge
eff	effective
eq	equivalent
f	frozen
FLT	at flight conditions
HL	at hinge line
i	initial; at arbitrary location; extrapolation on enthalpy
iM	extrapolation on Mach number and enthalpy
L	laminar
le, LE	leading edge
max	maximum
min	minimum
M	extrapolation on Mach number
mN	Boeing modified Newtonian pressure method
n	in normal direction; with effect of streamline divergence
n = 0	without effect on streamline divergence
o	at stagnation conditions
P	pressure
r	evaluated at enthalpy and pressure corresponding to conditions used to evaluate $\rho_r \mu_r$
ref	pertaining to a reference quantity
R	relative
R <sub>r</sub>	extrapolation from laminar to turbulent conditions
s	streamwise; conditions on downstream side of shock
sm	smooth
SL	on stagnation line
SP	at stagnation point
t	in tangential direction; temperature
te	at trailing edge
T	turbulent
w	at wall

### SYMBOLS (Concluded)

WT	at wind tunnel conditions
x	at distance x; distance correction
$\Lambda$	based on geometric sweep angle; at stagnation line of infinite swept cylinder
$\phi$	based on angular location; extrapolation of spanwise heating
0	at Mach number zero
1	at condition 1
2	at condition 2; downstream of shock wave
$\infty$	free-stream or undisturbed condition

#### Superscripts

$\zeta$	exponent in equation (C5)
*	at reference temperature; at leading edge; sonic conditions

**BLANK PAGE**

## SECTION I

### INTRODUCTION

Full-scale free-flight tests of maneuverable reentry vehicles and hypersonic cruise vehicles are highly desirable, since this is the only way in which all of the flow conditions influencing design parameters can be encountered simultaneously. In most cases, the cost of such an approach is prohibitive. As a result, the majority of all hypersonic aerothermodynamic data used in configuration design are obtained in ground facilities (i. e., wind tunnels, shock tunnels, hotshot tunnels, helium tunnels, and shock tubes) that cannot simultaneously simulate all of the conditions encountered in flight. The effects of simulation deficiencies in ground facilities on the observed aerothermodynamic characteristics of maneuverable reentry configurations are discussed in references 1 and 2. Hypersonic cruise vehicles, though not subjected to as severe an environment as the reentry vehicle, will encounter some partial simulation problems, particularly in regions of mutual flow-field interference (e. g., at the engine cowl lip, or at wing-body control surface intersections).

Successful design of hypersonic vehicles is dependent upon the development of analytic methods and procedures that can account for the lack of simulation in ground-test facilities and enable confident application of ground-test data to reentry vehicle design. This report presents an evaluation of the simulation capability of ground facilities available for development testing of scaled reentry and hypersonic cruise vehicles. Aerodynamic parameters such as Reynolds number, Mach number, Lewis number, and Knudsen number have been evaluated for ground-facility stream-flow conditions and are presented in Section II. These parameters are used in conjunction with velocity, total enthalpy, and free-stream temperature to illustrate the simulation limitations of these facilities. In the present analysis, the characteristics and the simulation capability of hypervelocity gun facilities have not been included since very few heat-transfer and pressure distribution investigations using complex configurations have been obtained in this type of facility.

Extrapolation methods and procedures for the aerothermodynamic analysis of four geometric elements are presented in Section III. These elements include a sharp unyawed delta wing, deflected control surfaces in compression and expansion, surface roughness elements typified by shallow convex waves and rectangular grooves, and a yawed circular cylinder intersecting a sharp flat plate. Extrapolation charts and curves are presented in this section that give numerical results. Extrapolation factors are presented directly, or a combination of factors is presented that will allow simple formulation of the extrapolation factor. The use of the charts, and of the extrapolation procedure is also explained in this section. The flight conditions are represented by a reentry corridor defined by a wing loading parameter,  $W/SC_L$ , range between 50 and 500 and by a flight envelope between  $10^{-2}$  and  $10^{-6}$  atmospheres at a free-stream Mach number of 10.

The theoretical method used to determine sharp-delta-wing centerline heat-transfer is outlined in Appendix A. A new flow-field method was developed to determine real-gas and leading-edge sweep-angle effects on flow-field gas properties at the centerline of a sharp delta wing. This method is presented in Appendix B. Existing sharp-delta-wing spanwise flow-field methods for angles of attack less than about 15 degrees (reference 18) and greater than about 45 degrees (reference 36) have been extended to the intermediate angle of attack range between these limits. The extended method bridges the analytic methods shown in references 18 and 36, and postulates a parting line theory for some conditions in the intermediate angle of attack range that predicts maximum heat transfer will occur on the delta wing surface inboard of the leading edge and outboard of the centerline. This method is presented in Appendix C.

## SECTION II

### GROUND-FACILITY FLIGHT CONDITION SIMULATION CAPABILITY

In the past few years, continual improvement in material capability and cooling techniques has allowed wind-tunnel designers to extend the thermal energy and maximum pressure capability of wind tunnels, shock tunnels, and hotshot tunnels. Nevertheless, total enthalpy deficiencies still exist in these types of facilities which affect flow-field and boundary-layer characteristics, heat transfer, and non-dimensional parameters such as Reynolds number, Prandtl number, and Lewis number.

Hypervelocity gun facilities are being used to simulate high enthalpy effects on models in a free-flight environment. The models generally are very small and simple, however, and extensive local measurements of pressure and heat transfer are not possible at this time. The present analysis does not include this type of ground facility.

A discussion of the free-stream environment that can be obtained in air-nitrogen tunnels having test-section diameters on the order of four feet or greater and in helium tunnels with test-section diameters of about two feet is presented in this section. The operating conditions for air and nitrogen tunnels considered in the present analysis are characteristic of Tunnels B, C, and F at Arnold Engineering Developmental Center (reference 3) and of the shock tunnel at Cornell Aeronautical Laboratory (reference 4). Operating characteristics for helium tunnels pertain to the facility at NASA-Langley<sup>1</sup>.

Shock-tube diameters do not approach the test-section diameters of the facilities described above. Their range of operation, however, is presented for comparison with the range of operation in air, nitrogen, and helium facilities. The environmental range of shock tubes has been determined for the present analysis using data from reference 5.

Effects of total enthalpy deficiencies on some nondimensional parameters are presented in this section. A qualitative summary of real-gas effects on free-stream gas properties in ground-facility test sections is also presented.

---

<sup>1</sup> These characteristics were obtained during a facility tour at the 25th Supersonic Tunnel Association Meeting at NASA-Langley Research Center, Langley Field, Virginia, May 1966.

## 1. GROUND-TEST FACILITIES

### a. Energy Simulation

The ability to simultaneously simulate all of the parameters important to hypersonic reentry in ground facilities, and to provide reliable aerothermodynamic data is discussed in references 1 and 2. It is shown in those two references that hypersonic ground facilities which employ air or nitrogen as a test medium cannot simulate the energy levels associated with reentry vehicles. Shock tubes can achieve flow velocities equivalent to high-speed flight conditions but at the expense of a loss in Mach number and free-stream gas property simulation. Helium tunnels, on the other hand, have the advantage of achieving hypersonic Mach numbers with stagnation temperatures on the order of ambient temperature. The helium facility, however, simulates neither the high enthalpies, nor the real-gas effects associated with flight.

These conditions are illustrated in figure 1 in terms of free-stream Mach number,  $M_\infty$ , and free-stream velocity,  $V_\infty$ . In this figure, free-stream Mach number is used as a measure of compressibility effects. Duplication of this parameter is required to insure a realistic shock-wave geometry. Free-stream velocity is indicative of the kinetic energy of the stream. This figure indicates clearly that present ground facilities cannot simultaneously duplicate the high Mach number and velocity encountered in the region of most critical reentry heating, which occurs within the orbital reentry corridor at velocities between about 17,000 and 22,000 fps and at Mach numbers between 16 and 23.

The kinetic and thermal energy capability of ground facilities provides a criterion that allows separation of these facilities into three sub-groups. Hypersonic air and nitrogen tunnels form the first group in which a bulk of all aerothermodynamic design testing is accomplished. Hypersonic helium tunnels form the second group, and shock tubes the third. The energy capability of these three groups of tunnels with respect to the energy available during reentry is best illustrated by a figure which shows the relationship between total energy and thermal energy. This is done in figure 2 where total enthalpy,  $i_0$ , representing the sum of the kinetic and thermal energy of the flow, is shown in terms of the free-stream temperature,  $T_\infty$ .

The energy capability of hotshot tunnels, shock tunnels, and conventional wind tunnels is illustrated by the region in the center of the figure. This region is bounded at low free-stream temperatures by the onset of gas liquefaction in the test section. This boundary is approximate, in that it corresponds to free-stream pressures and temperatures characteristic of the facilities being analyzed. The upper boundary is defined by the total enthalpy available in these facilities. Combustion-driven shock tunnels reach energy levels in excess of 4,000 Btu/lbm, whereas, hotshot tunnels and "regular" shock tunnels (i.e., those using inert gases for the driver gas) are able to reach energy levels on the order of 2,800 Btu/lbm. (Combustion-driven shock tunnels are separated

from "regular" shock tunnels because stream-flow characteristics for these facilities are not well defined for all operating conditions.) Conventional wind tunnels can obtain total enthalpies on the order of 1,000 Btu/lbm. It is indicated in this figure that the flight environment can be simulated by the hotshot and shock tunnels up to a free-stream velocity of about 11,000 fps.

Extremely low free-stream static temperatures (i. e. , approximately 2° to 10° Rankine) are characteristic of helium tunnels. A lower limit is imposed on the free-stream temperature that is based on liquefaction. Total enthalpies above ambient levels can be obtained in this type facility by heating the helium. However, the majority of present-day operational helium facilities operate with total enthalpies which correspond to ambient temperatures.

Shock tubes can reach energy levels on the order of 30,000 Btu/lbm and velocities on the order of 24,000 fps. This group of facilities, however, does not lend itself to development tests designed to obtain complex shape aerodynamic heat-transfer and pressure measurements.

#### b. Reynolds Number Simulation

The capability to simulate the free-stream Reynolds number in hypersonic air, nitrogen, and helium tunnels is shown in figure 3 in terms of free-stream Mach number. The free-stream Reynolds number is based on a one-foot model in air and nitrogen tunnels, and a 0.25 foot model in helium tunnels. The region of free-stream Reynolds numbers associated with reentry is also shown. This region is bounded by values corresponding to trajectories with a wing loading parameter,  $W/SC_L$ , range between 50 and 500. The region of free-stream Reynolds numbers pertaining to sustained hypersonic cruise between altitudes of 100,000 and 300,000 feet at  $M_\infty = 10$  is also shown. The free-stream Reynolds numbers for flight were computed assuming a prototype 30-foot vehicle. Simulation of free-stream Reynolds number and Mach number over these two flight regimes is shown to be quite good.

Simulation of the free-stream Reynolds number and the Mach number in ground facilities does not insure that boundary-layer development over the test model will be similar to boundary-layer development over the prototype vehicle in flight. Boundary-layer development is dependent upon the boundary-layer edge Reynolds number,  $Re_e$ , the edge Mach number,  $M_e$ , and the ratio of the wall temperature to the boundary-layer edge temperature,  $T_w/T_e$ . Large differences between wind-tunnel and flight values for  $Re_e$  and  $M_e$  have been calculated for sharp flat plates. Differences in  $Re_e$  and  $M_e$  are illustrated for two free-stream Mach numbers in figure 4 in terms of angle of attack,  $\alpha$ .

Edge Reynolds number differences depend also somewhat on the geometry as is illustrated by figure 5 for sharp flat plates and sharp cones. In this figure, the Reynolds number ratio of figure 4 has been inverted and presented as a function of  $\alpha$  and the ratio of total enthalpies  $i_{WT}/i_{FLT}$ . The band indicates the

effect of free-stream pressure in the range from  $10^{-1}$  to  $10^{-6}$  atmospheres at  $M_\infty = 10$  and from  $10^{-3}$  to  $10^{-5}$  atmospheres at  $M_\infty = 20$ . For the lowest enthalpy ratio, the differences in  $Re_\theta$  at  $M_\infty = 20$  approach a factor of 10 at high angles of attack for both geometries.

### c. Lewis Number and Knudsen Number Simulation

#### 1) Lewis Number

The dimensionless group  $(\rho c_{p,f} D/k_f)$  is defined as the Lewis number,  $Le$ . It represents the ratio of energy transported by diffusion to that transported by conduction. The subscript  $f$  on the specific heat,  $c_p$ , and thermal conductivity,  $k$ , indicate that these parameters represent a frozen gas composition (i.e., no chemical reactions are taking place). The other two terms in this group are the density,  $\rho$ , and  $D$ , the binary diffusion coefficient between the dissociated and undissociated species. This parameter is generally used as a correction factor that accounts for diffusion effects on convective heat transfer. For instance, in reference 6, it appears in the correlation equation for stagnation-point heating as

$$\frac{\dot{q}}{\dot{q}_{Le=1}} = 1 + (Le^{0.52} - 1) \frac{i_D}{i_o} \quad (1)$$

whereas, in reference 7, stagnation-point heat transfer for Lewis numbers different from unity is represented by the expression

$$\frac{\dot{q}}{\dot{q}_{Le=1}} = 1 + (Le - 1) \left( \frac{i_D - i_{D,w}}{i_o - i_w} \right) \quad (2)$$

In equations (1) and (2),  $i_D$  is the enthalpy absorbed in the process of dissociation,  $i_o$  is the total enthalpy of the undissociated gas, and  $w$  refers to conditions at the wall. It is shown in reference 7 that for a highly cooled wall (i.e.,  $T_w/T_o \ll 0.1$ ), equations (1) and (2) agree to within a few percent.

Lewis number comparisons can be made between flight and ground facilities that use air or other multicomponent gases as a test medium. The range of Lewis numbers that can be obtained in facilities using air as a test medium is presented in Table I. Curves of reference 8 indicate that the Lewis number can range from about 0.6 to 1.5 in flight and will generally be less than unity for that portion of the reentry corridor where heating is most severe.

TABLE I

GROUND FACILITIES	Lewis Number Range
Wind tunnels, shock tunnels, and hotshot tunnels	1.0 - 1.5
Shock tubes	0.6 - 1.5
FLIGHT	0.6 - 1.5

Values in Table I indicate that Lewis number for the entire range of reentry can only be simulated in shock tubes.

Since the Lewis number is only used for small corrections<sup>2</sup> to the heat-transfer calculation, its duplication is not as important as is the duplication of the other parameters already discussed.

## 2) Knudsen Number

The Knudsen number,  $Kn$ , is defined by the dimensionless parameter  $\lambda/l$ , where  $\lambda$  is the mean-free-path of the molecules comprising the free-stream fluid, and  $l$  is a characteristic body length. The Knudsen number is generally used as a criterion to determine if a fluid can be treated as a continuous medium. When  $Kn \ll 1$ , it is assumed that a continuum behavior exists. Free-stream conditions in the three groups of facilities considered in this analysis meet this criterion.

## 2. REAL-GAS EFFECTS IN GROUND-FACILITY NOZZLE FLOW

Real-gas effects on ground-facility nozzle flow-field properties are directly related to chemical changes that result from high stagnation chamber temperatures. For instance, up to temperatures on the order of 1200 °R air can be considered to behave as a perfect gas. At temperatures greater than about 1200 °R, appreciable vibration of the gas molecules begins, but no chemical reactions occur. The region of vibrations extends from about 1200 °R to about 3600 °R. Dissociation of the oxygen contained in air molecules becomes appreciable at about 3600 °R. Dissociation of the nitrogen contained in air is the next major chemical reaction that occurs. At about 10,000 °R, ionization of the atoms becomes significant, and large quantities of positively and negatively charged particles appear in the air. As this temperature is increased, the fluid becomes more and more like a plasma with an electrical conductivity comparable to sea water. Nitrogen and helium react to high temperatures in a similar manner.

Total enthalpy levels in present-day ground facilities are high enough to cause significant real-gas effects on gas properties. Real-gas effects on helium tunnel nozzle flows are generally small due to the low energy state in the stagnation chamber. Air-nitrogen tunnels, on the other hand, operate at stagnation temperatures high enough to cause molecular dissociation in the stagnation chambers. For example, it is shown in reference 9 that for air in chemical equilibrium at a pressure of one atmosphere and a temperature of 5900 °R the oxygen contained in the air is approximately 50% dissociated. As a result of this dissociation, real-gas effects on test-section gas properties of the hypersonic

---

2 The maximum effect of diffusion on heat transfer with  $Le = 1.4$  in an air facility is about 5%. In flight, at velocities in excess of 18,000 fps the effect of  $Le$  is approximately 10% at the stagnation point.

free stream are dependent upon not only enthalpy and entropy, but also upon the time required for atom recombination with respect to the time required for expansion. The degree of dissociation must be nearly zero in the free stream at the test section in order to simulate the free stream that will be encountered at most flight conditions.

Since recombination of a dissociated gas requires a finite amount of time, it is possible that the stream flow may reach the test section partially dissociated. Expanding flows in chemical nonequilibrium are difficult to assess analytically but can be evaluated for the limiting cases of equilibrium and frozen expansions (e. g., references 1, 10, and 11). If the flow is considered frozen as it expands, it is most probable that the flow will tend toward equilibrium again as a result of compression near a test model. This is the inverse of what happens in flight where dissociation, if it occurs, takes place behind the shock wave generated by a hypersonic vehicle or in the boundary-layer near the surface. As a result, stream-flow gas properties typical of flight conditions can only be simulated in air-nitrogen tunnels when the stream is in equilibrium. It is shown in reference 10 that for stagnation-chamber pressures greater than about 35 atmospheres, and total enthalpies less than about 2650 Btu/lbm, the expansion of air in a nozzle is essentially in equilibrium.

Charts are provided in reference 1 for determining real-gas effects in hypersonic nozzle flows in equilibrium air from knowledge of stagnation-chamber conditions. A more detailed study of these effects has been presented in reference 12 with results that allow rapid determination of test-section gas properties.

## SECTION III

### EXTRAPOLATION METHODS

This section describes methods and procedures for extrapolating wind-tunnel heat-transfer data to flight conditions. The term "extrapolation" denotes adjustment of wind-tunnel data to account for lack of complete simulation of flight conditions in the air-nitrogen and helium tunnels discussed in Section II.

A series of charts is presented that can be used in the development of extrapolation factors for the following geometric elements; (1) sharp delta wings, (2) deflected control surfaces, (3) interference geometries typified by yawed cylinders attached to a sharp flat plate, (4) shallow convex surface waves and rectangular grooves. These charts are evaluated at conditions representative of both the flight environment defined by the reentry corridor illustrated in figure 6 and the environment in air-nitrogen and helium tunnels. (Some operational air-nitrogen tunnels can simulate the environment of sustained hypersonic cruise. As a result, extrapolation factors are not generally required for heat-transfer and pressure measurements made in this flight regime and have not been specifically treated in this report.)

Within the reentry corridor shown in figure 6, dependence of extrapolation factors on pressure is on the order of 3%; hence, average pressures are used to represent the flight regime. Changes in the extrapolation factors that are due to variations in total enthalpy at the same Mach number in flight are on the same order and have been neglected in this report. All charts representing flight conditions are calculated for a free-stream temperature equal to 400 °R, and a wall temperature,  $T_w$ , equal to 2000 °R. Wind-tunnel charts are calculated for  $T_w = 540$  °R. All calculations are made for flows in chemical equilibrium. Nonequilibrium effects on the extrapolation factors are discussed in Section III-6. All calculations are made using the thermodynamic gas properties of reference 13.

The basic approach of the present analysis in extrapolation factor development is to use analytic methods. In this manner, those parameters influencing the extrapolation factors can be evaluated systematically.

#### 1. BASIC EXTRAPOLATION PROCEDURE

Application of ground-test data to flight conditions is accomplished in four parts. First, the data are extrapolated from wind-tunnel to flight enthalpy conditions at constant Mach number. The differences between these two conditions are expressed by a factor  $F_i$ , the subscript  $i$  denoting the fact that enthalpy is the varying quantity. In functional form,  $F_i$  appears as:

$$F_i = (\bar{h}_{FLT} / \bar{h}_{WT})_{M_\infty, WT} \quad (3)$$

where  $\bar{h}$  is a normalized laminar heat-transfer coefficient and the subscripts WT and FLT denote wind-tunnel and flight conditions at the wind tunnel Mach number,  $M_\infty, WT$ . Values for  $F_i$  are shown in charts for each of the elements.

The second part of the extrapolation procedure consists of "adjusting" the partially extrapolated data to account for differences between the wind-tunnel free-stream Mach number and the flight value. These differences are expressed in terms of the factor  $F_M$ , where the subscript M denotes that the Mach number is the varying quantity. The factor  $F_M$  is computed by forming a ratio of the normalized heat-transfer coefficients at the flight Mach number to that corresponding to the wind-tunnel Mach number as follows:

$$F_M = (\bar{h}_{M_\infty, FLT} / \bar{h}_{M_\infty, WT}) \quad (4)$$

A third extrapolation factor  $F_x$  is required to account for length differences on the sharp delta wing. For laminar flow  $F_x$  is defined as

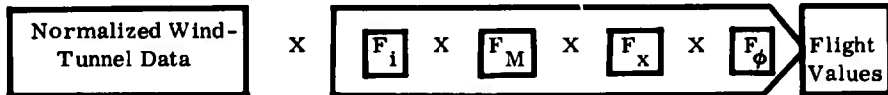
$$F_x = (x_{WT} / x_{FLT})^{1/2} \quad (5)$$

where  $x$  is the distance measured from the apex or leading edge of the wing.

A fourth extrapolation factor which only appears in the sharp delta-wing extrapolation procedure accounts for cross-flow pressure gradients and is defined as

$$F_\phi = \frac{(h_\phi / h_{\phi=0})_{FLT}}{(h_\phi / h_{\phi=0})_{WT}} \quad (6a)$$

This procedure is illustrated in the following sketch for laminar boundary-layer flow



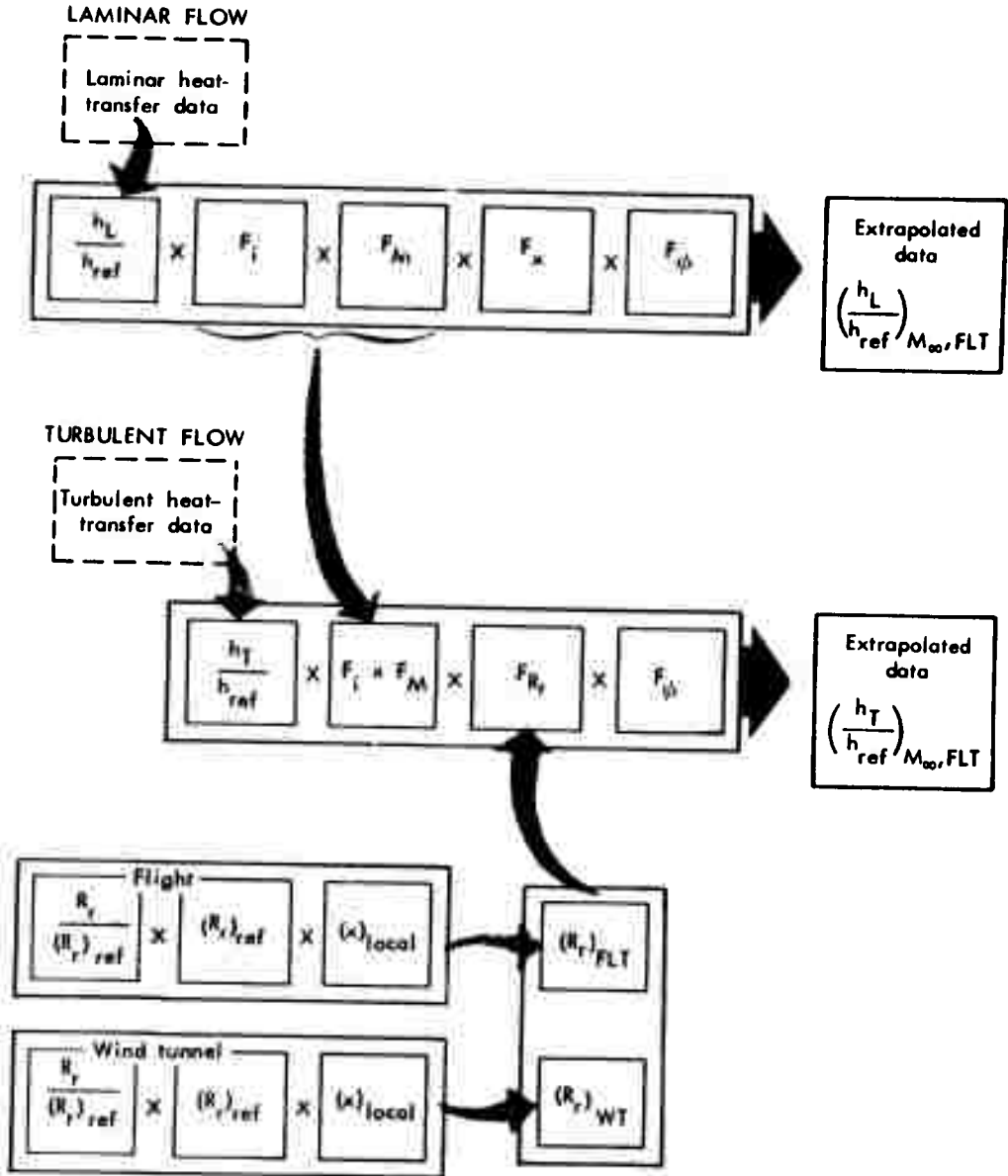
For the sharp delta wing in turbulent flow, a fifth extrapolation factor  $F_{R_r}$  is required. It is based on differences in the local Reynolds number and is defined as

$$F_{R_r} = \frac{(h_T / h_L)_{FLT}}{(h_T / h_L)_{WT}} \quad (6b)$$

where  $h_T / h_L$  is defined by equation (A19) in Appendix A.

## 2. SHARP DELTA WINGS

The complete extrapolation procedure in both laminar and turbulent flow for a sharp delta wing is shown in the following sketch.



a. Laminar Flow

To use the procedure illustrated on the previous page, it is necessary to normalize wind-tunnel heat-transfer data measured locally by a laminar reference heat-transfer coefficient,  $h_{ref}$ , defined as the stagnation-point heat-transfer coefficient for a hemisphere with a one-foot radius. Wind-tunnel stagnation-point heat-transfer data can be transformed to  $h_{ref}$  by the expression

$$(h_{ref})_{WT} = (h_o)_{WT} (r)^{1/2} \quad (7)$$

where  $r$  is the radius of the test model in feet. Local heating-rate data is normalized by  $h_{ref}$  for the free-stream Mach number at which the data were measured to form the ratio  $(h_L/h_{ref})_{M_\infty, WT}$ .

The extrapolation factors at the centerline of the delta wing are defined by the following expressions

$$F_i = \left[ \frac{(h/h_{ref})_{FLT}}{(h/h_{ref})_{WT}} \right]_{(M_\infty, x) WT} \quad (8)$$

$$F_M = \left[ \frac{(h/h_{ref})_{M_\infty, FLT}}{(h/h_{ref})_{M_\infty, WT}} \right]_{(i, x) FLT} \quad (9)$$

$$F_x = \left( \frac{x_{WT}}{x_{FLT}} \right)^{1/2} \quad (10)$$

where the subscript  $(M_\infty, x)WT$  denotes evaluation at the Mach number and distance in the wind tunnel and the subscript  $(i, x)FLT$  denotes evaluation at the enthalpy and distance in flight.

In equations (8) and (9) the ratio  $(h/h_{ref})$  is determined at the centerline using the heat-transfer method presented in Appendix A. Flow-field gas properties required to compute the heating rates in proximity to the centerline are computed using the method described in Appendix B.

For the delta wing, the extrapolation factor  $F_i$  in air-nitrogen wind tunnels has been evaluated in terms of the enthalpy ratio  $(i_o)_{WT}/(i_o)_{FLT}$  and free-stream Mach number,  $M_\infty$ . It is presented in figure 7 for delta wings with leading-edge sweep angles between 70 and 80-degrees in the angle-of-attack range between 10

and 60-degrees. This factor for helium tunnels is presented in figure 8 in terms of the free-stream Mach number and angle of attack.

Solutions for the heat-transfer ratios required to form the extrapolation factor  $F_M$  are presented in figure 9. The ratio  $(h/h_{ref})$  for flight is obtained at flight Mach numbers. Figure 9 is presented for delta wings having leading-edge sweep angles of 70, 75, and 80-degrees.

The extrapolation factor  $F_x$  is obtained using equation (10).

b. Turbulent Flow

Extrapolation of turbulent heat-transfer data to flight conditions is accomplished using an extension of the laminar method described above. This procedure is diagrammed in the lower portion of the preceding sketch. To begin the extrapolation procedure, the wind-tunnel turbulent heat transfer data,  $h_T$ , is also normalized by  $h_{ref}$ , the laminar reference heat-transfer coefficient discussed in the preceding text. In addition to the factors  $F_l$  and  $F_M$ , an extrapolation factor that incorporates differences in the local Reynolds number is required. This factor,  $F_{R_r}$ , is a ratio of turbulent to laminar heat-transfer coefficient ratios at flight and wind-tunnel conditions and is defined as

$$F_{R_r} = \frac{(h_T/h_L)_{FLT}}{(h_T/h_L)_{WT}} \quad (11)$$

The ratio  $h_T/h_L$  is evaluated in terms of the local Reynolds number by the expression

$$\frac{h_T}{h_L} = \left\{ \frac{0.185 \sqrt{R_r}}{0.332 [\log_{10} (R_r + 3000)]^{2.584}} \right\} \quad (12)$$

where  $R_r$  is the local reference Reynolds number defined as

$$R_r = \frac{\rho_r \mu_r u_{eq,L}^x}{\mu_o^2 F_x^2} \quad (13)$$

These expressions are unique to the " $\rho_r \mu_r$ " heat-transfer method described in Appendix A.

In order to evaluate  $F_{R_r}$ , the local reference Reynolds numbers in flight and in the wind tunnel must first be known. Values for  $R_r$  at the centerline of the delta-wing are presented for wind tunnel and flight conditions in figure 10. In this figure,  $R_r$  is presented for  $x = 1$  foot and has been normalized by  $(R_r)_{ref}$ , the Reynolds number for a sharp flat plate at  $\alpha = 20^\circ$  and  $x = 1$  foot. Wind-tunnel values for  $(R_r)_{ref}$  are presented as a function of free-stream Mach number and temperature in figure 11 and are normalized by the free-stream pressure. Flight values are presented in terms of altitude and free-stream velocity in figure 12. Local values for  $R_r$  are determined using the expressions

$$(R_r)_{FLT} = \left[ \frac{R_r}{(R_r)_{ref}} \right]_{FLT, x = 1 \text{ ft}} \cdot (R_r)_{ref, FLT} \cdot x_{FLT} \quad (14)$$

$$(R_r)_{WT} = \left[ \frac{R_r}{(R_r)_{ref}} \right]_{WT, x = 1 \text{ ft}} \cdot (R_r)_{ref, WT} \cdot x_{WT} \quad (15)$$

The extrapolation factor  $F_{R_r}$  is shown in figure 13 as a function of a ratio of the local reference Reynolds number at flight conditions to that at wind-tunnel conditions.

The complete extrapolation procedure that is used to extrapolate sharp delta-wing centerline heat-transfer data in turbulent flow is illustrated below:



c. Off-Centerline

The extrapolation procedure for laminar and turbulent heat-transfer data measured at off-centerline (spanwise) locations on a delta wing consists of multiplying the extrapolated centerline data by an additional factor,  $F_\phi$ , defined as,

$$F_\phi = \frac{(h_\phi/h_{\phi=0})_{FLT}}{(h_\phi/h_{\phi=0})_{WT}} \quad (16)$$

where  $h_\phi$  is the local spanwise heat-transfer coefficient and  $h_{\phi=0}$  is the centerline heat-transfer coefficient measured at a location as illustrated in the following sketch:



Spanwise heat-transfer coefficients are calculated for both wind-tunnel and flight conditions by the methods described in Appendix A. Flow-field gas properties are determined using reference 13 and the flow-field method described in Appendix C.

Equation (16) has been evaluated at a free-stream Mach number of 20 in laminar flow for sharp delta wings with leading-edge sweep angles of 70 and 80-degrees. Curves are presented in figure 14 for a total enthalpy ratio,  $(i_0)_{WT} / (i_0)_{FLT}$ , equal to 0.25.

#### d. Dissimilar Flow-Field Effects

Extrapolation of sharp delta-wing wind-tunnel data to flight conditions with the charts discussed in this section can only be made when the flow fields surrounding the delta wing are similar in both wind tunnel and flight. An example of dissimilar flow fields on sharp delta wing surfaces is illustrated as follows.

The flow on the windward surface of sharp delta wings is supersonic for a wide range of angles of attack. However, at very high angles of attack the flow field is subsonic. In a subsonic region, a downstream disturbance in the flow field can be transmitted upstream, and in this way alter the entire lower surface flow field. Such a disturbance may be caused by deflected control surfaces, vertical fins, etc. In such a situation, differences in heat transfer occur primarily due to a lack of local flow-field simulation rather than enthalpy simulation. Of course, the flow field differences have been induced by differences in total enthalpy, but the resultant effects on heat transfer due to dissimilar flow fields cannot be determined until a method has been developed for calculating the inviscid subsonic flow field. This calculation is approximately equivalent to that of calculating the flow over a triangular blunt body at angle of attack, and so is considerably more complex than any that has yet been accomplished. The angle of attack at which the flow field becomes subsonic is sensitive to real-gas effects. This effect is illustrated in figure 15. Using this figure, it is seen that the lower surface flow field on a 70-degree swept sharp delta wing is subsonic in a Mach 20 wind tunnel at a 60° angle of attack but supersonic for a flight case at the same angle of attack.

### 3. DEFLECTED CONTROL SURFACES

One possible way to control maneuverable reentry vehicles is through management of aerodynamic forces. A logical way to accomplish this control is to add flaps. However, when flaps are deflected the flow field in proximity to the flap is disturbed. Analytic methods that adequately describe this flow field are non-existent. As a result, aerodynamic pressure and heat-transfer distributions on deflected flaps, in the presence of upstream disturbances, will largely come from wind-tunnel tests.

A first-order approximation for extrapolating wind-tunnel data to flight conditions can be obtained analytically for simple two-dimensional control surfaces preceded by uniform two-dimensional flow. The stream-flow gas properties on these control surfaces are dependent upon the transport properties and thermodynamic gas properties upstream of the deflected surface. For compression surfaces, the dynamic pressure and local pressure at the hinge line exert the

greatest influence on the extrapolation factors presented in this report. On expansion surfaces, extrapolation methods developed here are dependent upon the boundary-layer displacement-thickness, pressure, and heat-transfer coefficient at the hinge line. These extrapolation methods are described below.

a. Compression Surfaces

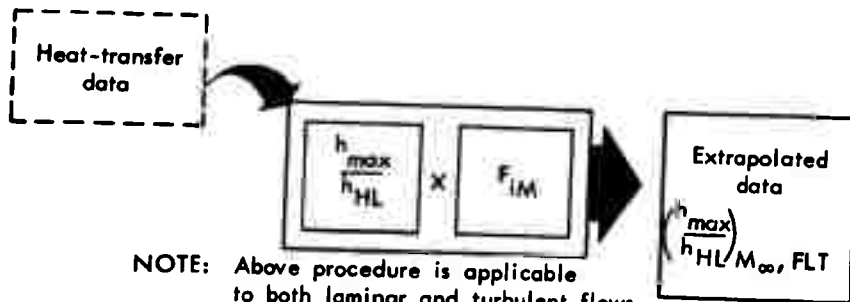
Control surfaces deflected into the stream will compress the oncoming flow. It is possible that the boundary layer of this stream will separate from the surface ahead of the hinge line. An example of this phenomenon is shown by the data of reference 14. When separation occurs, the pressure and aerodynamic heating distributions are altered significantly.

An analysis of aerodynamic heat transfer through a laminar separated region using an extension of boundary-layer theory is presented in reference 15. That analysis indicates that average aerodynamic heat transfer is reduced 50% as compared to an attached flow for the same local flow properties at the boundary-layer outer edge. These results have been verified by tests (see references 16 and 17). Yet, predicting regions of flow separation, their location of re-attachment, and the accompanying heating distributions analytically has not yet been possible.

Another approach, the one used in the present analysis, is to predict the more severe situation — one resulting in maximum heating rates. An approximate method for predicting an upper limit on the local heat transfer to flaps deflected into laminar or turbulent streams is presented in reference 14. It is based on the expression

$$\frac{h_{\max}}{h_{HL}} = \frac{P_{\max}}{P_{HL}} \tag{16a}$$

where  $h_{\max}$  is the maximum heat-transfer coefficient expected on the control surface,  $h_{HL}$  is the heat-transfer coefficient at the hinge line,  $P_{\max}$  is the pressure predicted using the oblique-shock method, and  $P_{HL}$  is the pressure at the hinge line. This method, which is verified by data contained in that report and in references 18 and 19, forms the basis for the extrapolation procedure illustrated in the following sketch:



NOTE: Above procedure is applicable to both laminar and turbulent flows

To extrapolate the maximum heating rate measured on a compression surface, the deflected flap heat-transfer data must first be normalized using heating rates measured just upstream of the hinge line. (It is important to note that the measured heat-transfer data at the hinge line and on the control surface must be either laminar or turbulent, not transitional.) The wind-tunnel data are then extrapolated to flight conditions using the extrapolation factor  $F_{iM}$ , which is defined as follows:

$$F_{iM} = \frac{(h_{\max}/h_{HL})_{M,FLT}}{(h_{\max}/h_{HL})_{M,WT}} \quad (17)$$

where the subscripts M,FLT and M,WT denote the flight Mach number and the wind-tunnel Mach number, respectively.

In equation (17), the factor  $(h_{\max}/h_{HL})$  is determined by equating it to a pressure ratio determined using the oblique-shock method, and assuming the flow field upstream of the hinge line is unseparated. The pressure ratio has been correlated for both wind-tunnel and flight conditions in terms of the parameter  $(2\hat{q}/P)_{HL}$ , where  $\hat{q}$  is the dynamic pressure and  $P$  is the pressure, both evaluated at the hinge line. This correlation is presented in figure 16 for air-nitrogen wind-tunnels, where the ratio  $P/P_{HL}$  has been replaced by the ratio  $h_{\max}/h_{HL}$ . The lines labeled  $\gamma = 1.4$  in figure 16 represent ideal-gas solutions in air. For a constant flap-deflection angle  $\delta$ , all of the solutions are confined to a narrow region which varies with  $(2\hat{q}/P)_{HL}$ , and which widens with increasing flap-deflection angles. At fixed values of  $\delta$  and  $(2\hat{q}/P)_{HL}$ , the upper bound on  $h_{\max}/h_{HL}$  is represented by the ideal-gas solution. With increasing departure from ideal-gas conditions, solutions shift toward the lower bound of the region. The lower bound in figure 16, labeled  $\gamma_{\text{eff}} = 1.1$ , represents flight-case solutions at a free-stream Mach number of 20 and a pressure of  $10^{-3}$  atmospheres. Real-gas effects in the flow field fostered by the flap are negligible in helium and figure 17 presents heating rate ratios applicable to all helium tunnels operating at stagnation temperatures equal to the ambient temperature.

Values of the parameter  $(2\hat{q}/P)_{HL}$  are dependent upon the geometry upstream of the hinge line and must be evaluated independently. In the correlations shown in figures 16 and 17, the only restriction placed on the flow field upstream of the hinge line is that it be two-dimensional and uniform.

#### b. Expansion Surfaces

Analytic methods for obtaining viscosity-induced pressure and heat transfer to a surface downstream of a fully developed boundary layer in an expanding hypersonic inviscid flow field are not well developed. This problem is characterized in references 2 and 14 by the expansion of a non-rotational hypersonic flow field about a sharp corner. In these two references, it was assumed that, (1) Prandtl's boundary-layer concept was valid such that the viscous and inviscid flow regions could be separated, and (2) the effective turning angle of the inviscid flow field was

reduced by the growth of the viscous boundary layer. Both of these references indicate that a complete calculation of this flow field requires simultaneous solution of the boundary-layer equations and the equation for a Prandtl-Meyer expansion. In reference 2, an iterative process based upon results from a nonsimilar boundary-layer program (reference 19) and the Prandtl-Meyer equation was used. In contrast, an expression for the effective turning angle in a two-dimensional flow field was derived in reference 14, using physical reasoning in conjunction with an assumed similarity for the boundary-layer profiles. The effective turning angle  $\Delta\nu$ , as defined in that document, is

$$\Delta\nu = \Delta F + \frac{n}{\bar{p}^{n+1}} \frac{d\bar{p}}{dx} \quad (18)$$

in which

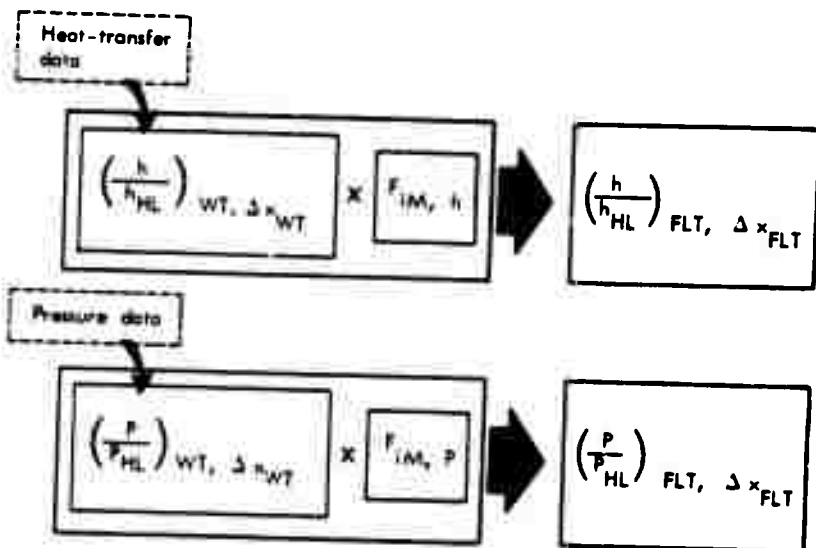
$$\bar{p} = \frac{P}{P_{HL}} \quad (19a)$$

and

$$x = \frac{x - x_{HL}}{\delta_{HL}^*} = \frac{\Delta x}{\delta_{HL}^*} \quad (19b)$$

In equations (18) and (19)  $P$  is the local pressure,  $P_{HL}$  is the hinge line pressure,  $\Delta F$  is the flap turning angle,  $x$  is the distance from the leading edge to the location of interest,  $x_{HL}$  is the distance from the leading edge to the hinge line,  $\delta_{HL}^*$  is the displacement thickness at the hinge line, and  $n$  is equal to unity.

Solution of equation (18) results in values for the pressure ratio  $P/P_{HL}$  that are dependent only upon  $\Delta x/\delta_{HL}^*$ . This suggests that extrapolation factors can be formed that allow extrapolation of both pressure and heat transfer data for expansion surfaces to flight conditions. The procedure suggested is illustrated below.

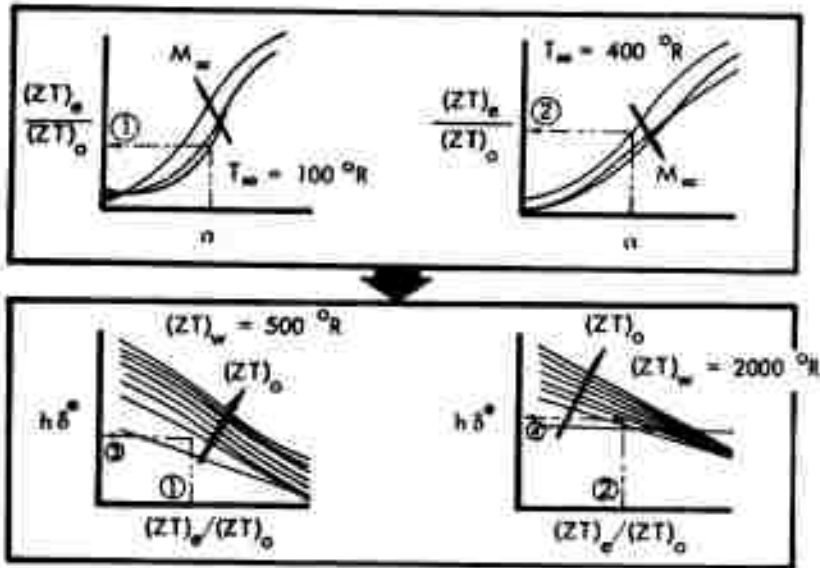


In this extrapolation procedure,  $(h/h_{HL})_{WT}$  and  $(P/P_{HL})_{WT}$  are the normalized wind-tunnel data. The extrapolation factor  $F_{IM, P}$  is defined as

$$F_{IM, P} = \frac{(P/P_{HL})_{FLT}, (\Delta x/\delta^*)_{FLT}}{(P/P_{HL})_{WT}, (\Delta x/\delta^*)_{WT}} \quad (20)$$

In the present analysis, the pressure ratio  $(P/P_{HL})$  is determined for attached flow on the flap using equation (18). Charts showing this pressure ratio are presented in figure 18, in terms of  $\Delta x/\delta^*_{HL}$ , and the flap expansion angle. The extrapolation factor  $F_{IM, P}$  is formed for any location on the flap by determining the pressure ratio corresponding to  $\Delta x/\delta^*_{HL}$ , evaluated at wind-tunnel or flight conditions.

Boundary-layer displacement thicknesses at the hinge line may be evaluated using the parameter  $h\delta^*$  for a sharp flat plate at angle of attack. In this parameter,  $h$  is the heat-transfer coefficient at the hinge line and must be known a priori. In the present analysis, it was found that  $h\delta^*$ , as developed in reference 2 for air, could be very nearly approximated in terms of compressibility factor-temperature products,  $ZT$ , evaluated at three different shock-layer locations. These locations are at the wall, at the boundary-layer edge of the flat plate, and at the stagnation point of a body immersed in the same free-stream flow. The compressibility factor-temperature product at the boundary layer edge,  $(ZT)_e$ , of a sharp flat plate at angle of attack is shown in figure 19 in terms of the stagnation-point product  $(ZT)_o$ . Figure 19 corresponds to free-stream flow temperatures of 100 and 400°R. The parameter  $h\delta^*$  is shown in figure 20 in terms of the three compressibility factor-temperature products,  $(ZT)_e$ ,  $(ZT)_w$ , and  $(ZT)_o$ . The subscript  $w$  denotes evaluation at the wall. The procedure for evaluating the parameter  $h\delta^*$  is shown in the sketches below.



The extrapolation factor  $F_{iM,h}$  for heat transfer is defined as

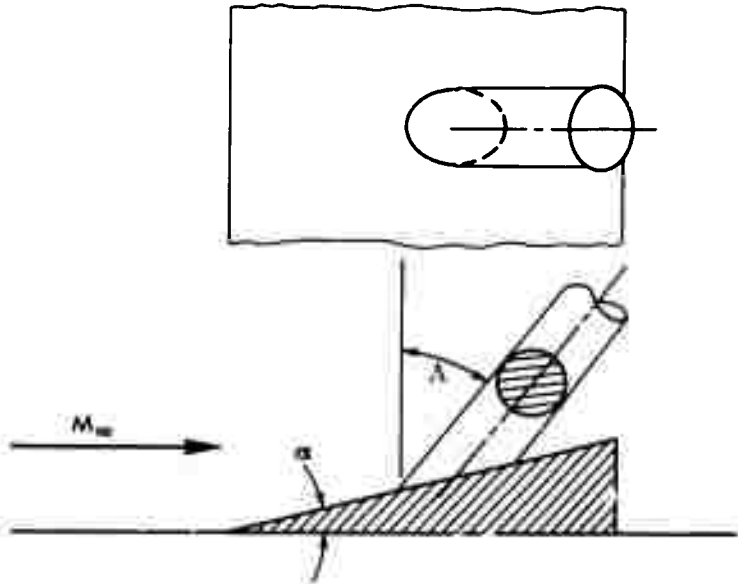
$$F_{iM,h} = \frac{(h/h_{HL})_{FLT}, (\Delta x/\delta^*)_{FLT}}{(h/h_{HL})_{WT}, (\Delta x/\delta^*)_{WT}} \quad (21)$$

The ratio  $(h/h_{HL})$  in equation (21) is evaluated using curves presented in this report in exactly the same way as the pressure ratio of equation (20). Charts showing the heat transfer coefficient ratio,  $h/h_{HL}$ , are shown in figure 21. In this figure,  $h/h_{HL}$  is presented in terms of the flap expansion angle, at  $\alpha = 10$  and  $40$  degrees and  $M_\infty = 10$  and  $20$ .

#### 4. INTERFERENCE GEOMETRIES

Maneuverable reentry vehicles and hypersonic cruise vehicles, which of necessity are designed with protruding stabilizers and control surfaces, will foster mutually interfering flow fields. As a result, some portion of either type of vehicle may experience shock-wave impingement, or separating and reattaching flows. The increased pressure associated with interfering flow fields has the tendency to reduce the boundary-layer thickness in the region of interference and, consequently, increase the local convective heat-transfer rate. Data reported in references 20 through 28 indicate that local heating rates can be larger by an order of magnitude or more compared to those without interference. In general, the size of interference regions, as indicated by the data, is small; hence, the total heat load is not substantially increased.

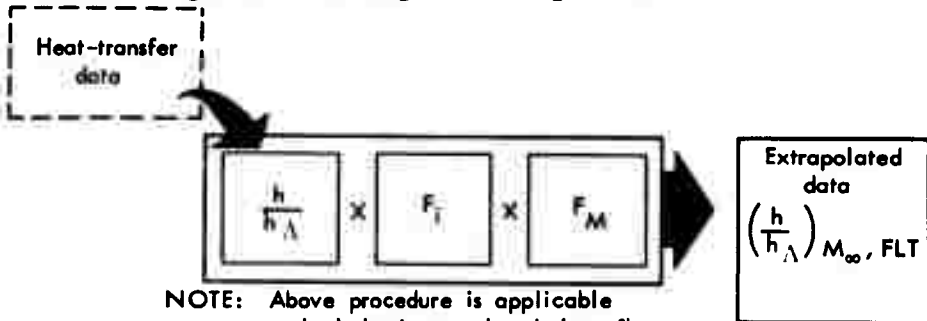
An interference geometry is defined as a body which generates a secondary shock system that interacts with the basic shock system. For example, a swept cylinder-flat plate combination, as illustrated below:



The flat plate deflected at a slight angle generates a secondary shock wave which interacts with the basic shock wave generated by the swept cylinder. The flat plate represents the slender body of a vehicle. The cylinder represents the leading edge of a wing, a stabilizer, or an inlet, and is mounted to the flat plate at a sweep angle  $\Lambda$ . The cylinder sweep angle is always measured with respect to an axis perpendicular to the free-stream flow direction.

a. Swept-Cylinder Stagnation-Line Interference Heating

The data extrapolation method developed for the interference geometry is applicable at the stagnation line of the swept cylinder. Stagnation-line heat-transfer data that has been measured on a cylinder in a disturbed flow field, and normalized using swept-infinite-cylinder theory, is extrapolated from wind-tunnel conditions to flight conditions using the following format:

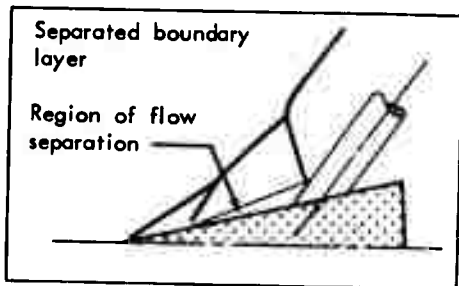
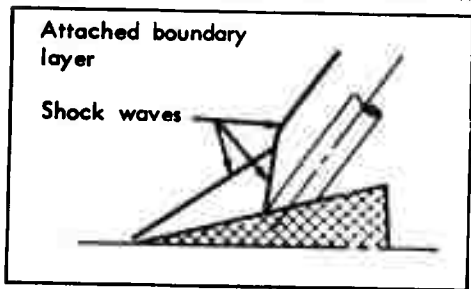


NOTE: Above procedure is applicable to both laminar and turbulent flows

The wind-tunnel data is expressed in the form  $(h/h_{\Lambda})$ , where  $h$  is heat-transfer coefficient data on the leading edge in the interference region, and  $h_{\Lambda}$  is the stagnation-line heat-transfer coefficient for an infinite cylinder of the same sweep angle and radius. The factor  $F_i$  is used to extrapolate the data from wind-tunnel to flight enthalpy conditions at the wind-tunnel Mach number. The factor  $F_M$  is used to extrapolate flight values from the wind-tunnel Mach number to the desired flight Mach number. The procedure is identical for laminar and turbulent flows. The extrapolation factor  $F_i$  is defined as:

$$F_i = \left[ \frac{(h_{\max}/h_{\Lambda})_{FLT}}{(h_{\max}/h_{\Lambda})_{WT}} \right]_{M_{\infty}, WT} \quad (22)$$

In equation (22), the maximum heat-transfer coefficient in the vicinity of shock-wave impingement,  $h_{\max}$ , is normalized using the undisturbed stagnation-line heat-transfer coefficient for an infinite cylinder,  $h_{\Lambda}$ . The evaluation procedure used for this ratio is dependent upon the flow-field geometry. The first method used corresponds to a flow field where the secondary shock wave fostered by the cylinder is attached at the intersection of the cylinder and the boundary-layer re-attachment location. The second method corresponds to a flow field where this secondary shock wave is detached. The flow model illustrated in the following sketch for an attached shock wave was first postulated in reference 21.



For this flow field, the ratio  $(h_{\max}/h_{\Lambda})$  is defined by the relationship

$$\left( \frac{h_{\max}}{h_{\Lambda}} \right)_L = \left( \frac{P_{\max}}{P_{\Lambda}} \right)^{0.5} \left[ \frac{T_{SL, (\Lambda + \alpha)}}{T_{SL, \Lambda}} \right]^{0.25} \left( \sqrt{2} \frac{g'_{w, SP}}{g'_{w, SL}} \right) \quad (23a)$$

where  $h_{\max}$  is the maximum heat-transfer coefficient in the vicinity of shock wave impingement,  $h_{\Lambda}$  is the undisturbed stagnation-line heat-transfer coefficient for an infinite cylinder,  $P_{\max}$  is the stagnation-line pressure determined by the interference method,  $P_{\Lambda}$  is the stagnation-line pressure on a yawed infinite cylinder, and the subscript L denotes laminar boundary-layer flow. The subscript  $M_{\infty}, WT$  in equation (22) denotes that the ratios  $(h_{\max}/h_{\Lambda})$  for both flight and wind tunnel, are evaluated for a free-stream Mach number equal to that in the wind tunnel. Cylinder stagnation-line pressures for flow with interference are

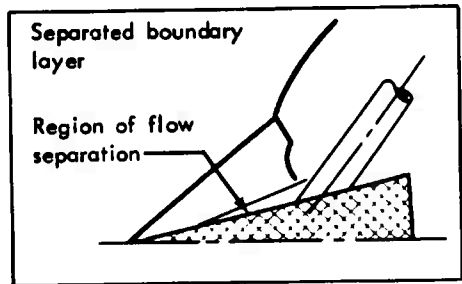
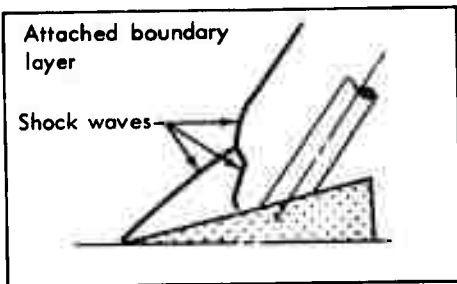
calculated using oblique and normal shock methods as required for the flow field illustrated. The term  $[T_{SL, (\Lambda + \alpha)}/T_{SL, \Lambda}]^{0.25}$  essentially corrects for increases in the effective sweep of the cylinder. The last term is a pressure gradient term tabulated in reference 29 in terms of the velocity gradient parameter,  $\beta$ . In this analysis,  $\beta$  is equal to 1.0 and 0.5 for stagnation-line and stagnation-point flows, respectively. Equation (23a) is developed in reference 21.

Turbulent heat-transfer coefficient ratios for cylinder-plate combinations with attached shock waves are determined using the relationship

$$\left(\frac{h_{\max}}{h_{\Lambda}}\right)_T = \left(\frac{P_{\max}}{P_{\Lambda}}\right)^{0.8} \left[\frac{\sin(\Lambda + \alpha)}{\sin \Lambda}\right]^{0.6} \quad (23b)$$

where the term  $[\sin(\Lambda + \alpha)/\sin \Lambda]^{0.6}$  corrects for the velocity component normal to the cylinder, and the subscript T denotes turbulent boundary-layer flow. Equation (23b) is presented in reference 21 and is a modification of the relationship presented in reference 30. An axial pressure-gradient term which appears to the one-fifth power in the latter analysis has been neglected.

For those flow conditions where the cylinder shock wave detaches at the root of the cylinder, the flow-field is illustrated by the following sketch:



For this situation, the laminar and turbulent heat-transfer coefficient ratios are defined by the following expressions:

$$\left(\frac{h_{\max}}{h_{\Lambda}}\right)_L = \frac{\Delta_2}{\Delta_1} \frac{1}{(\cos^2 \Lambda)} \left(\sqrt{2} \frac{g'_{w, SP}}{g'_{w, SL}}\right) \quad (24a)$$

$$\left(\frac{h_{\max}}{h_{\Lambda}}\right)_T = \frac{\Delta_2}{\Delta_1} \frac{1}{(\cos^2 \Lambda)} \quad (24b)$$

where  $\Delta_1$  represents the shock wave standoff distance for a cylinder in an interfering flow field, and  $\Delta_2$  is the standoff distance for a yawed infinite cylinder. This parameter is calculated as suggested in reference 21 using the relationship

$$\Delta = \frac{f(K_{SL}) (r)}{1 - f(K_{SL})} \quad (25a)$$

where

$$K_{SL} = \rho_\infty / \rho_{SL} \quad (25b)$$

$$f(K_{SL}) = \frac{K_{SL}}{1 - K_{SL}} \ln \left\{ g(K_{SL}) + \left[ g^2(K_{SL}) + 1 \right]^{1/2} \right\} \quad (25c)$$

and

$$g(K_{SL}) = \frac{1 - K_{SL}}{\left[ K_{SL} (2 - K_{SL}) \right]^{1/2}} \quad (25d)$$

In this equation,  $\rho_\infty$  is the free-stream density in front of the shock system generated by the wedge and the cylinder.  $\rho_{SL}$  is the shock-layer density along the cylinder stagnation line, and  $r$  is the cylinder radius. For this flow model, cylinder sweep angles are generally small, and the impinging flow nearly stagnates at the cylinder surface. As a result, the stagnation-line temperature ratio can be expressed in terms of a velocity ratio, which ultimately reduces to the sweep angle function  $\cos^2 \Lambda$  for hypersonic free-stream flow. Axial pressure-gradient effects are determined in the same manner as previously described for an interference geometry fostering an attached shock wave.

The factor  $F_i$  for laminar flow is shown in figure 22 for air-nitrogen tunnels and in figure 23 for helium tunnels as a function of Mach number for three different flat plate angles of attack. The factor  $F_i$  for turbulent flow in air-nitrogen tunnels is shown in figure 24. The dashed and solid lines represent flows with detached and attached shock waves at both wind-tunnel and flight conditions, respectively. Curves are not shown for configurations which have detached shock waves in wind tunnels and attached shock waves in flight. This situation is discussed in the following subsection. The curves in figures 22, 23, and 24 correspond to a total enthalpy ratio  $\bar{i} = 0.25$ , where

$$\bar{i} = \frac{i_{o, WT}}{i_{o, FLT}} \quad (26)$$

For wind tunnels with a different total enthalpy ratio, a linear interpolation of the factor  $F_i$  is suggested between the value shown for  $F_i$  in the chart at  $\bar{i} = 0.25$ , and  $F_i = 1.0$  at  $\bar{i} = 1.0$ . (For example, if the factor  $F_i$  has a value 1.3 at  $\bar{i} = 0.25$ , then, by the above procedure, it has the value 1.2 at  $\bar{i} = 0.50$ , 1.1 at  $\bar{i} = 0.75$ , and 1.0 at  $\bar{i} = 1.0$ .)

The extrapolation factor  $F_M$  is defined as

$$F_M = \frac{(h_{\max}/h_\Lambda)_{M, \text{FLT}}}{(h_{\max}/h_\Lambda)_{M, \text{WT}}} \quad (27)$$

where the ratios  $(h_{\max}/h_\Lambda)$  are obtained from figures 25 and 26. The subscripts M, FLT and M, WT indicate that the heat transfer ratios are evaluated at the flight and the wind-tunnel Mach numbers, respectively.

To determine absolute heating rates in flight, the swept-infinite-cylinder heat-transfer coefficients must be obtained from a separate source. Calculations for swept-infinite cylinders in laminar and turbulent flows are presented in reference 2.

#### b. Dissimilar Flow Fields

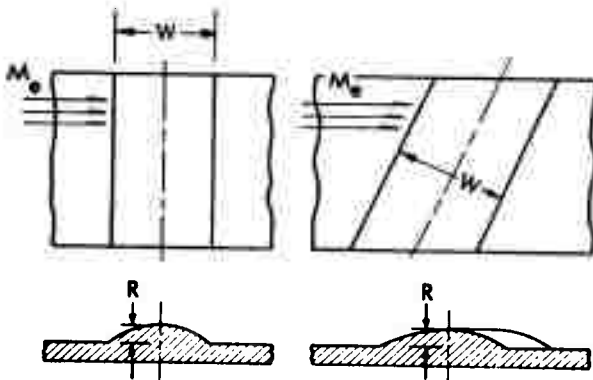
When the shock wave fostered by the cylinder detaches from the root of the cylinder, the interference flow field undergoes a change. Because the theories for predicting maximum heat transfer behind attached and detached shock waves do not converge upon each other at shock-wave detachment, a discontinuity occurs. Shock-wave detachment at the cylinder is dependent upon the cylinder sweep angle, the flat-plate angle of attack, the surface Mach number, and the total enthalpy. Dependence of shock-wave detachment upon total enthalpy fosters a situation which may occur during ground tests when the wind-tunnel total enthalpy is significantly less than that for flight conditions.

In real-gas flows, greater density changes can occur across the shock wave, hence shock-wave detachment may be delayed until much higher angles of attack are reached. When the cylinder sweep angle is small enough to make shock-wave detachment possible, detachment may occur in wind tunnels but not in flight. Figure 27 shows loci of points which represent the approximate boundaries between regions where this situation may occur for flat-plate angles of attack between 10 and 30 degrees. The dashed and solid lines indicate wind-tunnel and flight conditions, respectively. Wind tunnels represented by this chart are assumed to be capable of reaching approximately one-fourth the total enthalpy of flight at the same Mach number. To illustrate the use of this chart, consider a wind tunnel at Mach 15. If the plate (shock generator) is at a 10-degree angle of attack, the dividing point between attached shock waves and detached shock waves in the wind-tunnel is at a cylinder sweep angle of approximately 31 degrees. For sweep angles greater than 31 degrees the shock wave is attached, and at sweep angles less than 31 degrees the shock wave is detached. In flight at Mach 15, the dividing point between attached and detached shock waves occurs at a sweep angle equal to approximately 21 degrees. These results indicate that the flow fields in flight and wind-tunnel are dissimilar between sweep angles of 21 and 31 degrees. For sweep angles less than 21 degrees and greater than 31 degrees, the flow fields are similar in both wind-tunnel and flight environments.

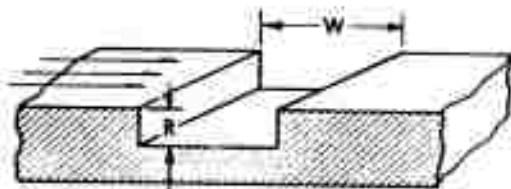
It should be noted that the boundary for the geometry in helium ground facilities at  $\alpha = 30^\circ$  lies between the boundaries at  $\alpha = 10^\circ$  and  $20^\circ$ . This occurs with changing  $\alpha$  due to the combined effect of changes in the cylinder deflection angle ( $90^\circ - \Lambda - \alpha$ ) and the flat-plate surface Mach number,  $M_s$ .

## 5. ROUGHNESS ELEMENTS

It is improbable that the surface of a reentry vehicle, or hypersonic cruise vehicle, will have the ideally smooth surfaces typical of wind-tunnel test models. Manufacturing tolerances, load deformation, and thermal expansion requirements will cause flow-field disturbances. Extrapolation methods have been developed for two types of surface roughness elements, (1) shallow convex waves, and (2) butt joints having a rectangular cavity below the contour line at the joint. These elements are illustrated by the sketch below:

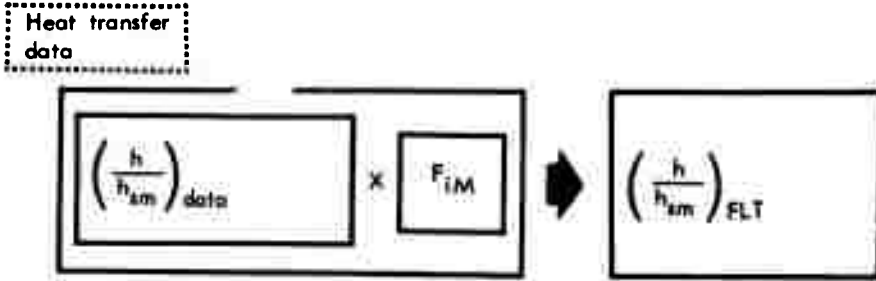


Shallow Convex Waves



Rectangular Cavity

The procedure that has been developed for extrapolating shallow convex wave and rectangular groove maximum laminar heating-rate wind-tunnel data to flight conditions is illustrated by the following sketch



A description of the extrapolation factor  $F_{iM}$  and methods for its development follows.

#### a. Shallow Convex Waves

In order to extrapolate the maximum laminar heat-transfer coefficients obtained in the wind tunnel to flight conditions, the measured values must first be normalized by smooth surface heating rates at the same distance. The ratio  $(h/h_{sm})_{data}$  is extrapolated to flight by the extrapolation factor  $F_{iM}$  which is defined as

$$F_{iM} = \frac{(\Delta\dot{q}/\dot{q}_{sm})_{FLT, R/\delta^*}}{(\Delta\dot{q}/\dot{q}_{sm})_{WT, R/\delta^*}} \quad (28)$$

The ratio  $(\Delta\dot{q}/\dot{q}_{sm})$ , where  $\Delta\dot{q} = \dot{q}_{max} - \dot{q}_{sm}$ , in equation (28) is determined using the following expression

$$\frac{R}{\delta^*_{sm}} = \left\{ .3 + \frac{1}{2.5[.78 + .84(i_w/i_o)] + \bar{q}} \right\} \left( \frac{\bar{q}}{1 - \frac{\bar{q}}{\pi\gamma[.78 + .84(i_w/i_o)]} \left[ \frac{(W/R)\sqrt{M_{e,n}^2 - 1}}{M_{e,n}^2} \right]} \right) \quad (29)$$

where

$$\bar{q} = \frac{\dot{q}_{\max} - \dot{q}_{sm}}{\dot{q}_{sm}} \quad (30)$$

The derivation of equation (29) is presented in reference 19.

Curves showing solutions for  $\bar{q}$  on a sharp flat plate in air are presented in figure 28 as a function of  $R/\delta_{sm}^*$  and  $[W/R(M_{e,n}^2 - 1)^{0.5}/M_{e,n}^2]$ . These curves are presented for values of the effective specific heat ratio,  $\gamma_{\text{eff}}$  equal to 1.4 and 1.15. The parameter  $R/\delta_{sm}^*$  is evaluated using the expression

$$\frac{R}{\delta_{sm}^*} = \frac{hR}{(h\delta^*)_{sm}} \quad (31)$$

where  $h_{sm}$  is a flat-plate heat-transfer coefficient evaluated at a distance equal to that between the leading edge and the center of the wave,  $R$  is the maximum height of the wave, and the product  $h\delta^*$  is obtained using the procedure outlined in Section III-3. Edge Mach number in the parameter  $[W/R(M_{e,n}^2 - 1)^{0.5}/M_{e,n}^2]$  is evaluated in the plane normal to the wave using the expression

$$M_{e,n} = M_e \cos(\Lambda)_{\text{wave}} \quad (32)$$

The extrapolation factor  $F_{iM}$  for waves on a sharp flat plate is evaluated using values obtained from these curves. The method of extrapolation presented here for waves takes into account the physical characteristics of the wave with respect to the predicted depth of the displacement thickness for both hot-wall and cold-wall conditions.

Absolute values of the maximum heating rate predicted for flight conditions can be obtained by determining  $h_{sm}$  using reference 2 for the flight condition of interest.

No reliable analytic or empirical method exists for extrapolating turbulent wind-tunnel data to flight conditions for waves.

#### b. Rectangular Grooves

Extrapolation of maximum laminar heating-rate measurements obtained in an air-nitrogen wind tunnel for rectangular grooves is accomplished by first normalizing this heating rate using smooth-body heat-transfer coefficients evaluated at a distance equal to that between the leading edge and the center of the groove. The extrapolation factor  $F_{iM}$  is defined as

$$F_{iM} = \frac{(h_{\max}/h_{sm})_{FLT}}{(h_{\max}/h_{sm})_{WT}} \quad (33)$$

where the ratio  $(h_{\max}/h_{sm})$  is evaluated using the empirical correlation expression for a rectangular groove that was first presented in reference 18. This correlation is expressed as

$$\frac{h_{\max}}{h_{sm}} = 1 + \left( 0.035 + \frac{0.1}{\sqrt{(W/y)}} \right) \frac{h_{sm} W Pr_w}{\mu_w c_{p,w}} \quad (34)$$

In equation (34),  $W$  is the width of the cavity,  $y$  is the depth of the cavity,  $h_{sm}$  is the heat-transfer coefficient on a smooth body evaluated at a location corresponding to the mid-point of the groove,  $Pr_w$  is the Prandtl number based on wall temperature and pressure,  $\mu_w$  is the viscosity and  $c_{p,w}$  is the specific heat at constant pressure evaluated at the wall temperature.

Curves are presented in figure 29 which represent solutions for equation (34) in terms of the width to depth ratio of the groove,  $W/y$ , and the parameter

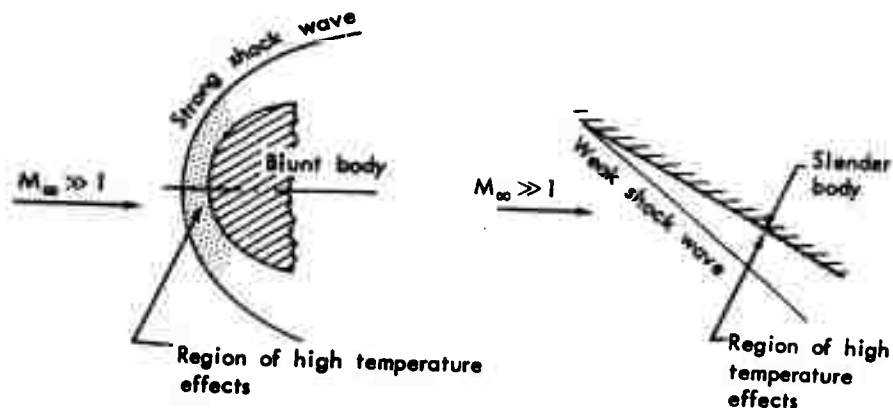
$$\frac{h_{sm} W Pr_w}{\mu_w c_{p,w}}$$

The extrapolation factor  $F_{iM}$  is formed by evaluating the ratio  $(h_{\max}/h_{sm})$  for values corresponding to  $h_{sm} W Pr_w / \mu_w c_{p,w}$  at wind-tunnel or flight conditions.

No reliable analytic or empirical method exists for extrapolating turbulent wind-tunnel data to flight conditions for grooves.

## 6. CHEMICAL NONEQUILIBRIUM EFFECTS ON EXTRAPOLATION FACTORS

For the free-stream conditions of present day wind tunnels and in the orbital reentry corridor, flow kinetic energy is the greater part of the total energy of the gas. When this gas is brought to rest by compression, the flow energy is converted into thermal energy resulting in a considerable increase in temperature, molecular excitation, and dissociation. This compression may be a result of crossing a strong shock wave generated by a blunt body, or of viscous interaction in the boundary layer of a slender body. These two types of compression are illustrated in the sketch below:



Both shock compression and compression due to viscous interaction can be present on blunt bodies having high fineness ratios; that is, bodies that are long compared to their nose or leading edge diameter.

The compressed gas may be in an equilibrium or a nonequilibrium state, depending upon the magnitude of the compression and the resulting thermal energy density. Gases in equilibrium can be treated with confidence. On the other hand, thermochemical nonequilibrium effects on an otherwise well-defined flow field are difficult to assess rigorously and are treated analytically with less confidence. In order to use analytic methods in the present analysis, the flow fields enveloping the geometric elements described in the previous discussion have been simplified. The simplifications required preclude an analytic treatment of thermochemical nonequilibrium effects on the extrapolation factors developed for these elements. However, general discussion of how the extrapolation factors may be affected by thermochemical nonequilibrium is included in this section.

#### a. Blunt Bodies

The probability of equilibrium flow over surface waves and grooves, control surfaces deflected into the stream, swept cylinder-flat plate combinations, and sharp delta wings at angles of attack greater than about 50-degrees, is greater for air-nitrogen wind-tunnel conditions than it is at flight conditions. As a result, heating rate predictions for flight, based on extrapolation factors presented in this report, may be higher than will actually be experienced at flight conditions.

Geometric elements, such as those listed above, could foster shock wave compression of a magnitude large enough to cause a nonequilibrium state to occur. Near the stagnation region, if the density rise across the shock is small, or the body radius is small, the gas may be closer to a frozen rather

than a nonequilibrium state. Actually, in this region, the gas is rapidly approaching an equilibrium state because of the increase in collision frequency. Yet, as the flow progresses away from the stagnation region, it undergoes a rapid expansion and could pass through a series of quasi-frozen states. In a quasi-frozen state, the collision rate is so small that the energy of dissociation released is negligible. It is shown in reference 31 that the reduction in the available energy can result in decreases on the order of 60% in heat transfer to the body compared to that which would occur for equilibrium flow-field conditions.

#### b. Slender Bodies

In air-nitrogen wind tunnels (excluding combustion-driven shock tunnels) boundary-layer temperatures on sharp delta wings never reach the high temperatures attained under flight conditions. As a result, nonequilibrium effects on sharp delta-wing wind-tunnel data are negligible.

Sharp delta wings at low angles of attack and at flight conditions, will cause flow compression through viscous interaction in the boundary layer, since the majority of the kinetic flow energy of the free-stream has been retained across the relatively weak shock wave generated by this geometry. As the flow compresses, temperatures can become high enough to cause dissociation of the molecules. Since sharp delta wing flow properties are similar to those for a sharp cone<sup>3</sup>, an examination of nonequilibrium gas-property effects on a sharp cone flow field will serve to indicate the trends to be expected in the case of a sharp delta wing.

For sharp cones, chemical nonequilibrium nonsimilar boundary-layer program calculations indicate that temperature gradients at the wall are less than would be expected for gases in chemical equilibrium as the flow progresses from the apex. This reduction in temperature gradient at the wall fosters changes in the specie concentration profile, which in turn leads to more specie diffusion.<sup>4</sup> Effects of gas specie diffusion on slender body heat transfer is discussed in reference 35. In that report, gas specie diffusion is shown to be of relatively greater importance in the slender body case than in the blunt body case. This is because the viscous layer of the slender body is much thinner near the wall. Decreases up to 15% in heat transfer due to gas specie diffusion on slender bodies might be expected based on the results of reference 35. This result does not agree with the results shown in reference 32 where chemical nonequilibrium effects on gas specie diffusion was shown to increase heating slightly. However, in that report, the slight increase shown was offset by the decrease resulting from the decrease in the temperature gradient at the wall with increasing streamline length. As a result, the net effect on heat transfer for slender bodies is small.

---

<sup>3</sup> See Appendix B.

<sup>4</sup> A more detailed discussion is contained in references 32, 33, and 34.

### c. Effects of Catalytic Wall

By definition, a catalytic wall fosters recombination of dissociated gas molecules in proximity to the wall, thus releasing the energy absorbed in dissociation. Heat transfer to surfaces enveloped in a flow field that is dissociated is therefore a function of wall catalycity.

For the slender bodies considered in this report, the effect of wall catalycity on heat transfer is always small, since the degree of dissociation is small for both flight and wind-tunnel conditions. On the other hand, a significant increase in nonequilibrium heat transfer to blunt bodies can occur because flow compressed by a strong shock wave can cause a high degree of molecular dissociation. These molecules tend to recombine in proximity to a catalytic wall. It is indicated in reference 32 that for blunt bodies in a highly dissociated flow field, a noncatalytic wall can reduce heat transfer at the stagnation point by as much as 75% in comparison to a catalytic wall.

Increases in heating that can be attributed to catalycity has been accounted for in the extrapolation factors presented in this report. All calculations were made for a fully catalytic wall, and apply to wind-tunnel data measured on models that have highly catalytic surfaces.

## SECTION IV

### CONCLUDING REMARKS

One purpose of this analysis was to evaluate the capability of operational ground facilities to simultaneously simulate the free-stream Mach number, Reynolds number, Knudsen number, Lewis number, and enthalpy (velocity) that will occur during hypersonic reentry. It was found that only free-stream Mach number, free-stream Reynolds number, free-stream Knudsen number, and boundary-layer edge Lewis number are simulated adequately in present-day facilities. Flight condition boundary-layer edge Mach number and Reynolds number, two parameters that must be simulated exactly to insure similar boundary-layer growth at ground-test conditions, are not simulated well in present-day ground facilities. The largest deficiency, however, is due to the failure to adequately simulate high Mach number flight enthalpy conditions. Present-day facilities large enough for development testing have the capability to run at only about half the velocity occurring during the hottest portion of reentry.

The primary purpose of this analysis was to develop extrapolation factors using existing analytic methods that account for any simulation deficiencies occurring in present-day ground facilities. These factors were to be used in the application of ground-test data to reentry vehicle design and were to be developed for four geometric elements that are representative of portions of a reentry vehicle. The elements are a sharp unyawed delta wing, deflected control surfaces in compression and expansion, shallow convex waves and rectangular grooves, and a yawed circular cylinder intersecting a sharp flat plate.

Extrapolation factors have been developed for these four elements that are based on existing analytic methods. However, it was found during the present analysis that the best analytic methods for these elements are only approximate, and that for the groove the best method is empirical. In addition, existing methods generally neglected real-gas effects.

A new flow-field method was developed for a thin-sharp-unyawed delta wing. In this method, flow-field gas properties in proximity to the centerline of the delta wing are computed using a new similarity parameter that accounts for both real-gas and leading-edge sweep-angle effects. Away from the centerline, at angles of attack greater than about 50 degrees, the present delta-wing method is dependent upon correlations of the approximate analytic method presented in reference 36.

The delta-wing flow-field method presented here postulates that a parting line exists on a sharp delta wing at angles of attack between about 30 to 60 degrees that accounts for both in-flow and out-flow occurring on the surface simultaneously. The present analysis indicates that maximum spanwise heating

occurs along this parting line. The reason for this is that streamline divergence along this line is large and spanwise pressure is at its maximum. On the outboard side of the parting line, the streamlines diverge at an increasing rate thinning the boundary layer, but the pressure decreases even more rapidly. The combined result is a decrease in heat transfer in the outboard direction. On the inboard side, the streamlines diverge at a decreasing rate thickening the boundary layer and causing a decrease in heating to occur in the inboard direction.

The present delta-wing method uses the two best available approximate analytic methods (i. e., references 18 and 36) as a basis at low and high angles of attack. This method bridges the solutions of the two analytic methods using an interpolation technique between the angles of attack where they are no longer valid. Thus, this report presents a unified inviscid flow-field solution for a sharp delta wing in the range of angles of attack between zero degrees and about 60 degrees. It also presents a means of determining gas properties at the centerline of a sharp delta wing in a simple manner. Further improvement in determining sharp delta wing flow properties will require a major effort.

Centerline heating rates predicted using the unified inviscid flow-field solution presented in this report are generally higher between about 15° and 45° angle of attack than those presented in reference 2. This difference is due to the manner in which the divergence parameter,  $n$ , is evaluated in the present analysis.

Extrapolation factors based on this method predict differences in delta-wing centerline heating rates, between wind tunnels and flight, generally less than about 15%. However, using the parting-line theory, maximum differences on the order of 20-40% are predicted at spanwise locations off the centerline at angles of attack greater than about 40-degrees.

During the present analysis, an attempt was made to perform a separated boundary-layer flow analysis on a compression flap using the method of reference 37 as documented in reference 38. It was found that useful solutions could not be obtained for  $Y_{eff}$  less than about 1.36. However, it is felt that this was due to the limitations imposed by using the incipient separation profiles that were published in reference 38 which are curve fits of similarity solutions of reference 39. The basic method of reference 37 could possibly be used in a study to indicate the differences in separation lengths, reattachment pressure, and reattachment heat transfer at wind-tunnel and flight conditions if separation profiles for a real gas are used.

Pressure and heating rate distributions are presented in this report for expansion surfaces that are dependent only upon the distance from the hinge line. The present analysis indicates that the average pressure level over the flap will be higher than that predicted using inviscid flow theory, the magnitude

of the difference increasing with increasing deflection angles. The distributions also indicate that differences between surface pressures on the expansion surface obtained in a wind tunnel and those obtained in flight may be greater than 100% over some portion of the flap. There are two reasons for this: first, the total pressure drop for a given deflection angle is greater in flight and second, the boundary layer at the hinge line in flight is much thicker than it is in a wind tunnel. Additional analytic analysis is required to more precisely determine the effects of the boundary layer on the pressure distribution and conversely, the effects of the pressure distribution on the boundary-layer development.

Further development of the analytic method for predicting heat-transfer to yawed circular cylinders intersecting a sharp flat plate is required. The method used in this document predicts a large discontinuity in pressure and heat-transfer when the shock wave fostered by the cylinder detaches from the loci of intersection with the plate. This is reasonable, but methods are required to establish how to interpolate between pressures and heating rates that occur when the shock wave is attached at wind-tunnel conditions and detached at flight conditions.

Differences between wind-tunnel and flight heating rates for the cylinder-plate combination, for surface waves and grooves, and for deflected flaps have been found to be extremely geometry dependent. Extrapolation factors presented in this report vary from unity to values exceeding 50% for some conditions.

In general, the methods chosen for development of the extrapolation factors for these four geometric elements reflect the present state-of-the-art. As more precise, or better substantiated, analytic methods become available, new extrapolation factors should be developed. The procedures developed in the present analysis and presented in this report should be applicable at that time.

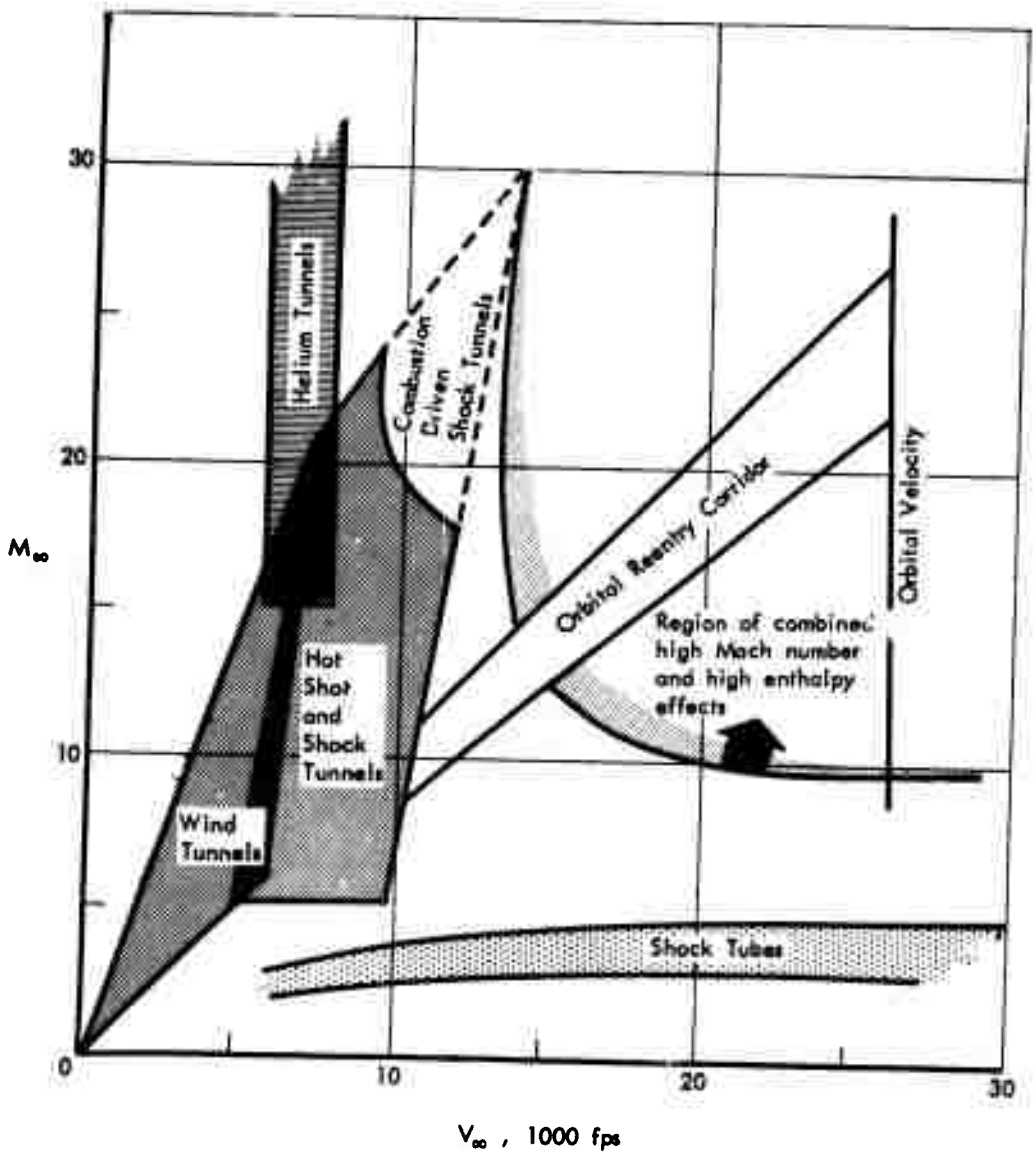


Figure 1: VELOCITY SIMULATION IN GROUND FACILITIES

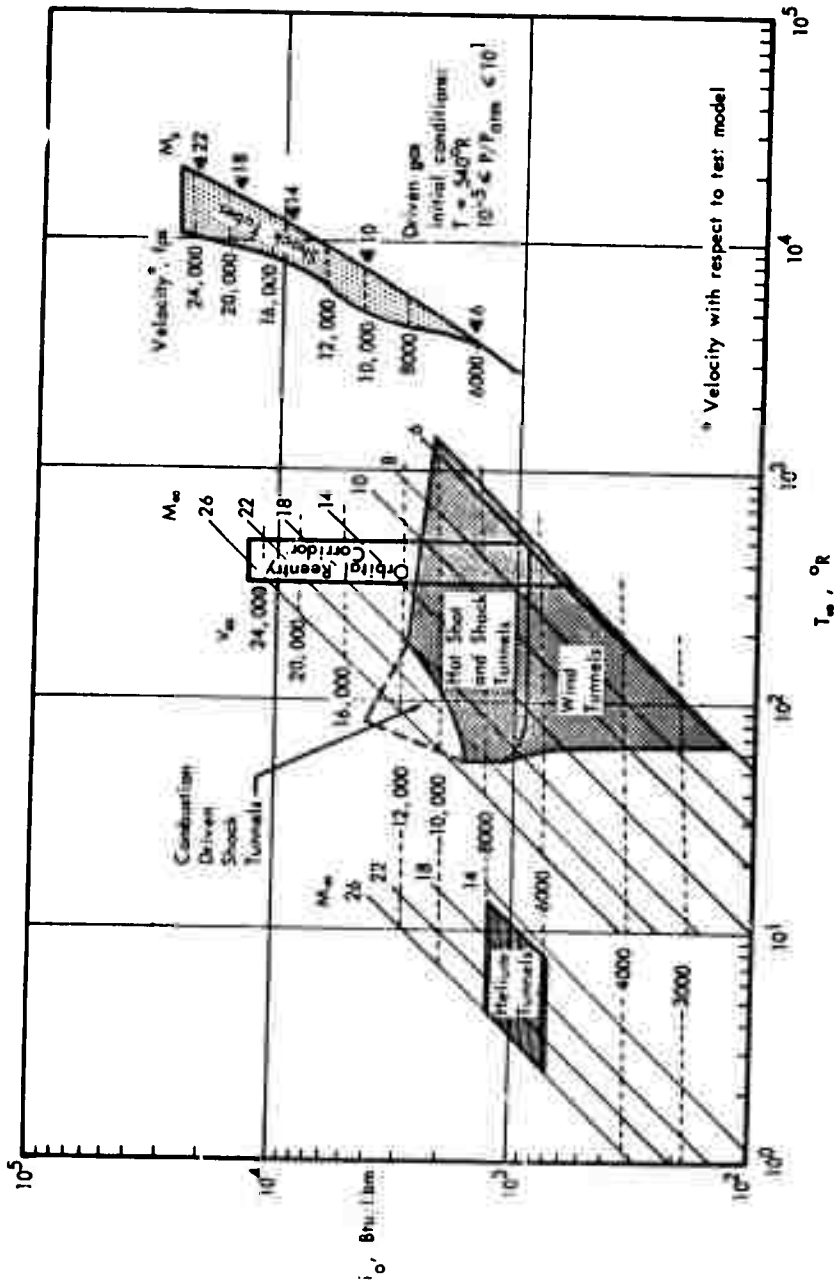


Figure 2: ENERGY SIMULATION IN GROUND FACILITIES

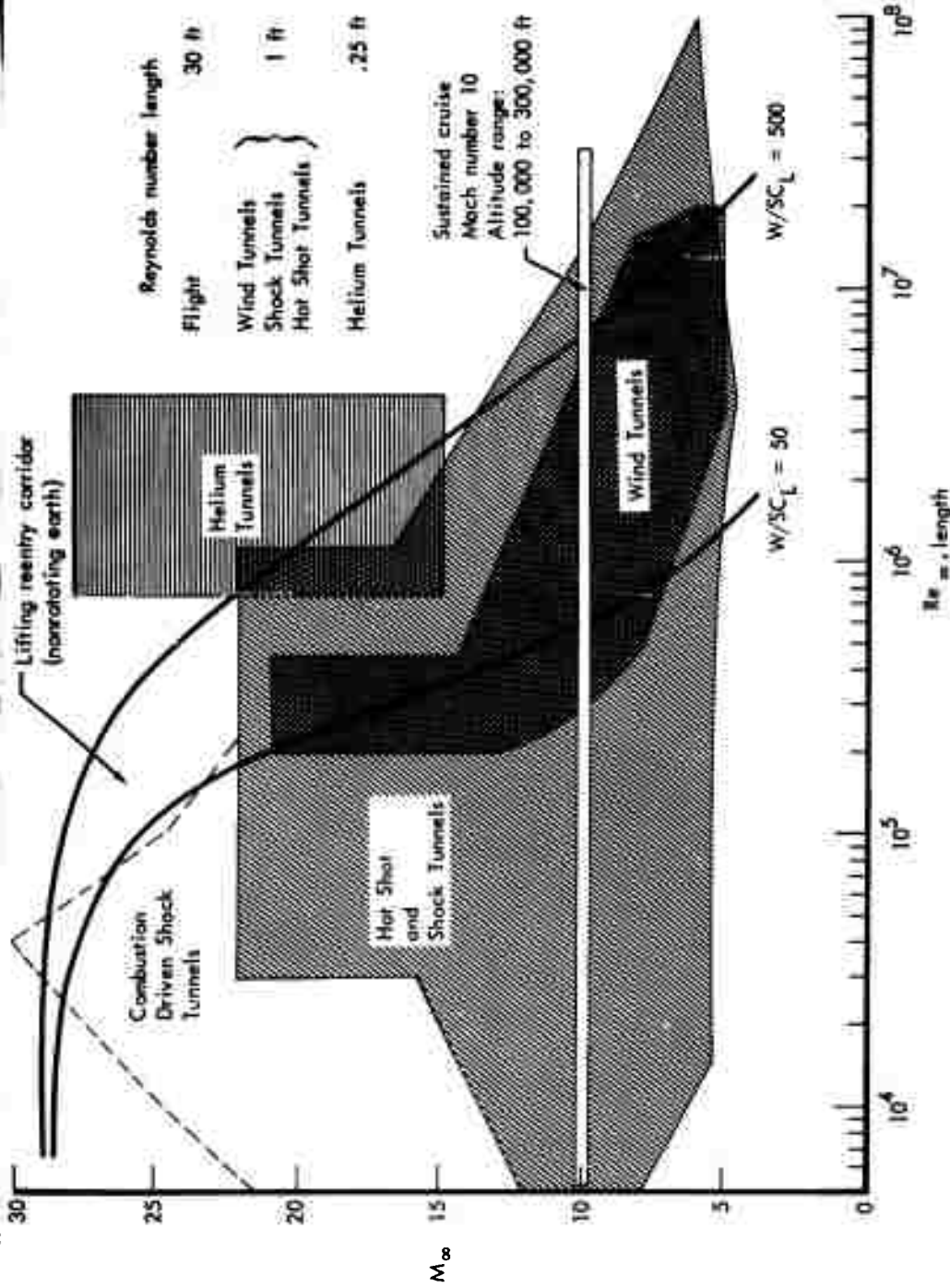


Figure 3: FREE-STREAM REYNOLDS NUMBER SIMULATION IN GROUND FACILITIES

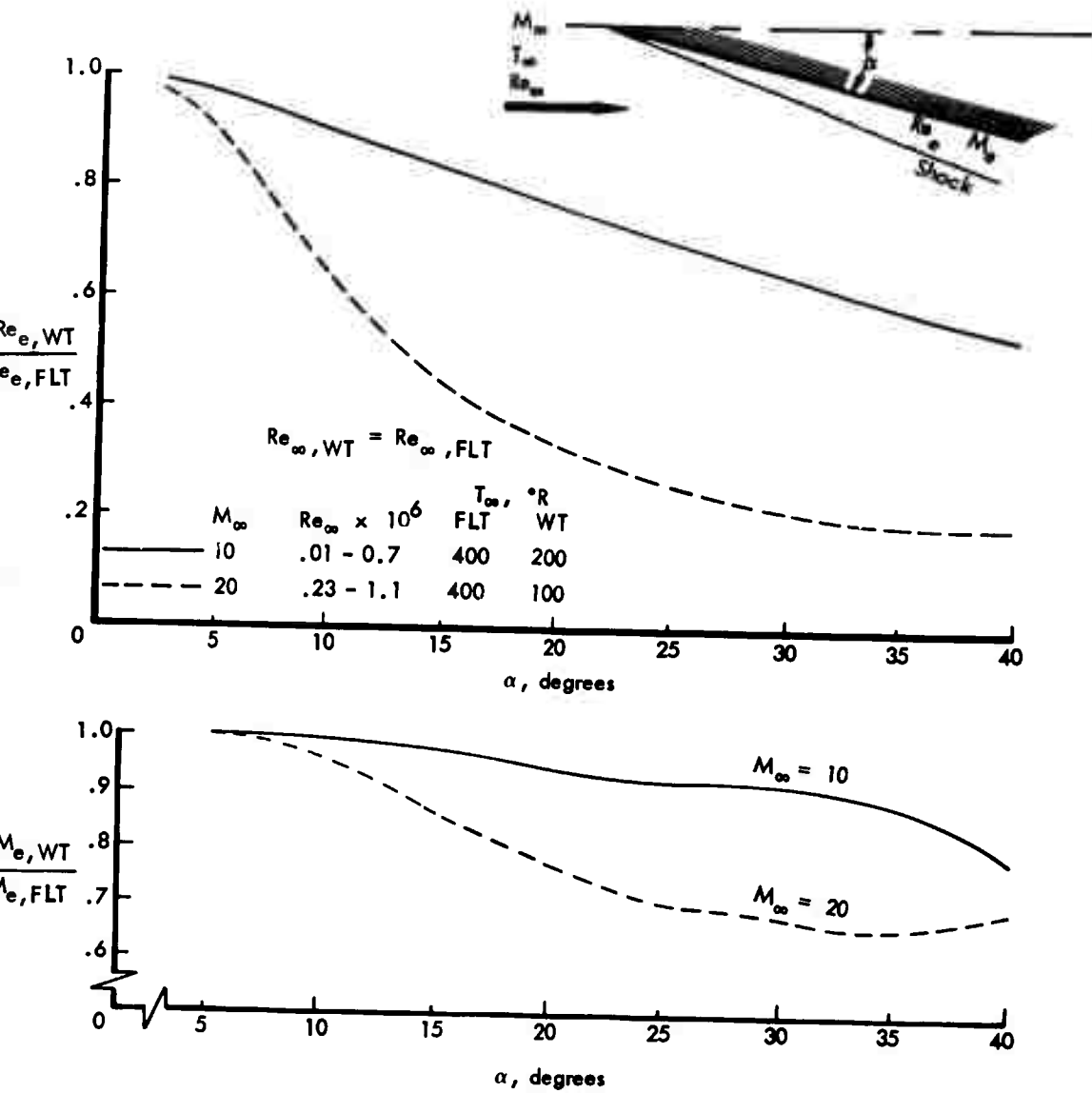
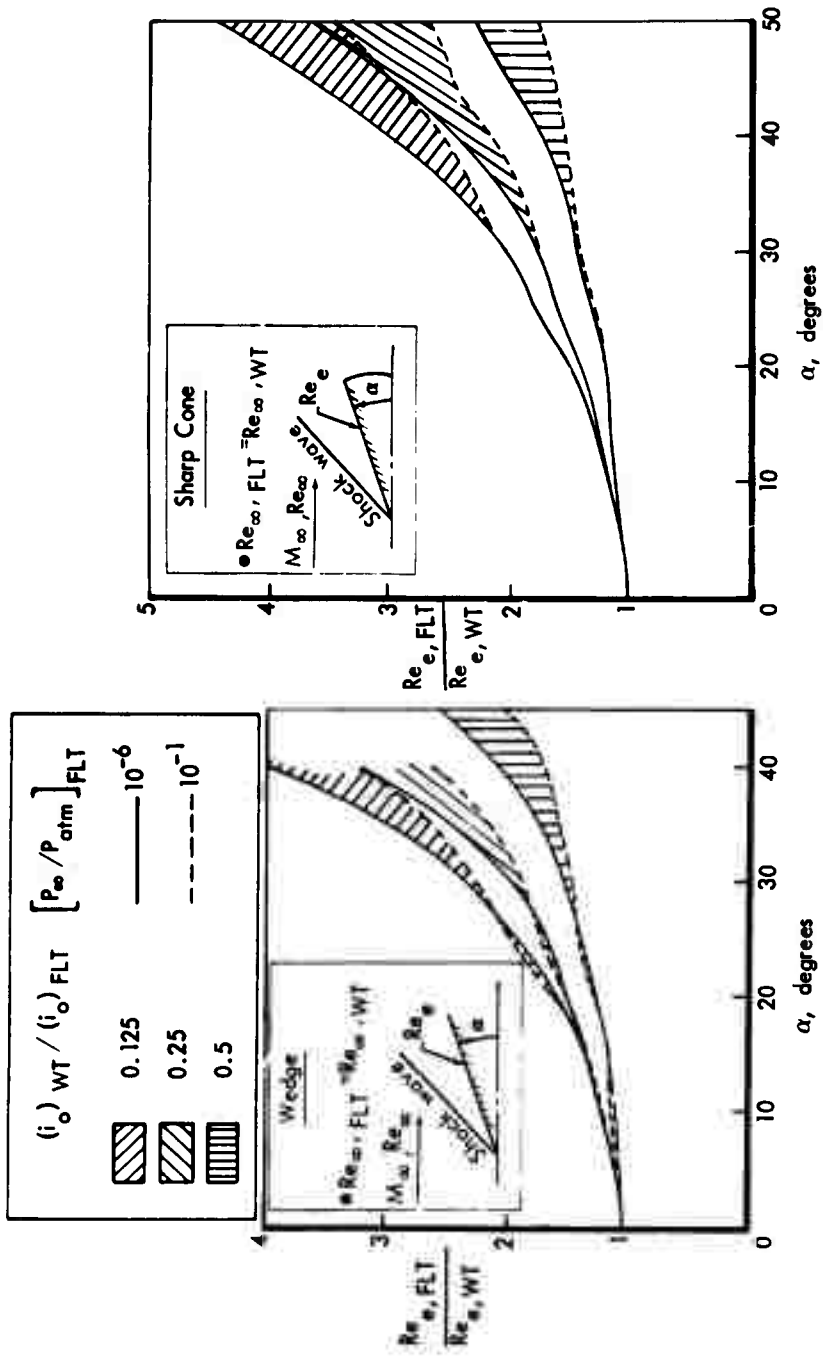
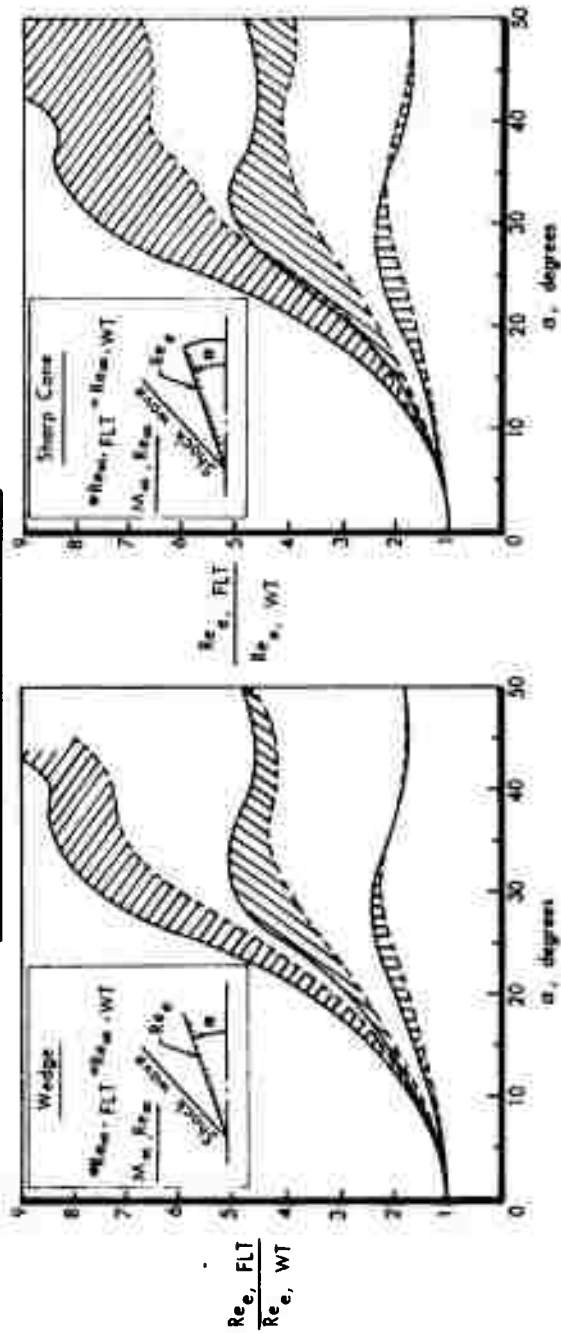
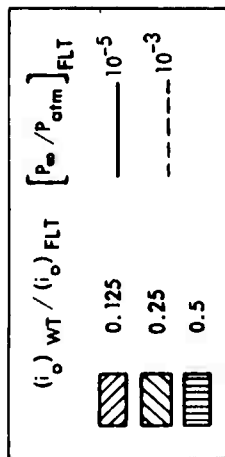


Figure 4: REYNOLDS NUMBER AND INVISCID MACH NUMBER COMPARISON ON A SHARP FLAT PLATE



a)  $M_\infty = 10$

Figure 5: REAL-GAS EFFECTS ON REYNOLDS NUMBER FOR WEDGES AND SHARP UNYAWED CONES



b)  $M_\infty = 20$

Figure 5: Concluded

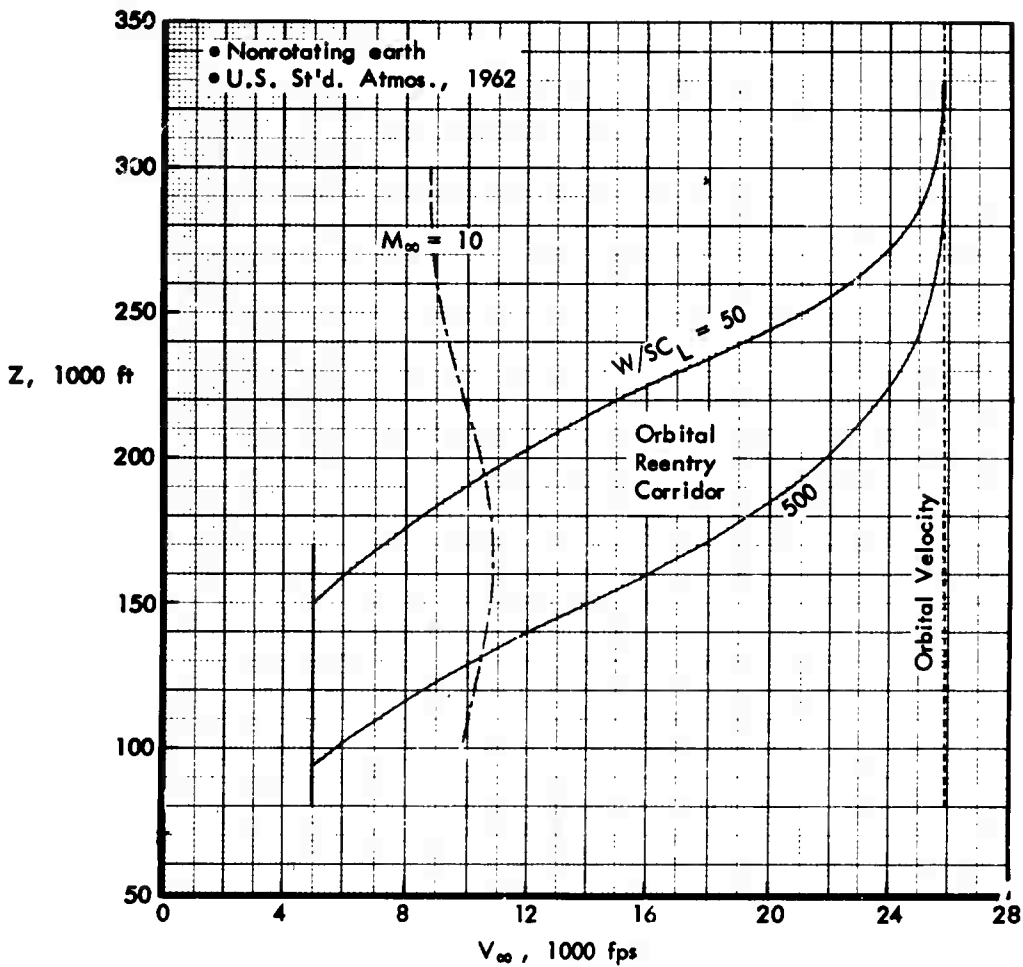


Figure 6: ORBITAL REENTRY CORRIDOR FOR LIFTING VEHICLES

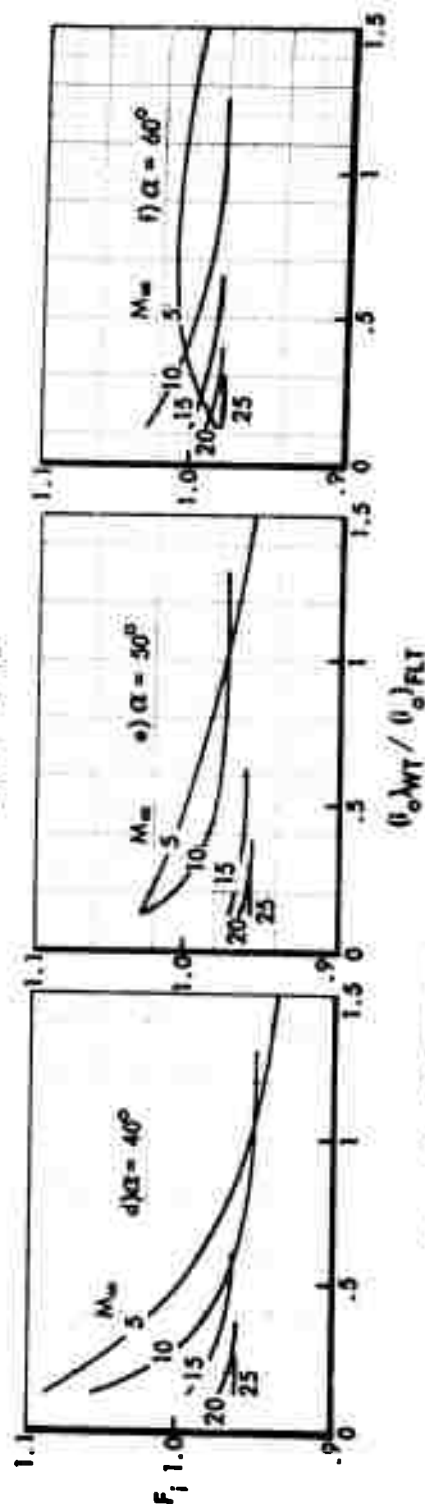
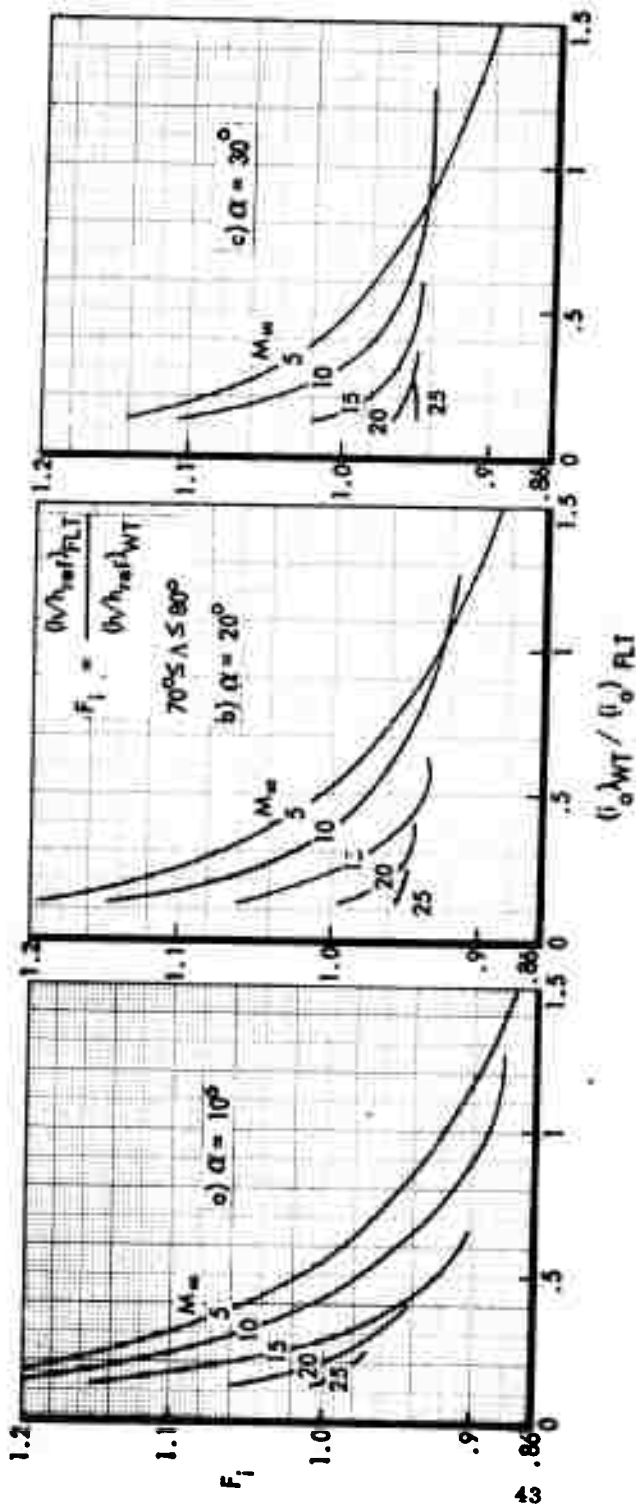


Figure 7: SHARP DELTA WING LAMINAR EXTRAPOLATION FACTORS FOR

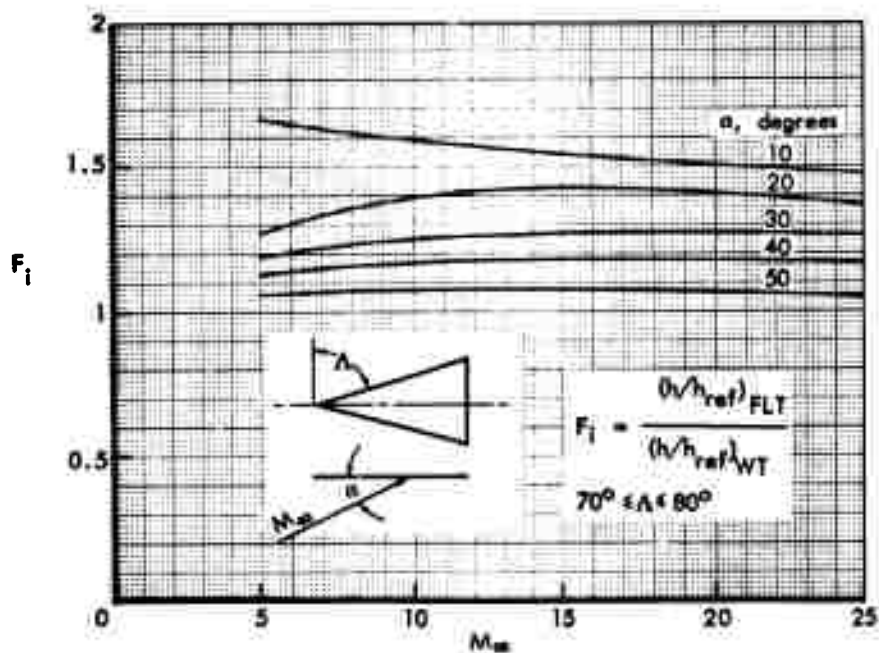


Figure 8: SHARP DELTA WING LAMINAR EXTRAPOLATION FACTORS FOR HELIUM GROUND FACILITIES

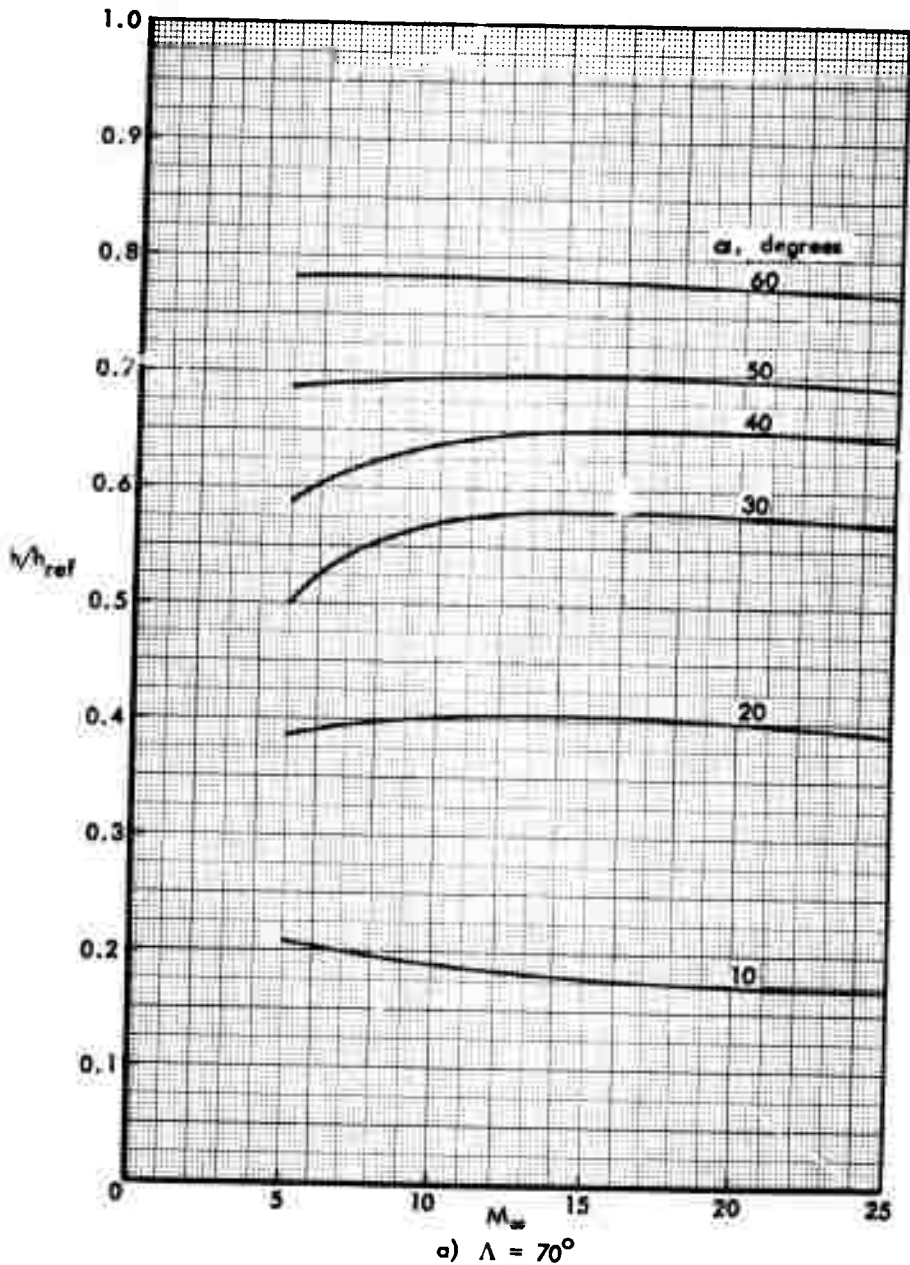
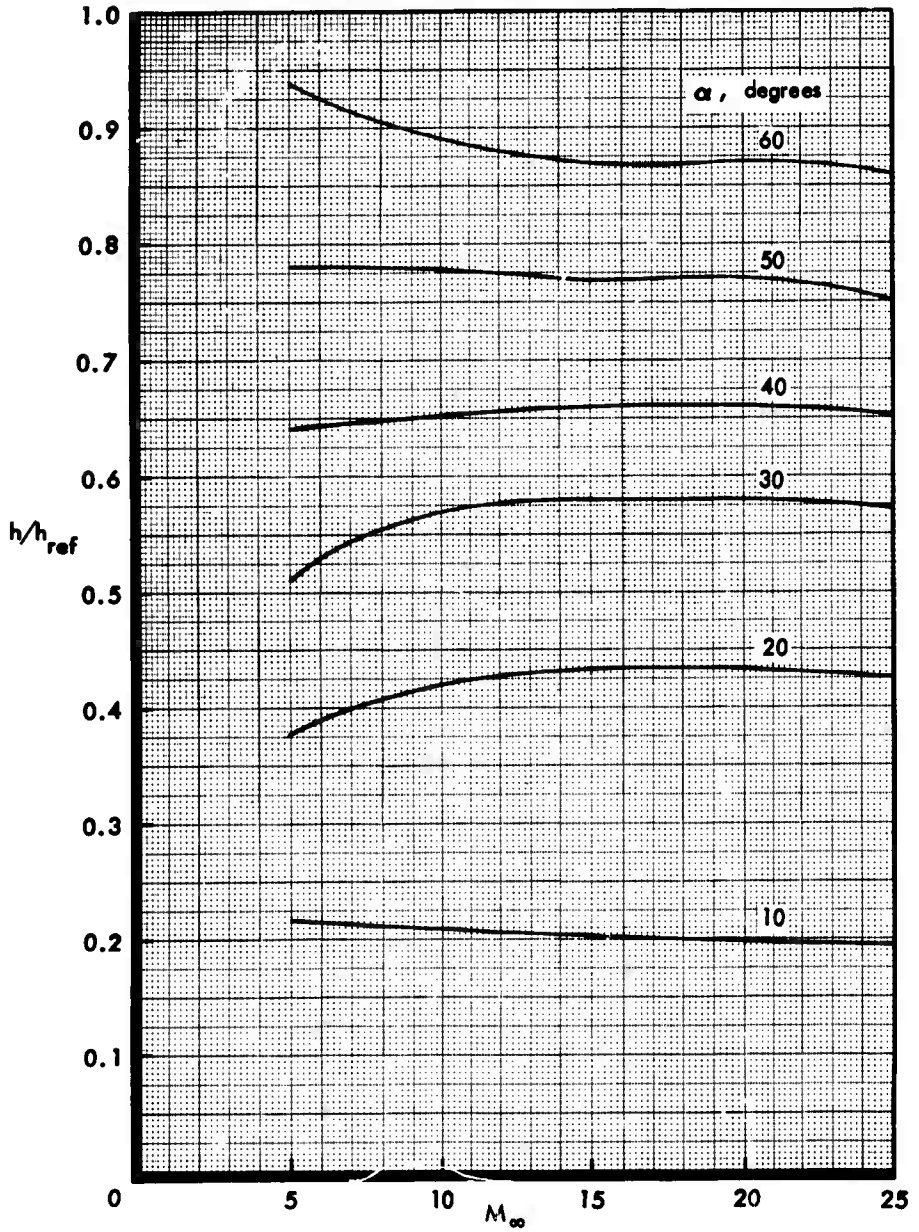


Figure 9: SHARP DELTA WING CENTERLINE LAMINAR HEATING FOR FLIGHT CONDITIONS



b)  $\Lambda = 75^\circ$

Figure 9: Continued

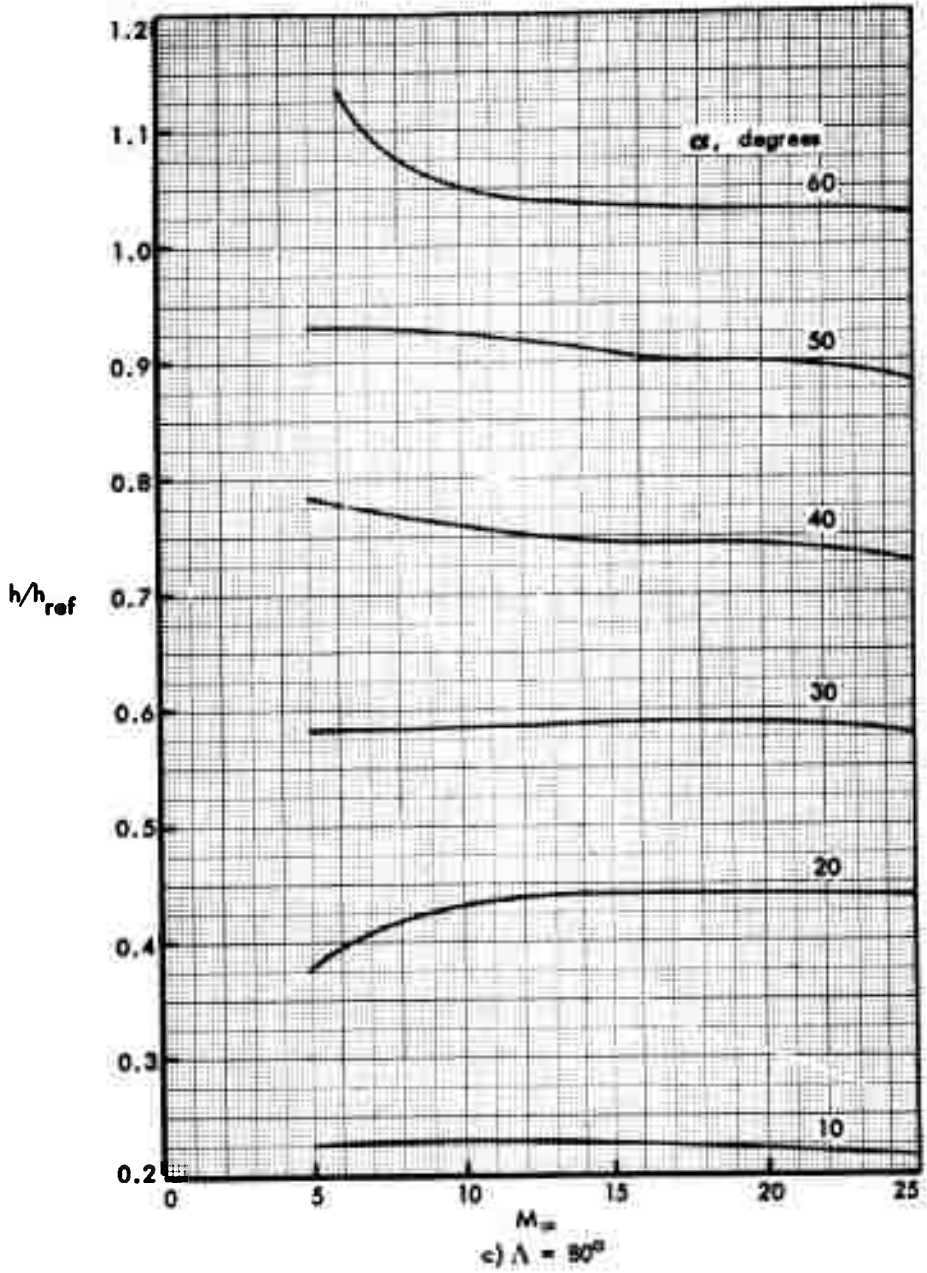


Figure 9: Concluded

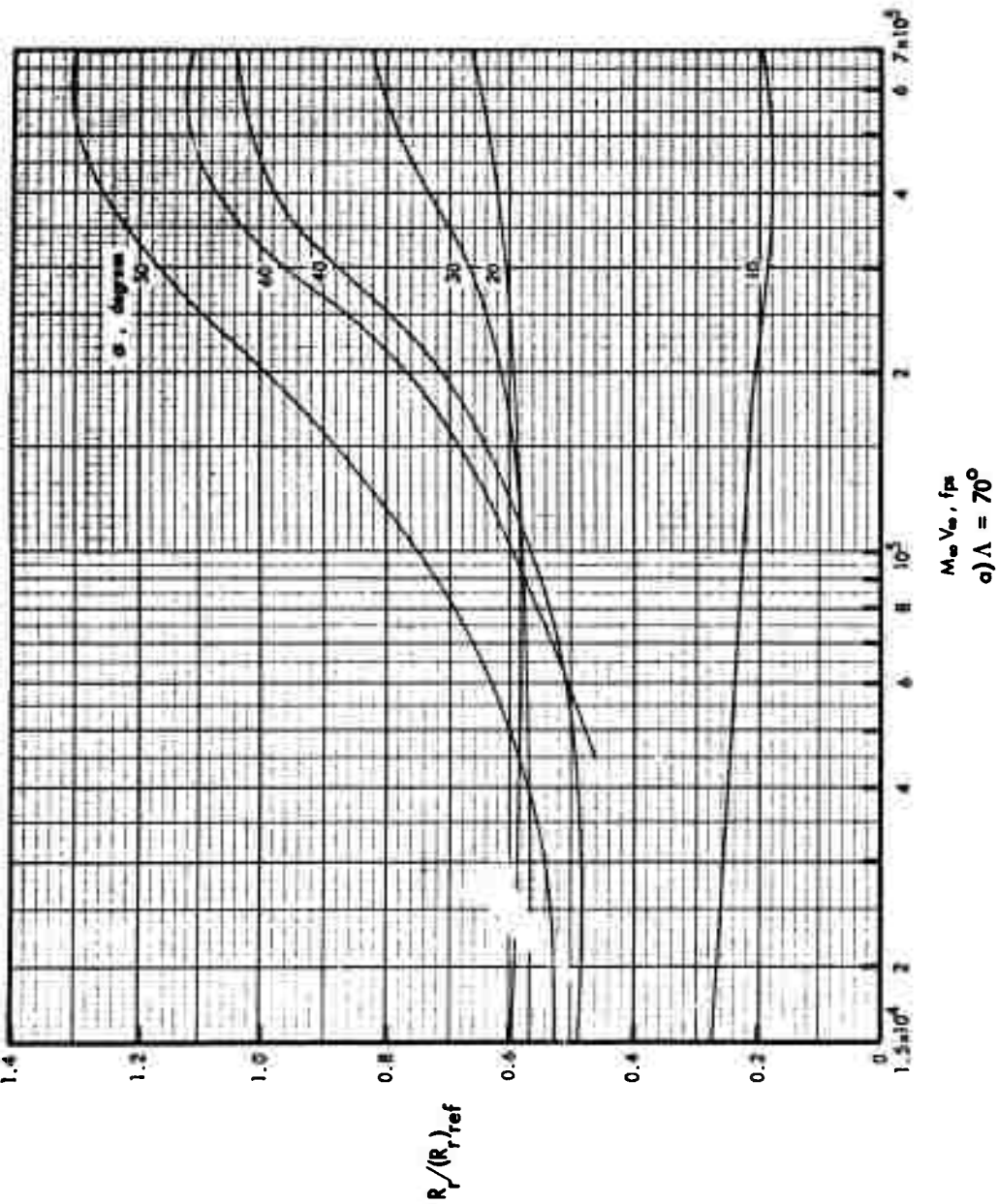
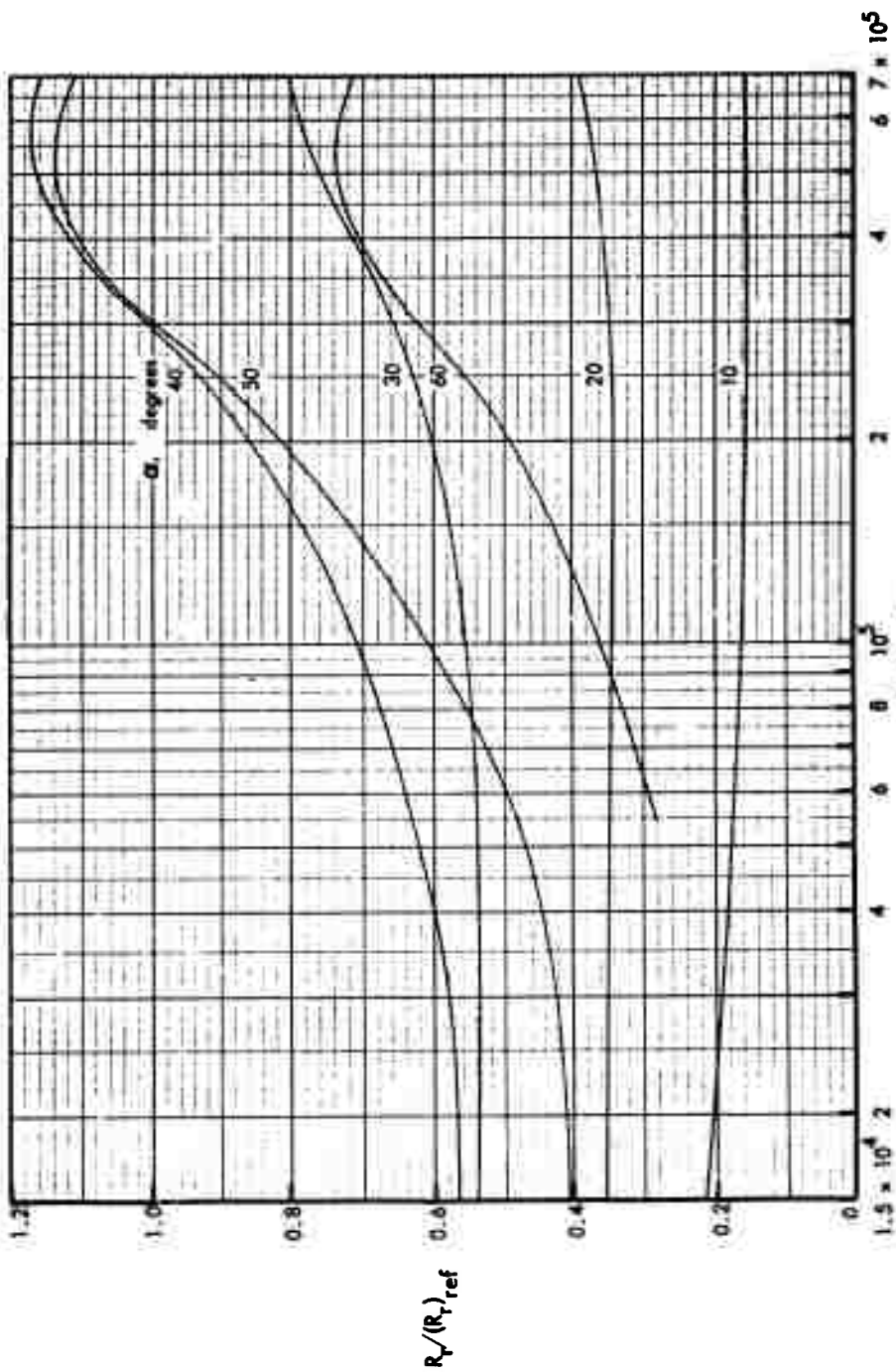


Figure 10: SHARP DELTA WING CENTERLINE REYNOLDS NUMBER DISTRIBUTION



$M = V_{\infty} / c_{ref}$

b)  $\Delta = 75^\circ$

Figure 10: Continued

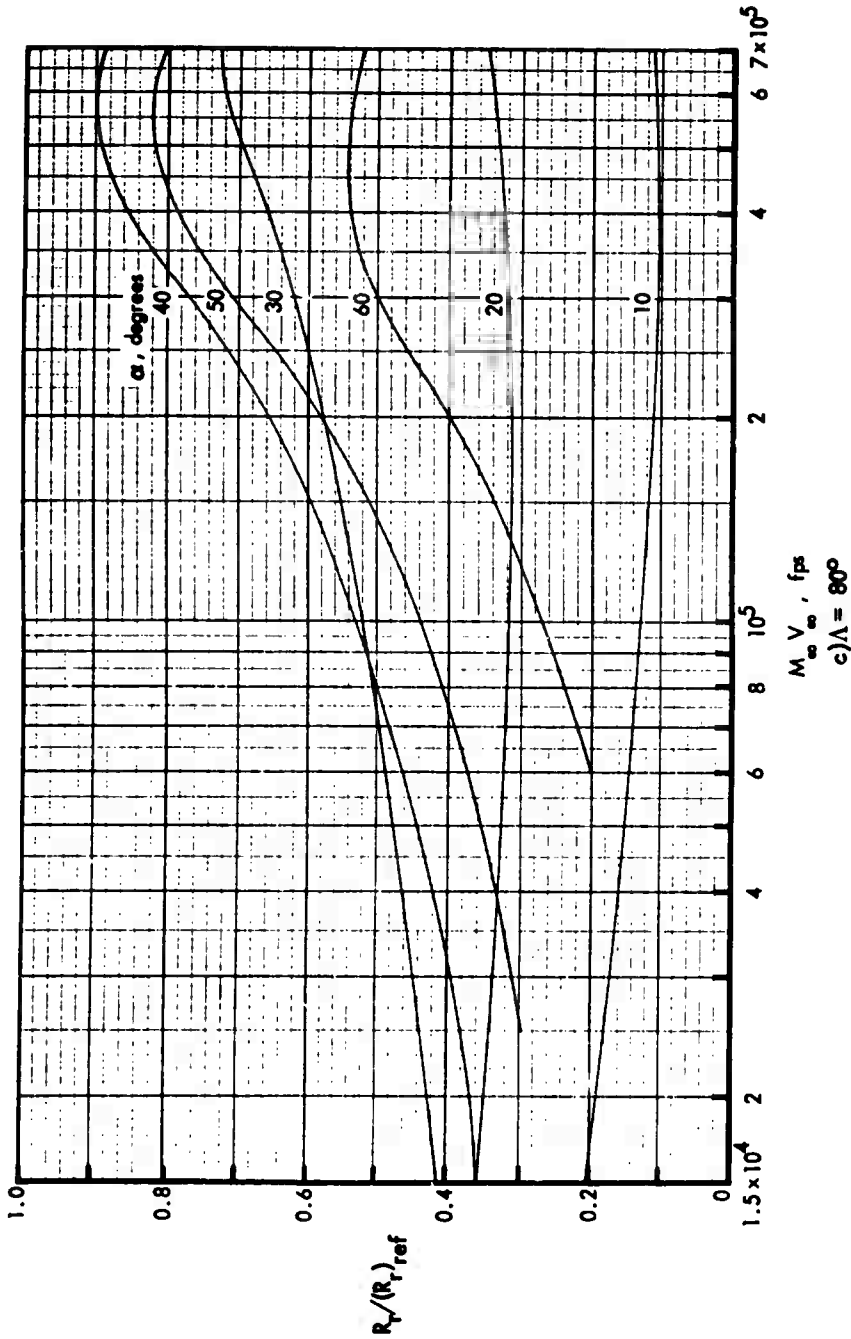


Figure 10: Concluded

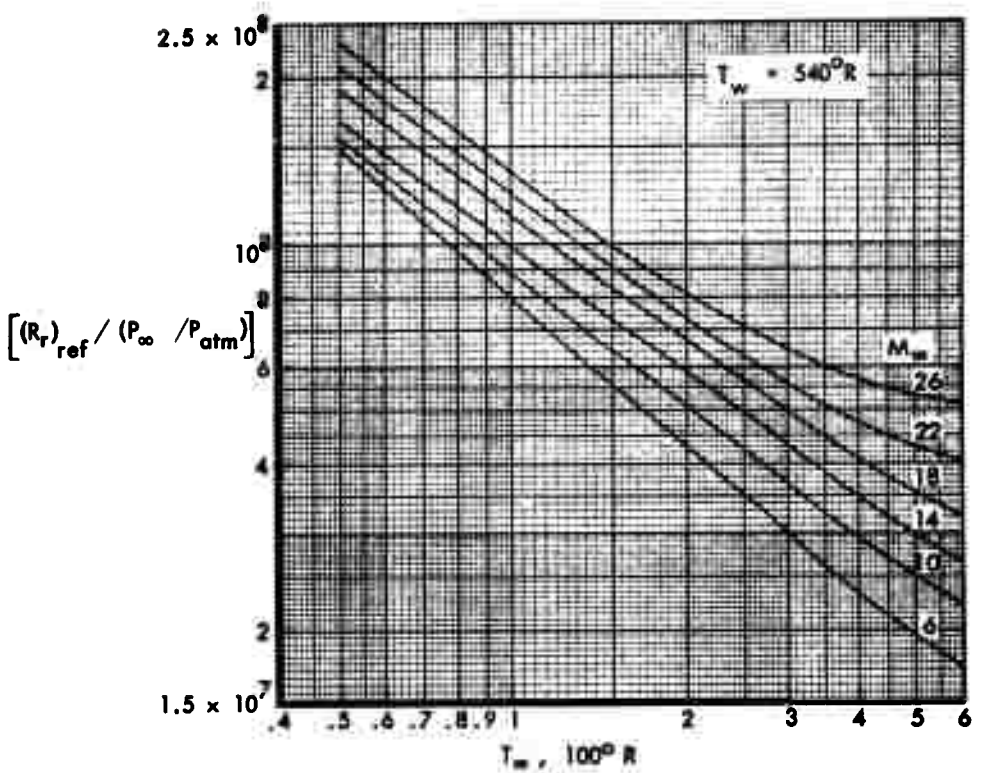


Figure 11: REFERENCE REYNOLDS NUMBER FOR AIR AND NITROGEN GROUND FACILITIES

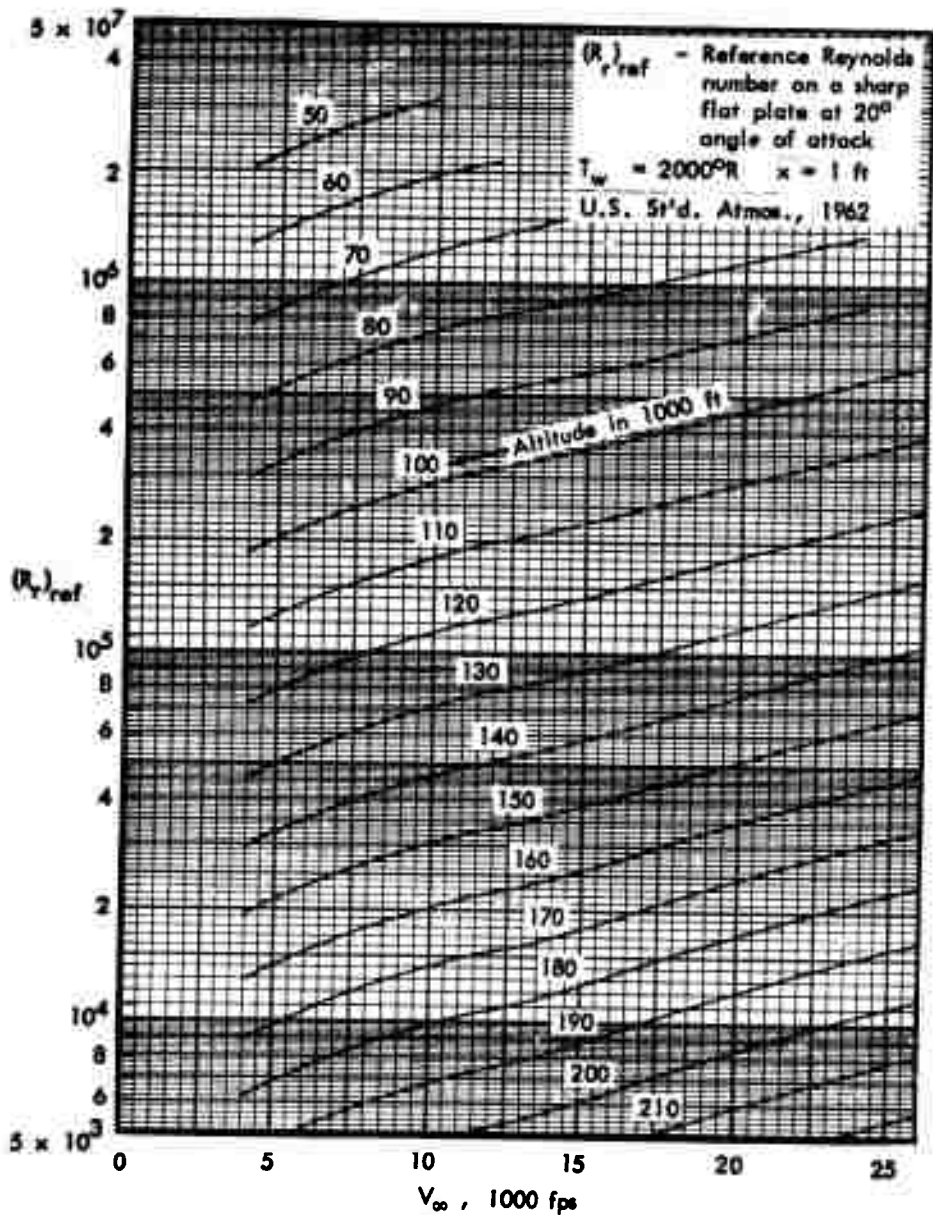


Figure 12: REFERENCE REYNOLDS NUMBER FOR FLIGHT CONDITIONS

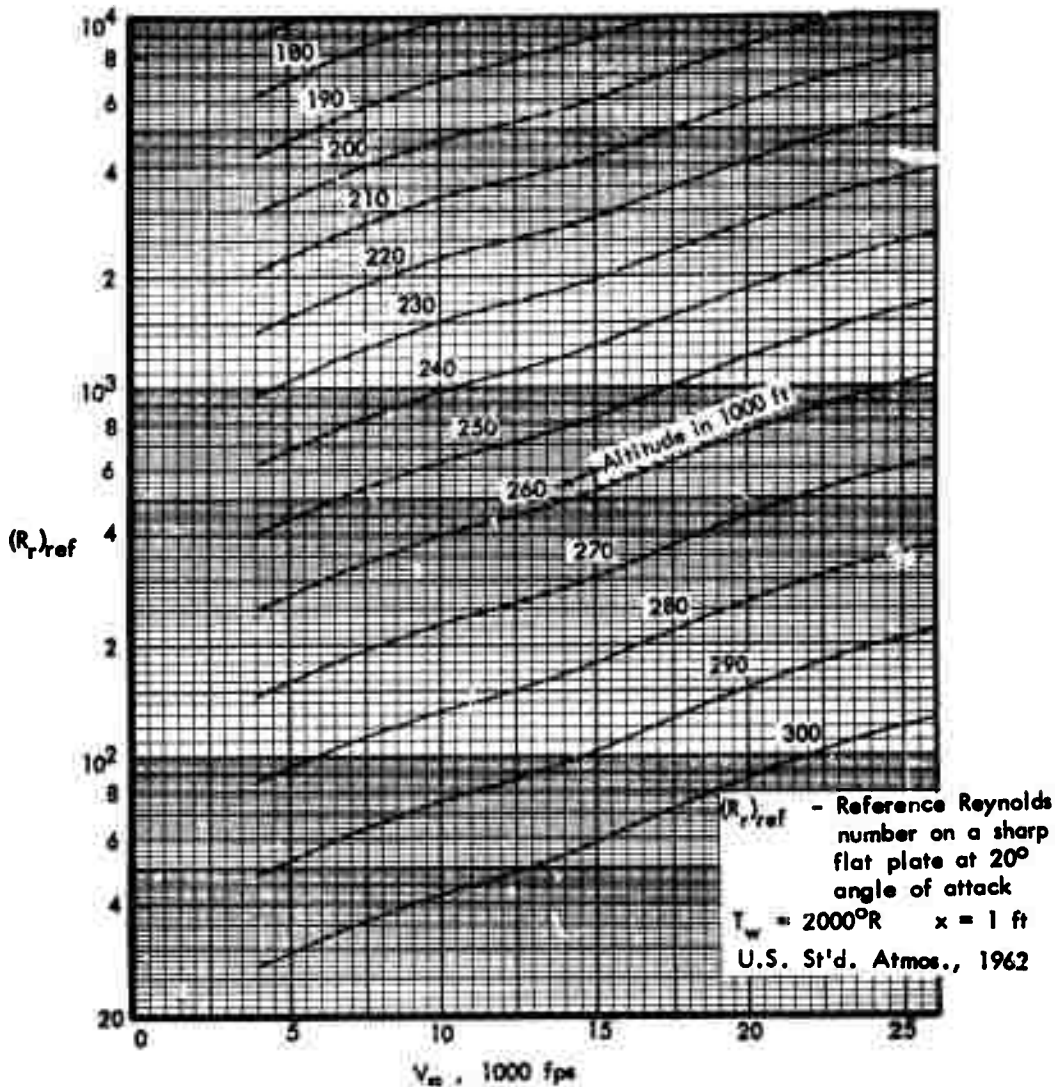


Figure 12: Concluded

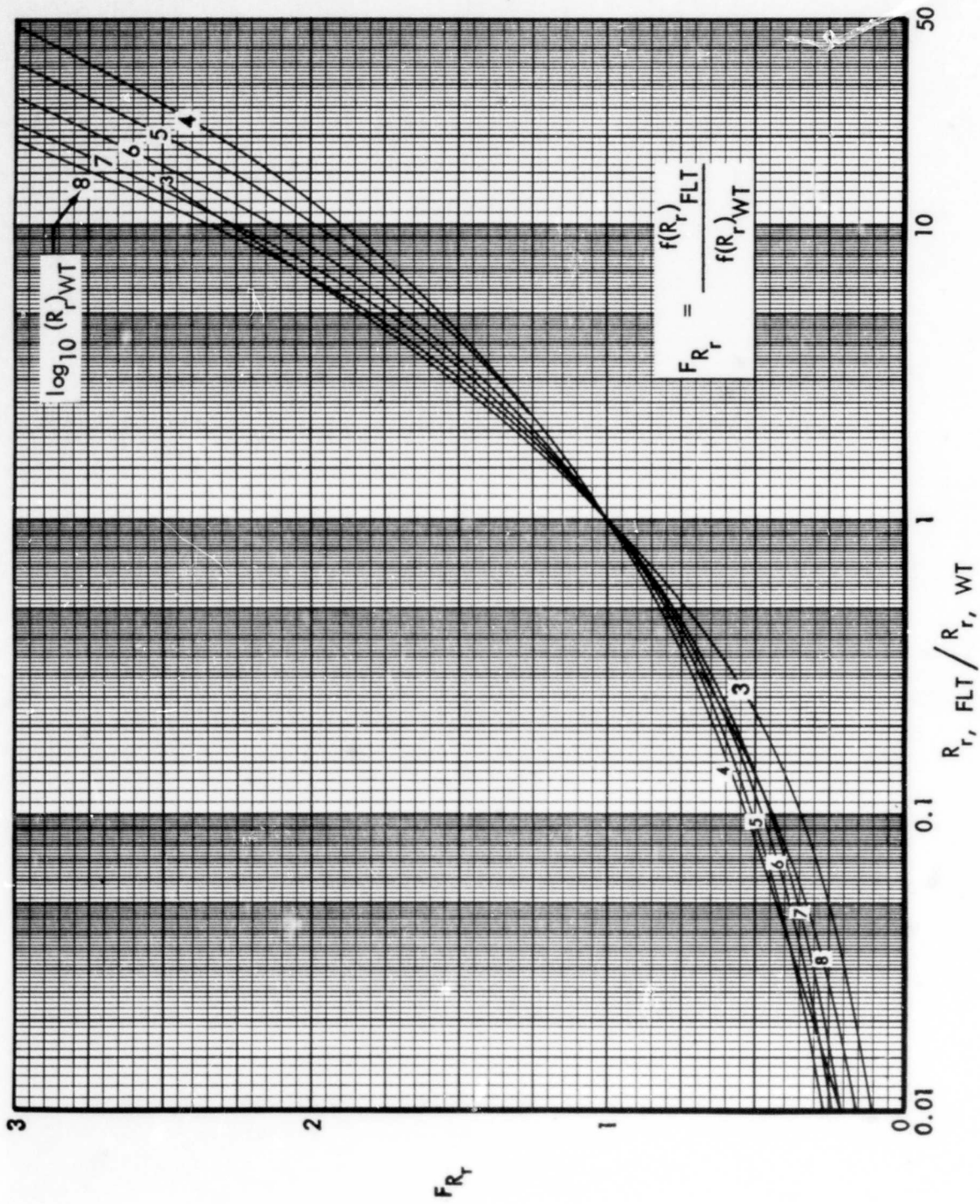
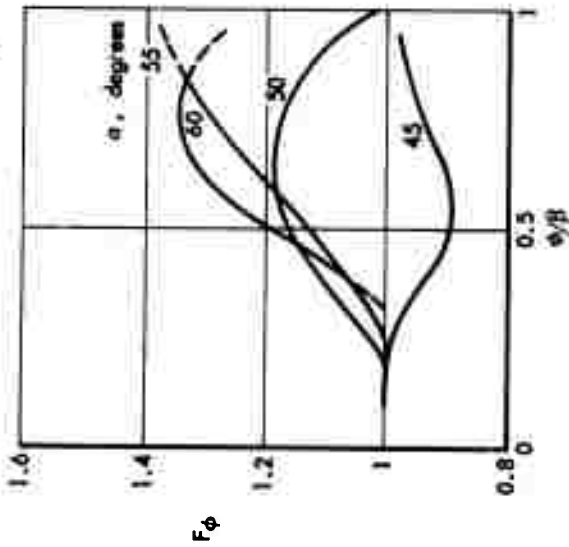


Figure 13: REYNOLDS NUMBER FUNCTION

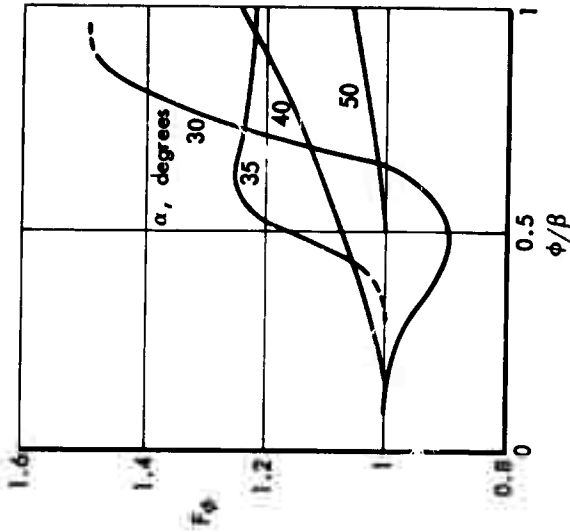


●  $\frac{i_{\alpha, WT}}{i_{\alpha, FLT}} = 0.25$

●  $M_{\infty} = 20$

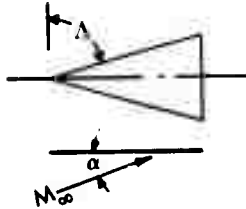


a)  $\Lambda = 70^\circ$



b)  $\Lambda = 80^\circ$

Figure 14: SHARP DELTA WING SPANWISE LAMINAR EXTRAPOLATION FACTORS



•  $\alpha_{M=1}$  - angle of attack at which lower surface centerline flow is sonic

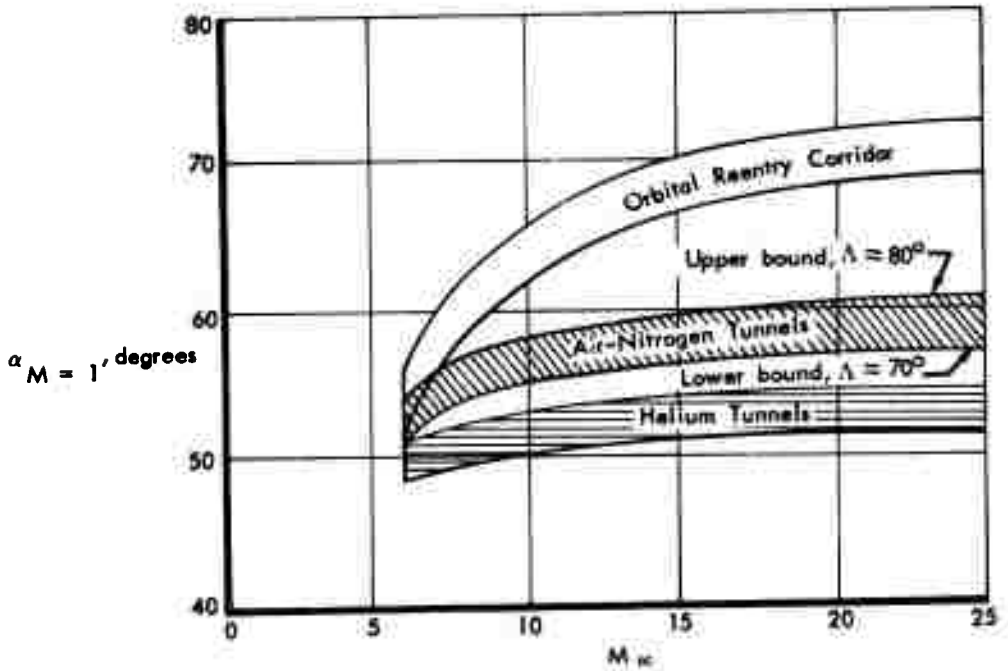


Figure 15: SHARP DELTA WING CENTERLINE SONIC FLOW CONDITIONS

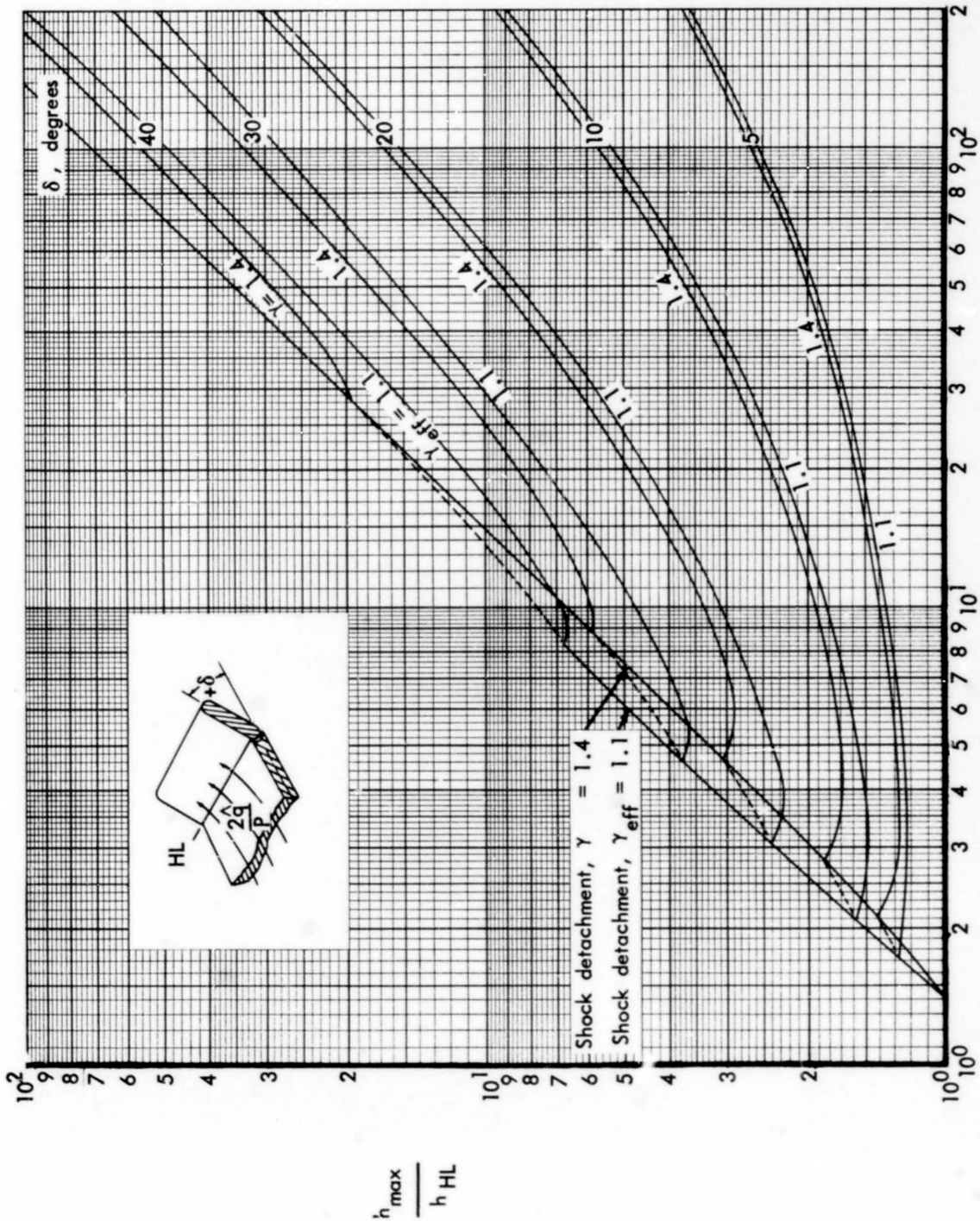


Figure 16: MAXIMUM HEATING RATE INCREASES FOR POSITIVELY DEFLECTED CONTROL SURFACES IN AIR AND NITROGEN FLOWS  $(2 \dot{q}/P)_{HL}$

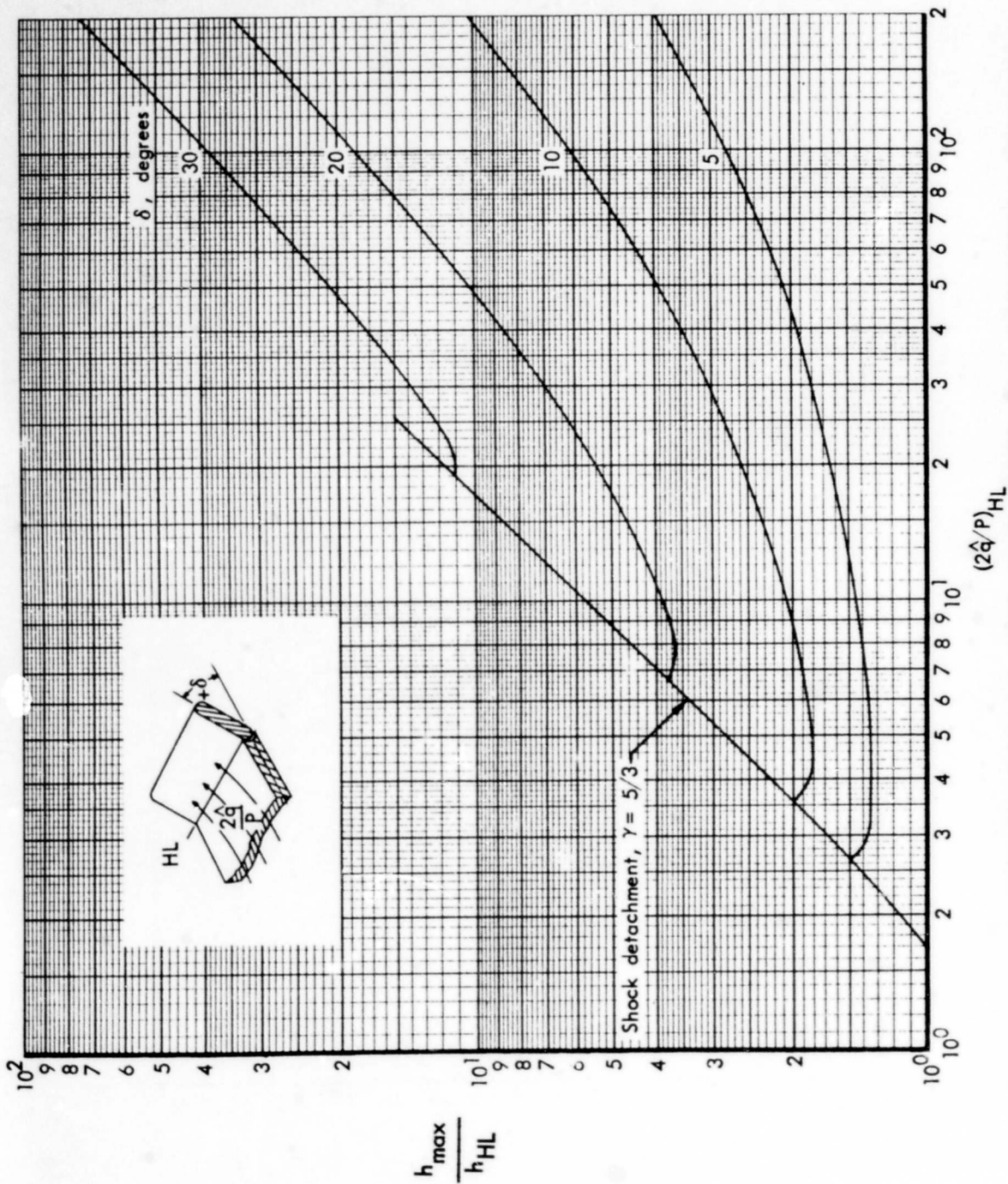
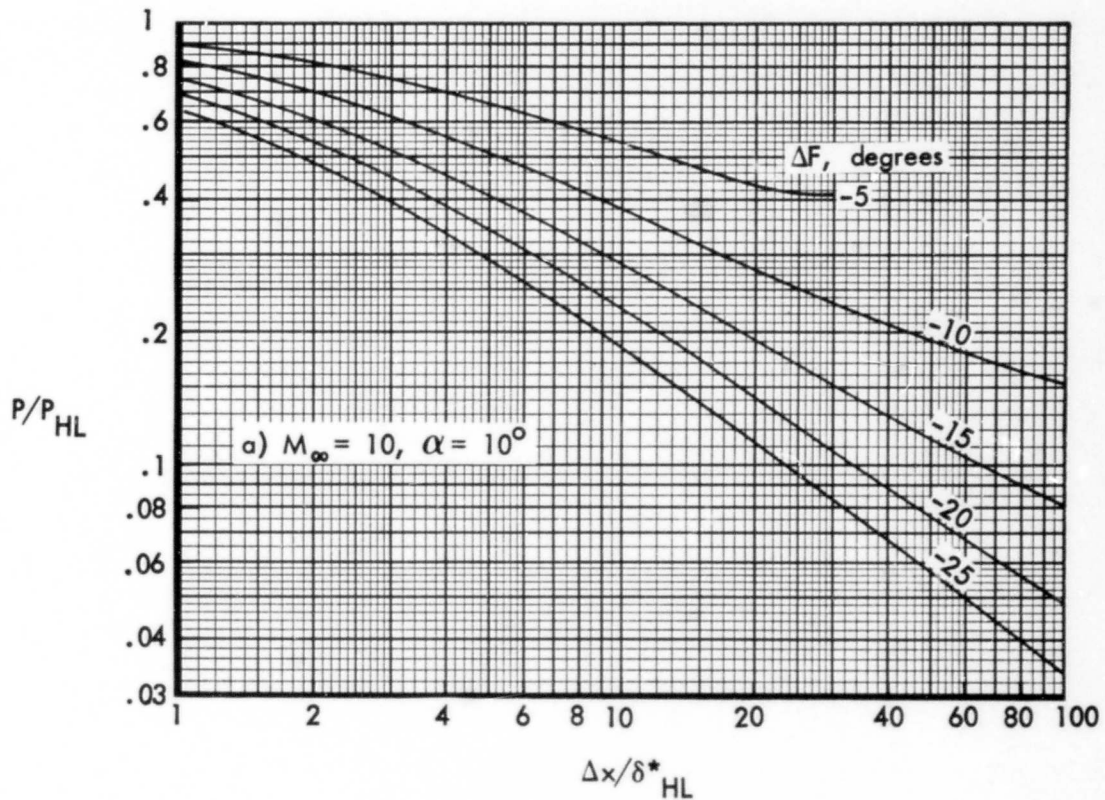


Figure 17: MAXIMUM HEATING RATE INCREASES FOR POSITIVELY DEFLECTED CONTROL SURFACES IN HELIUM GROUND FACILITIES



$T_\infty = 100 \text{ and } 400 \text{ }^\circ\text{R}$

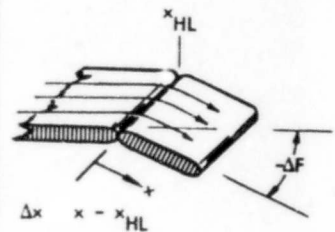
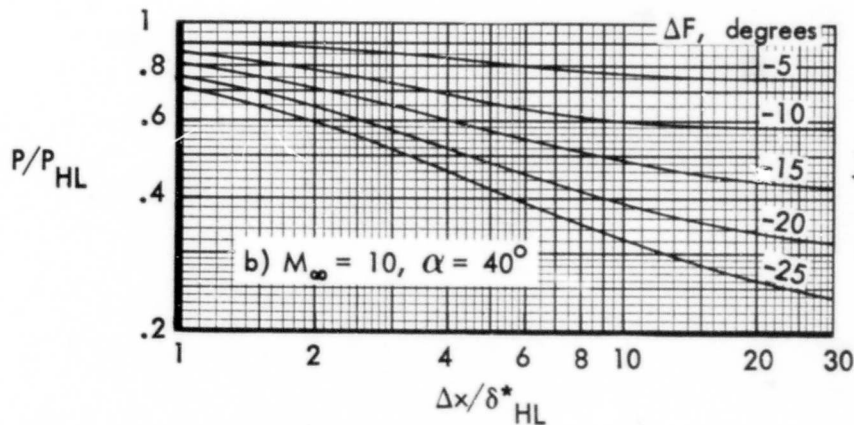
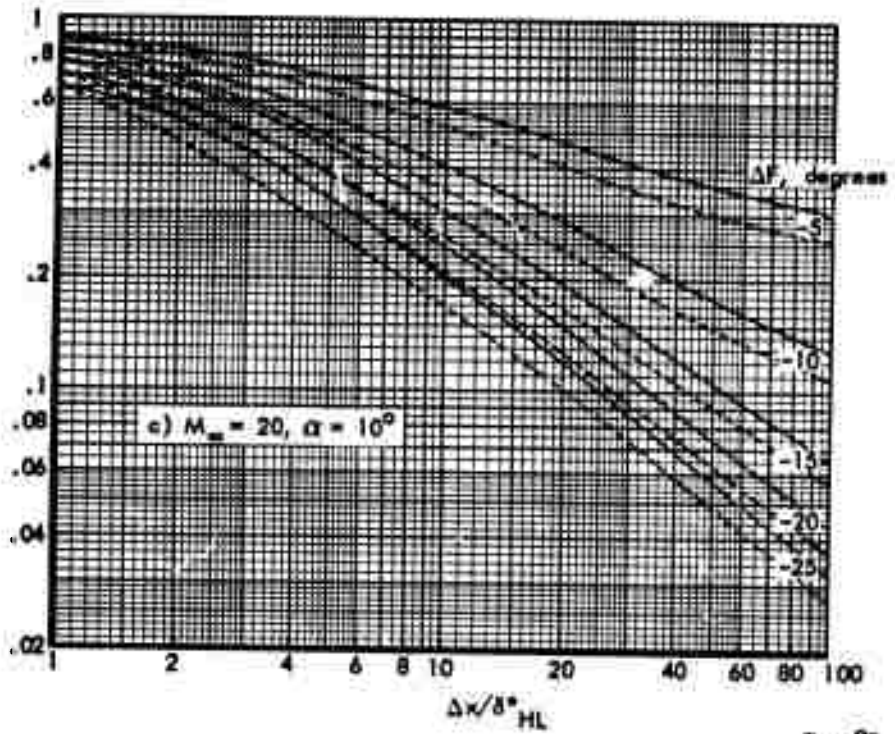


Figure 18: PRESSURE DISTRIBUTION ON NEGATIVELY DEFLECTED CONTROL SURFACES IN AIR AND NITROGEN FLOWS

$P/P_{HL}$



$P/P_{HL}$

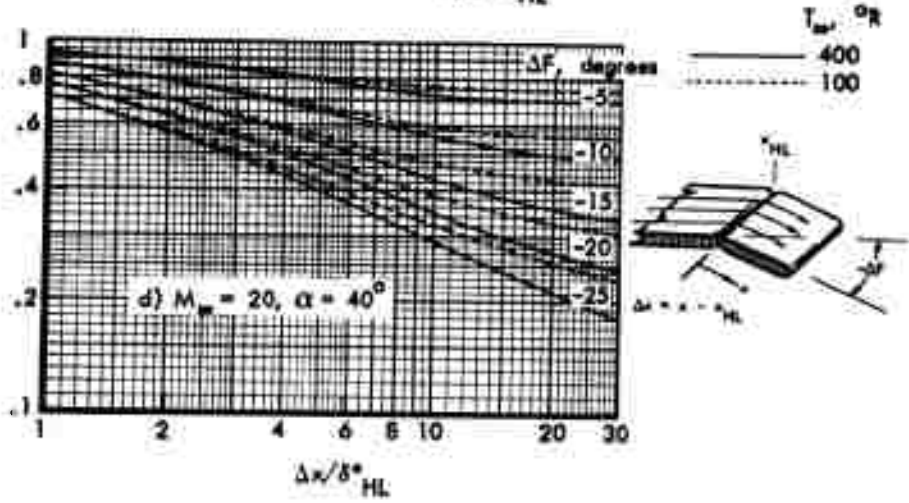


Figure 18: Concluded

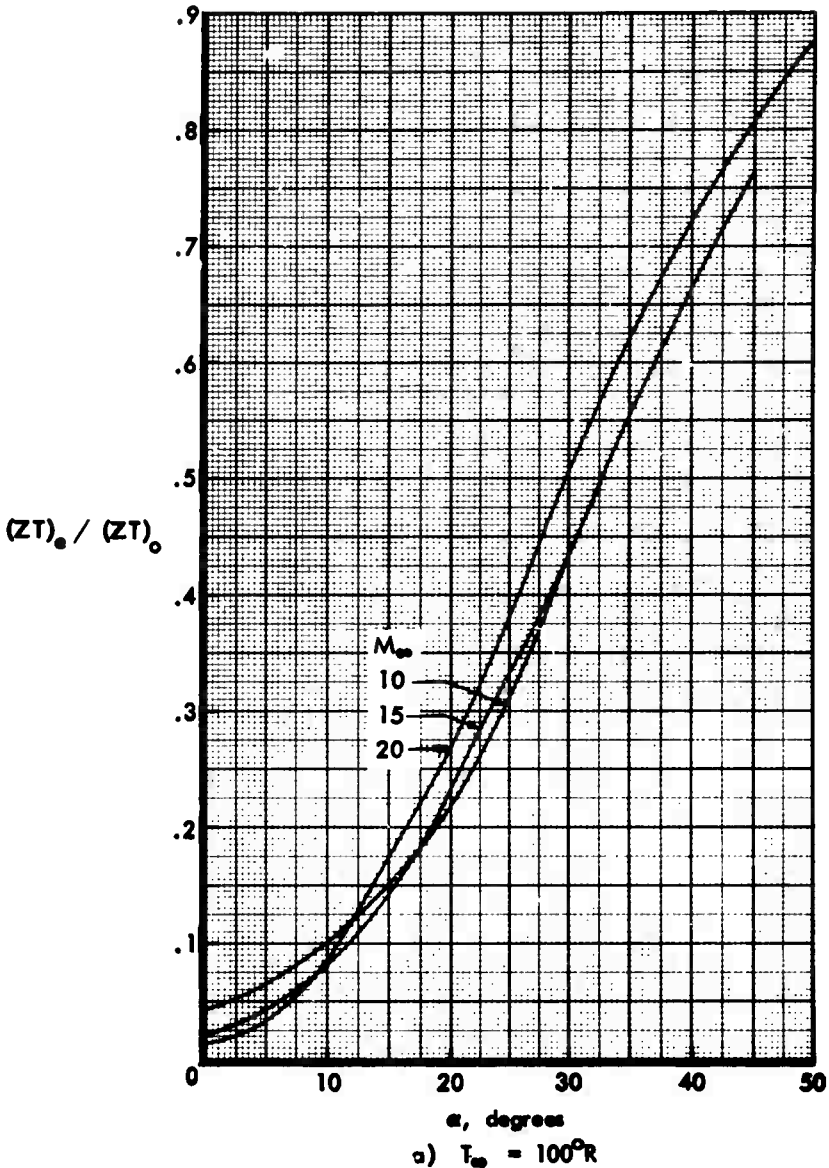


Figure 19: COMPRESSIBILITY FACTOR - TEMPERATURE PRODUCT FOR SHARP FLAT PLATES AT ANGLE OF ATTACK

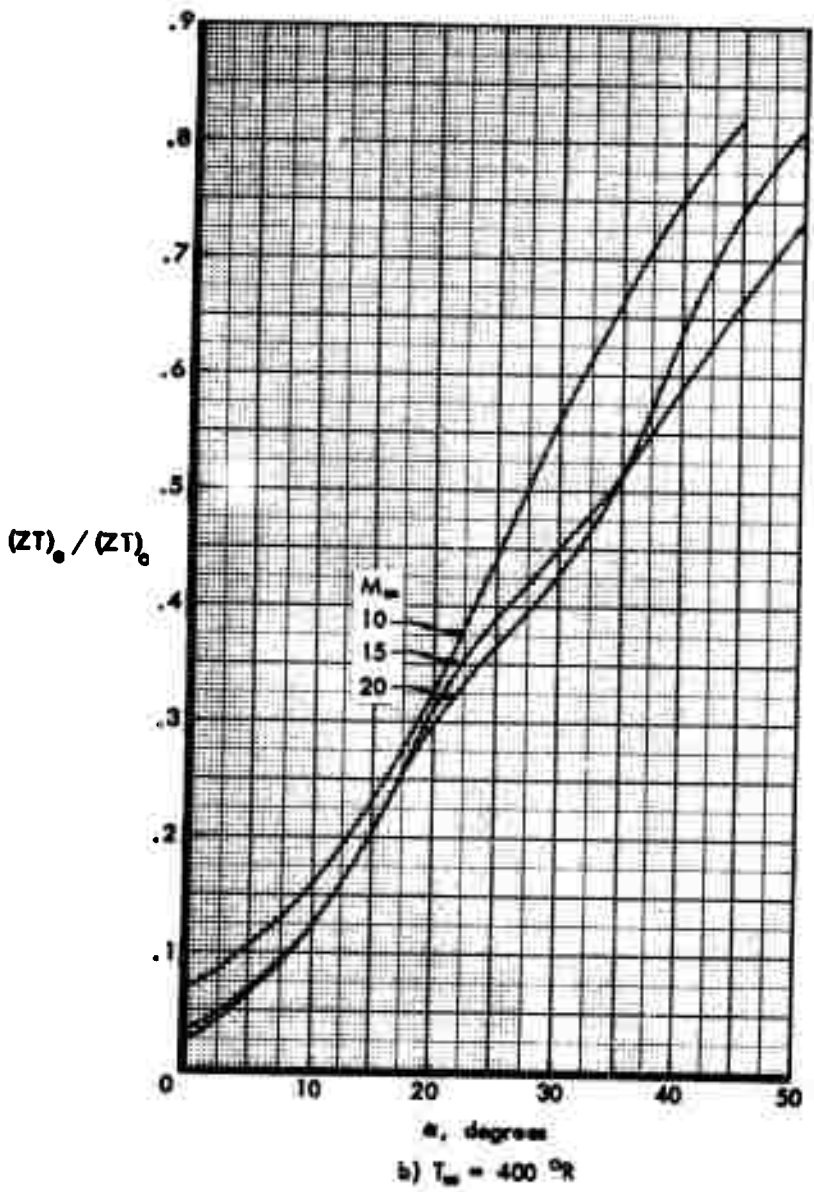


Figure 19: Concluded

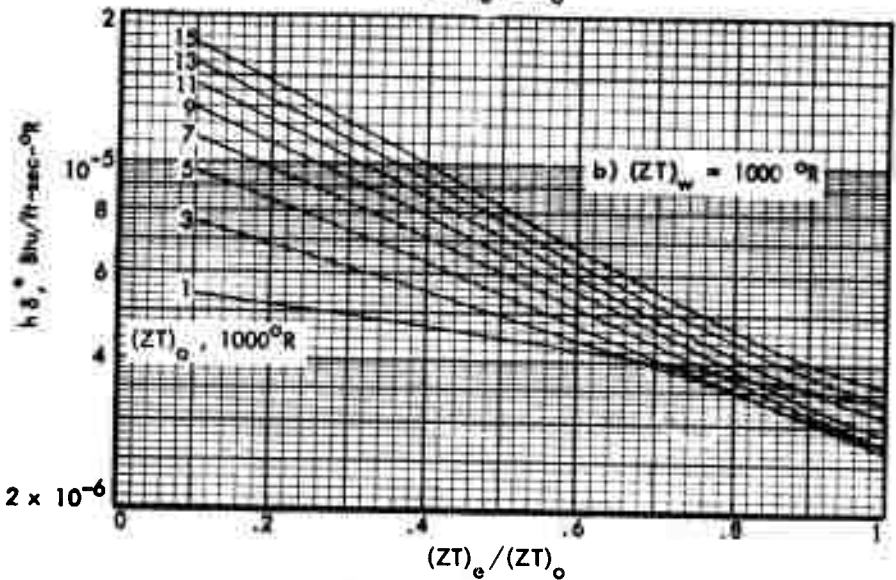
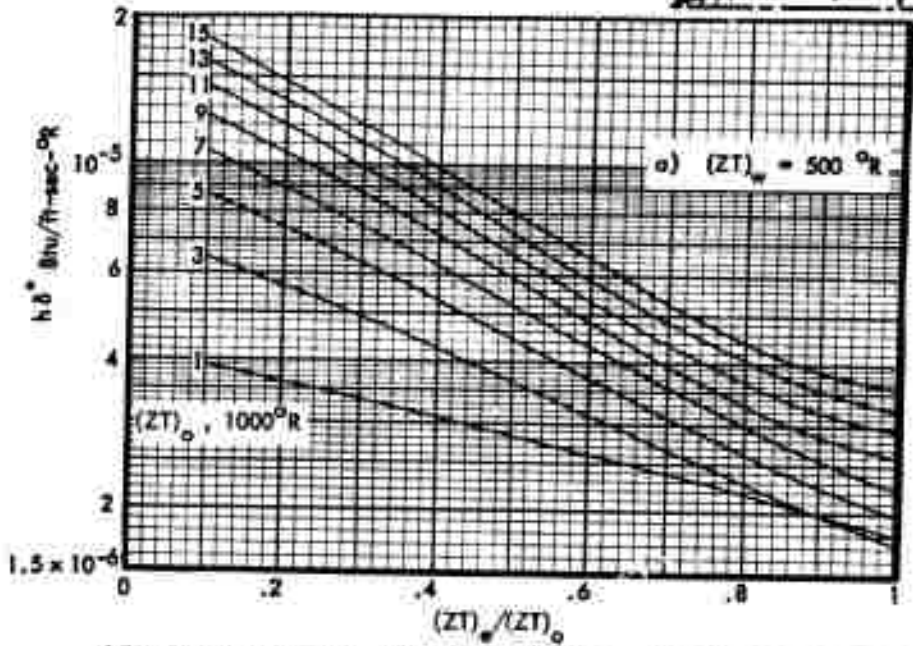


Figure 20: DISPLACEMENT-THICKNESS HEATING PARAMETERS FOR SHARP FLAT PLATES

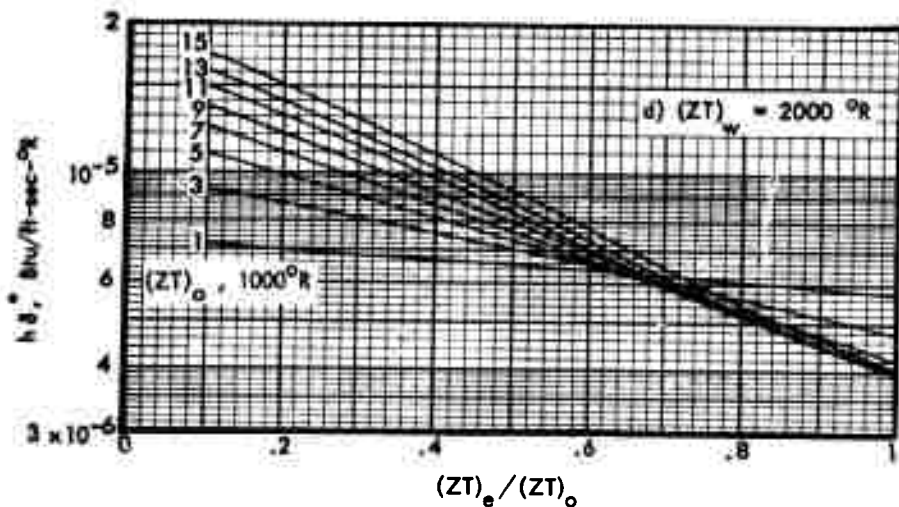
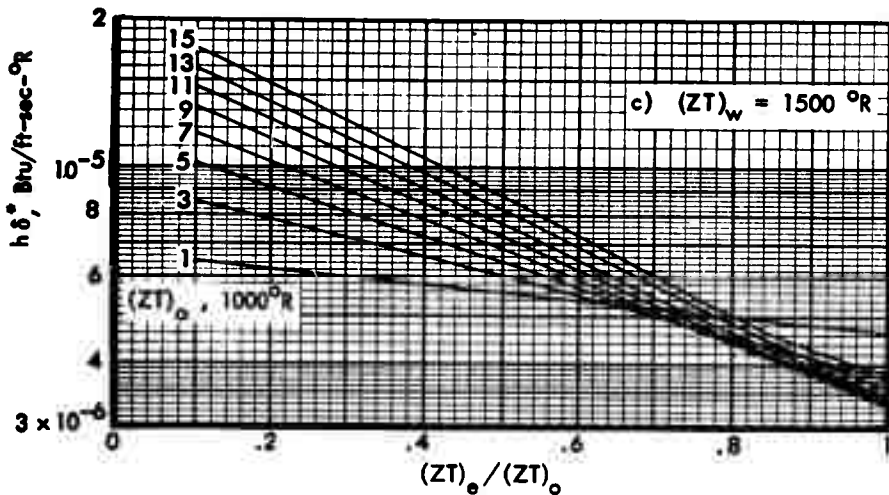


Figure 20: Continued

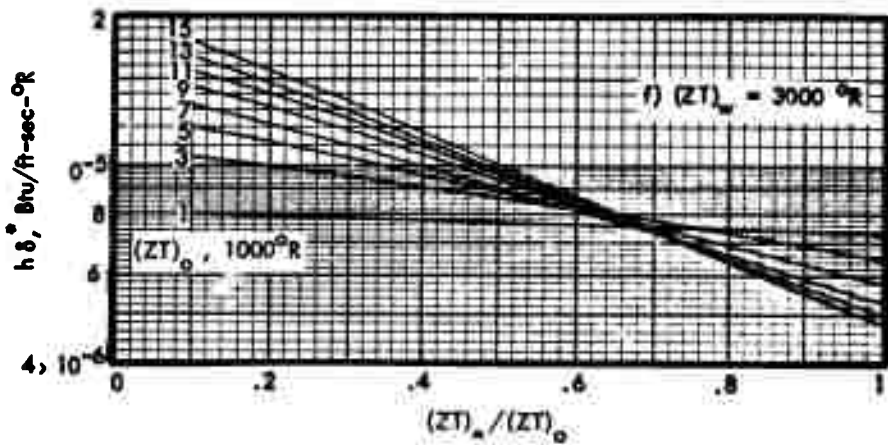
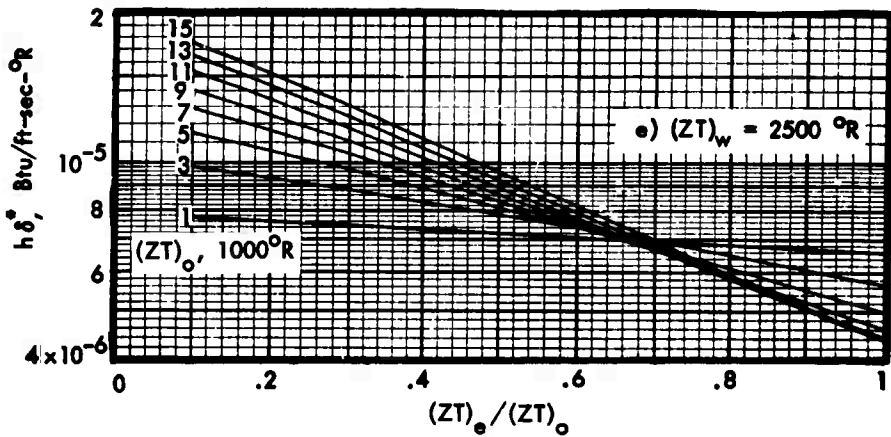


Figure 20: Concluded

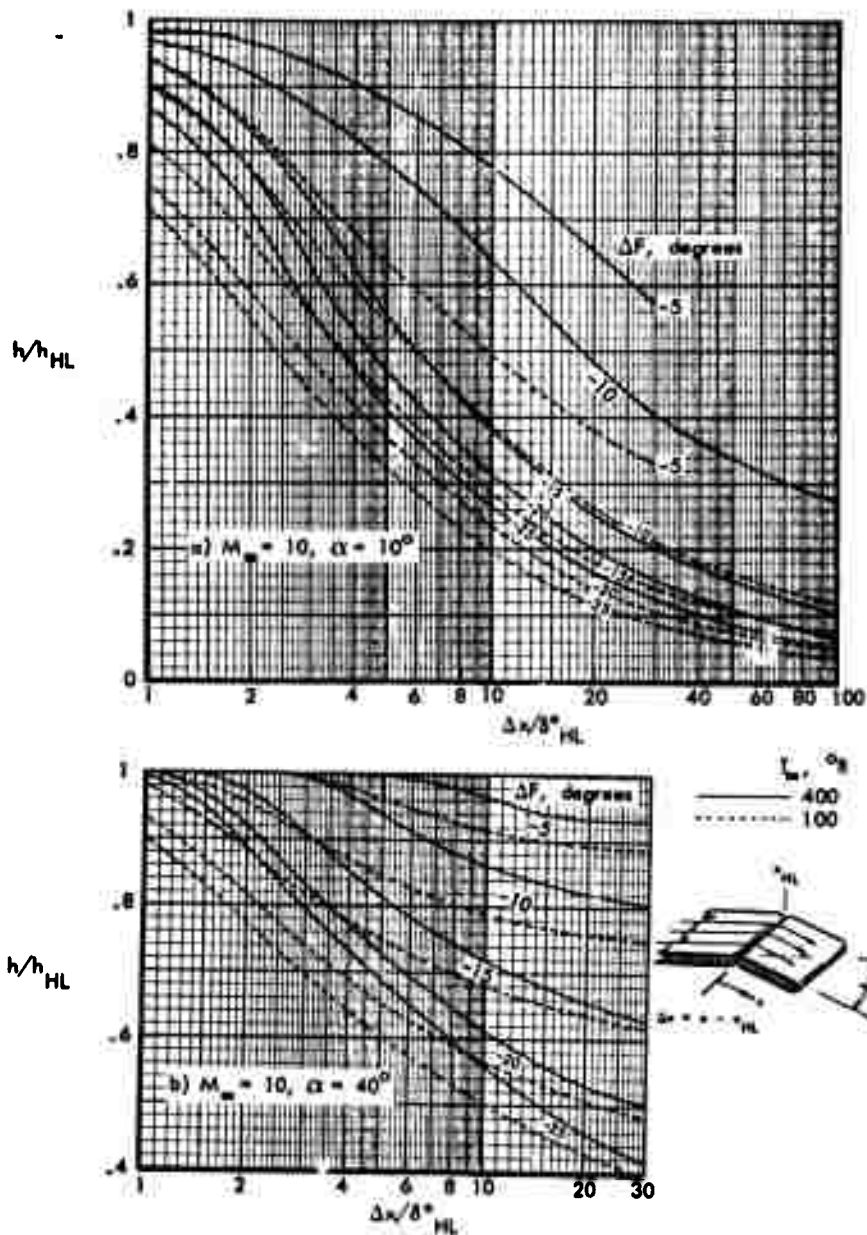


Figure 21: HEATING DISTRIBUTION ON NEGATIVELY DEFLECTED CONTROL SURFACES IN AIR AND NITROGEN FLOWS

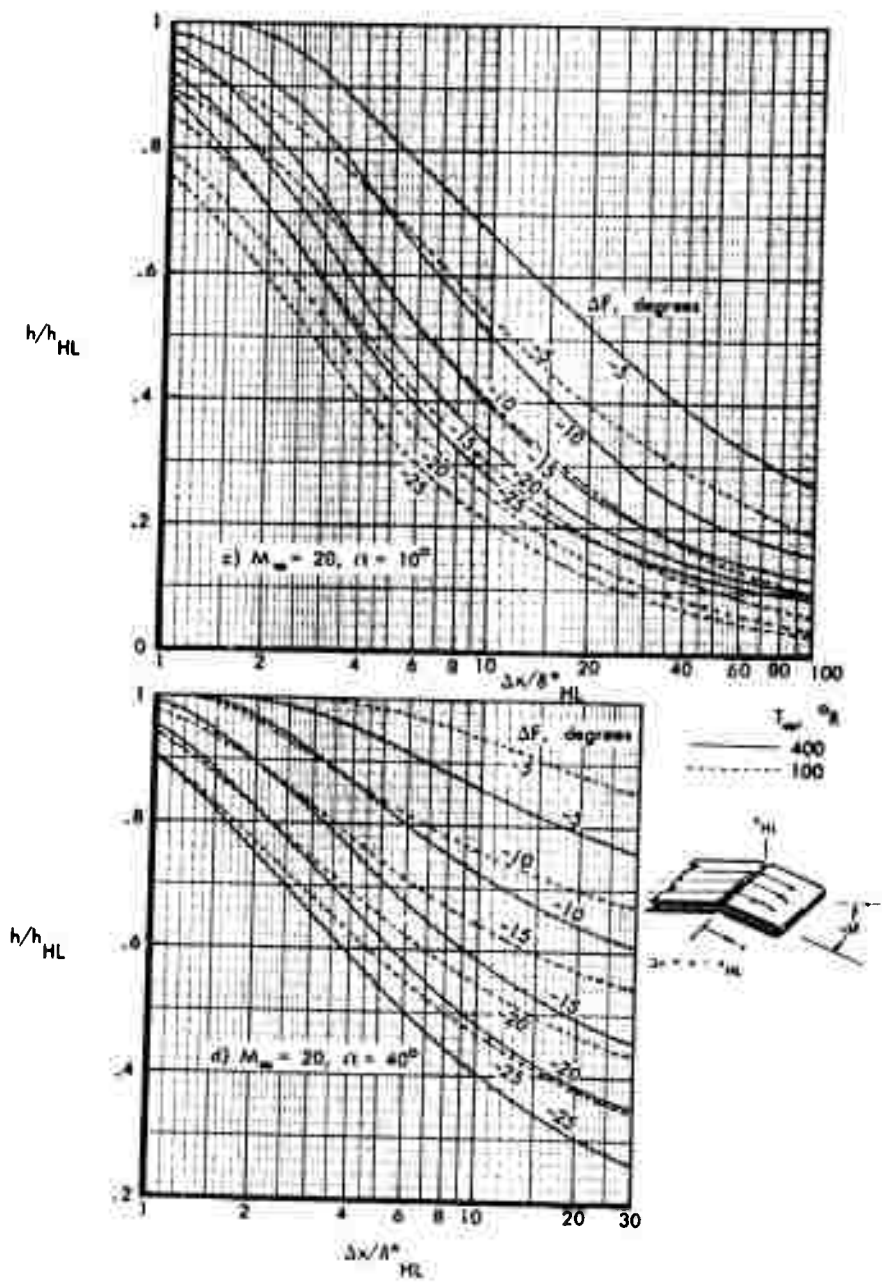
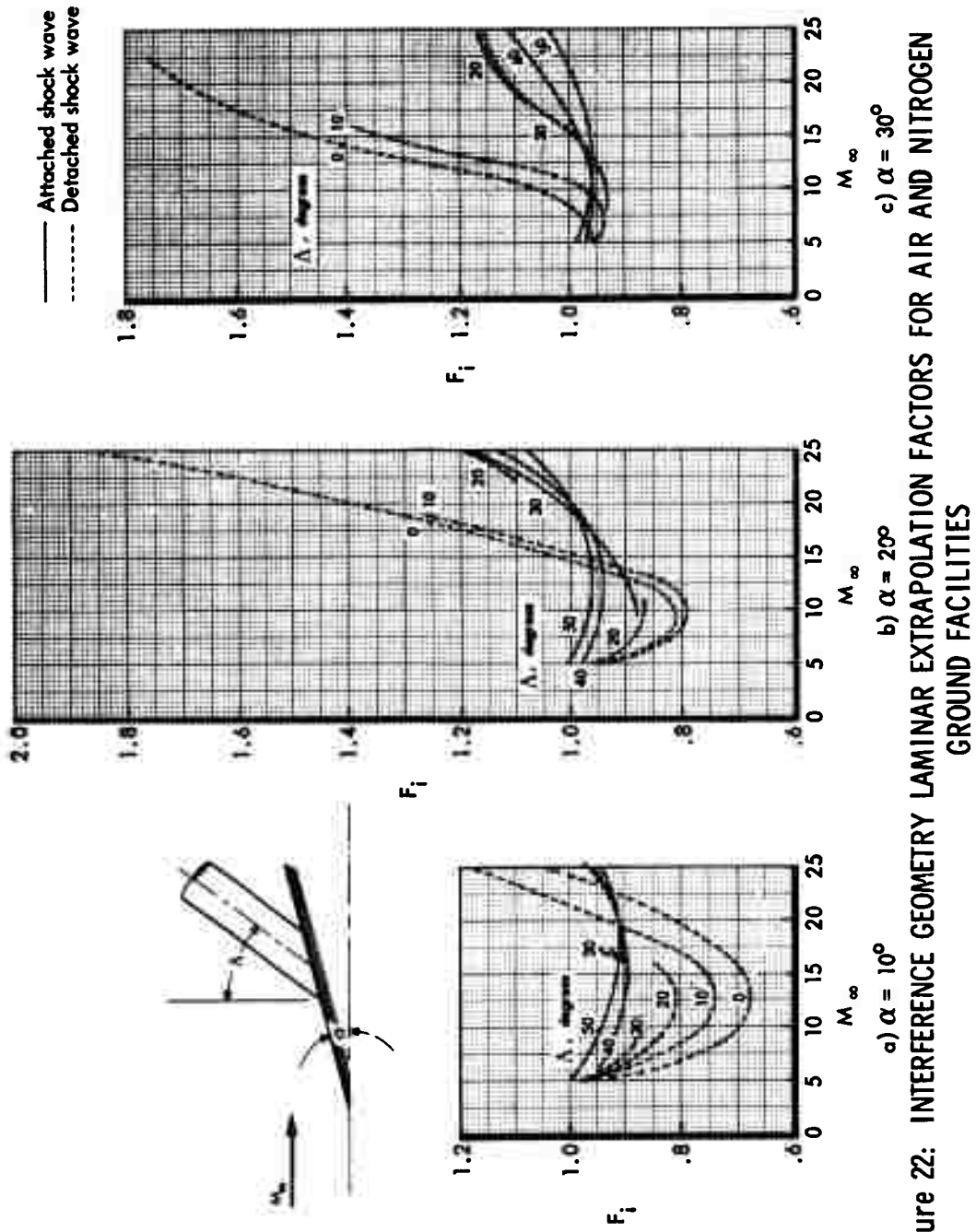
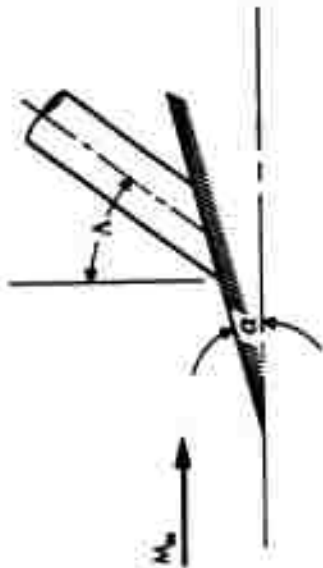


Figure 21: CONCLUDED





— Attached shock wave  
 - - - Detached shock wave

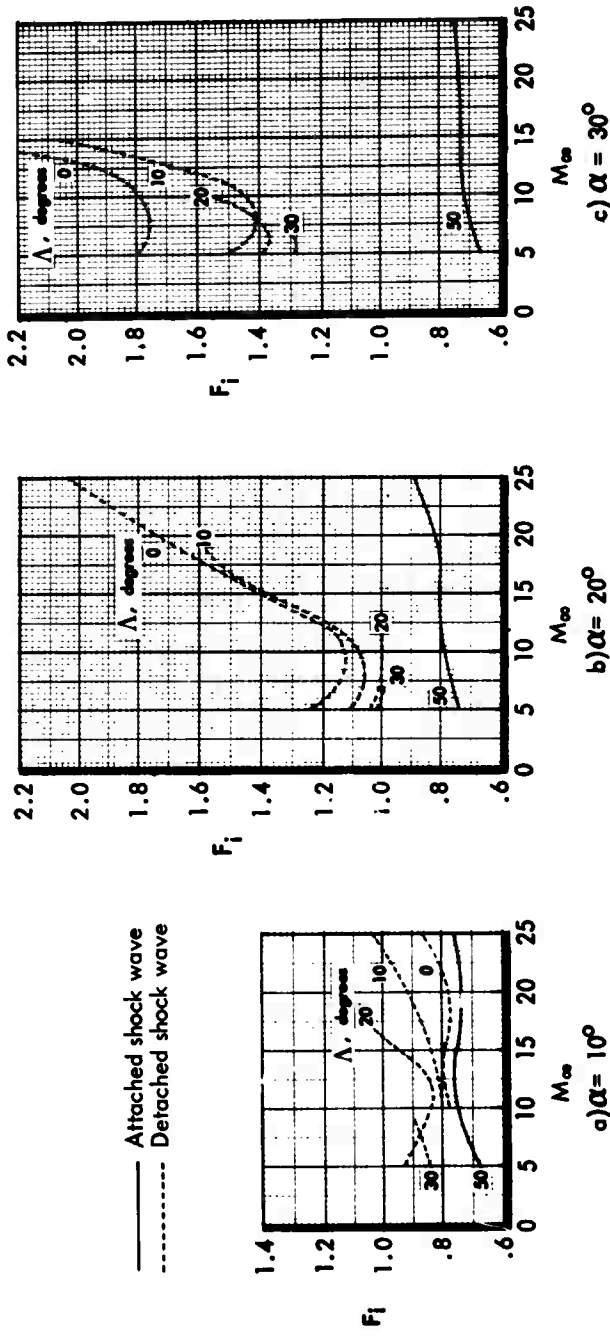
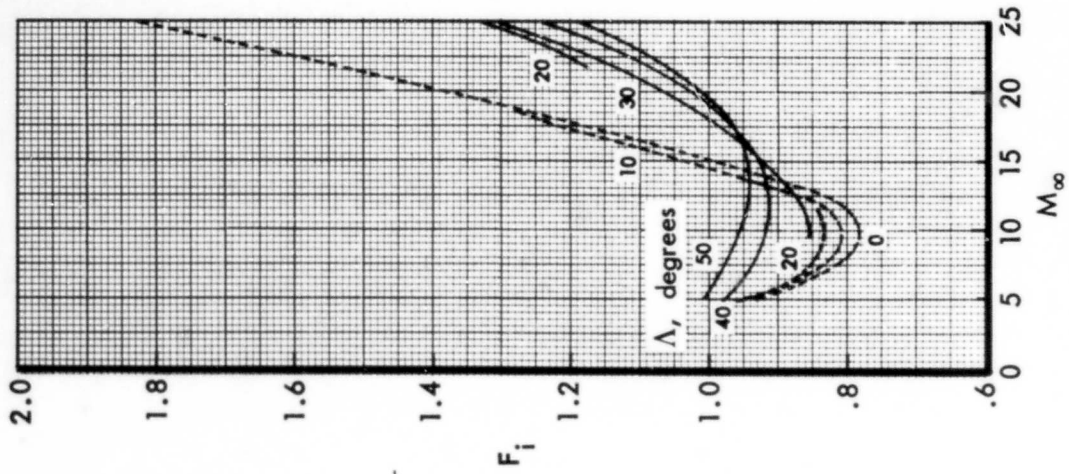
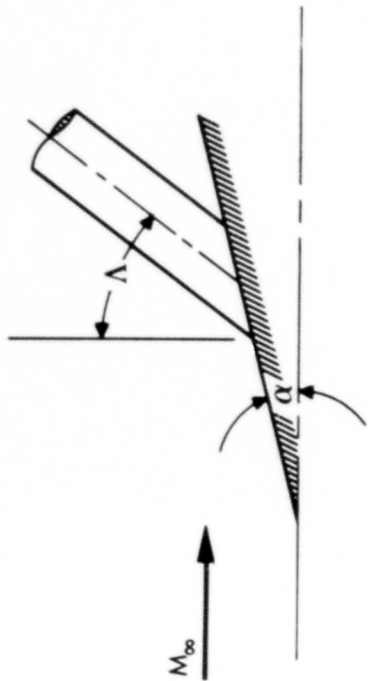
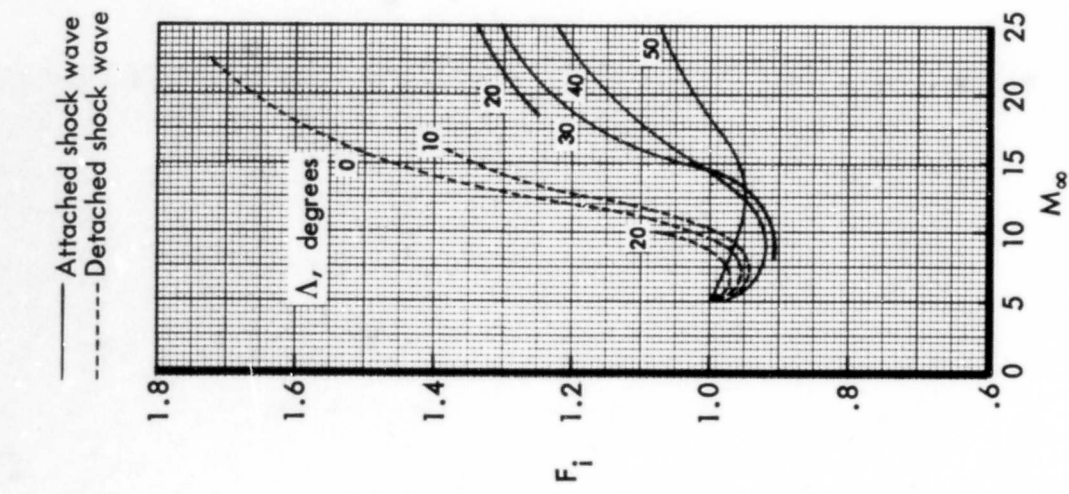


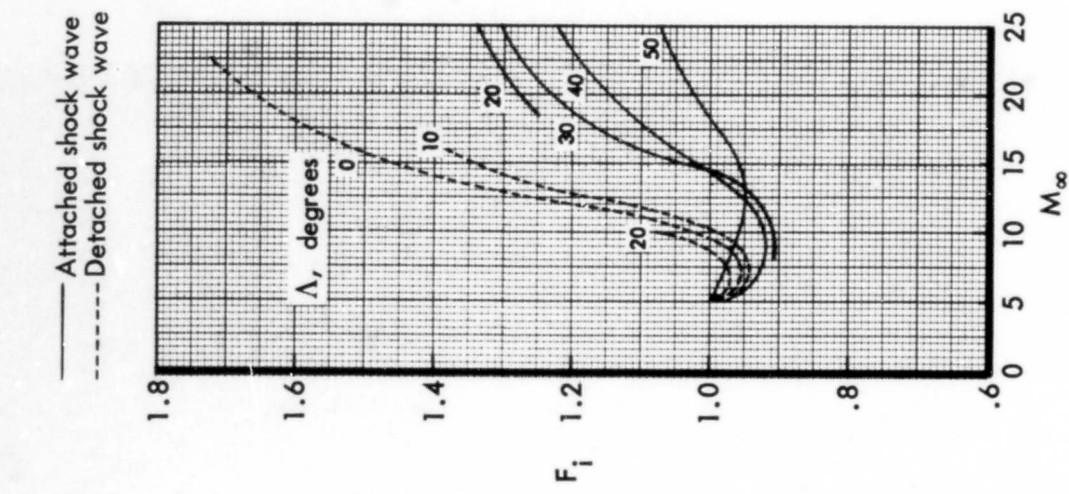
Figure 23: INTERFERENCE GEOMETRY LAMINAR EXTRAPOLATION FACTORS FOR HELIUM GROUND FACILITIES



a)  $\alpha = 10^\circ$



b)  $\alpha = 20^\circ$



c)  $\alpha = 30^\circ$

Figure 24: INTERFERENCE GEOMETRY TURBULENT EXTRAPOLATION FACTORS FOR AIR AND NITROGEN GROUND FACILITIES

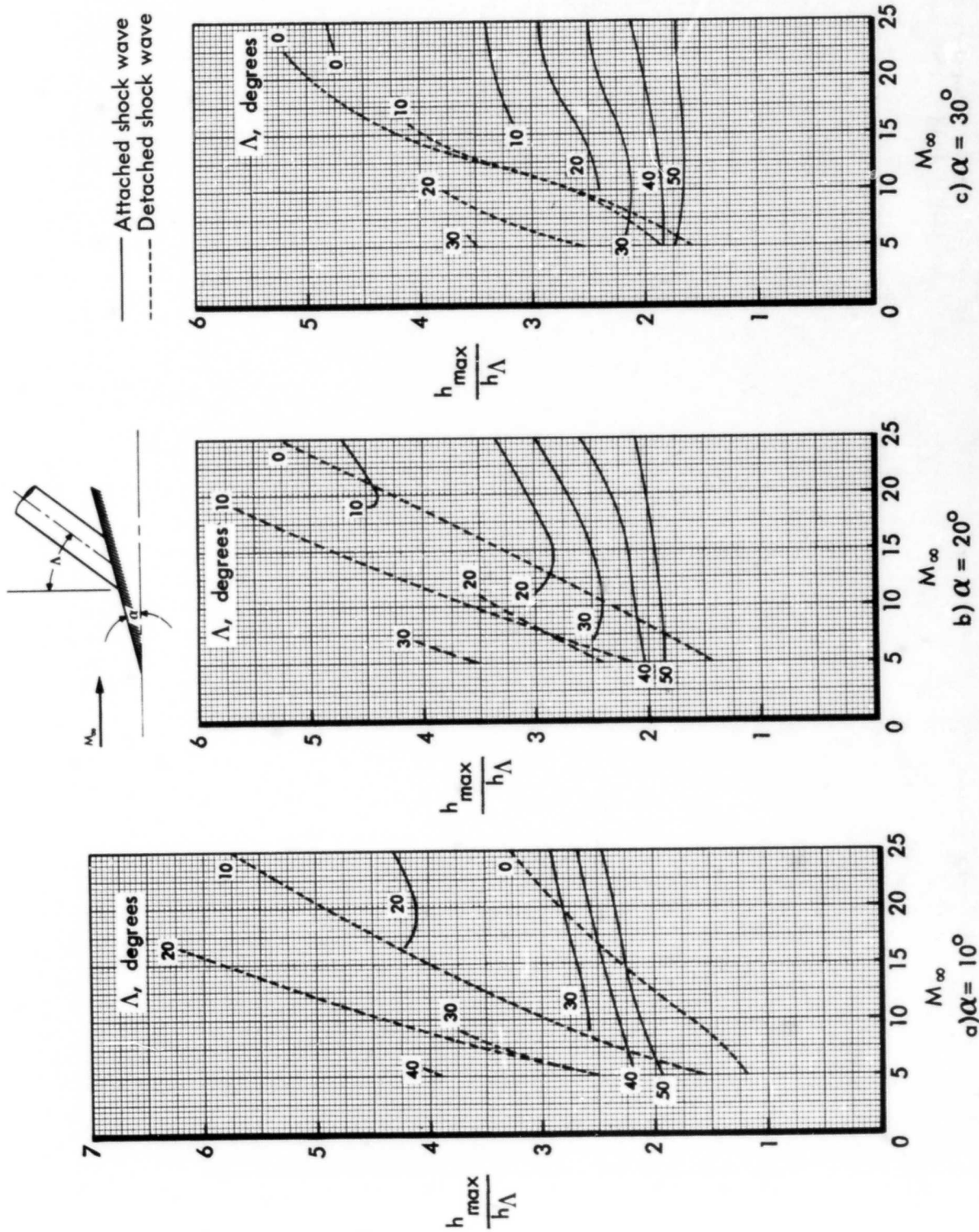
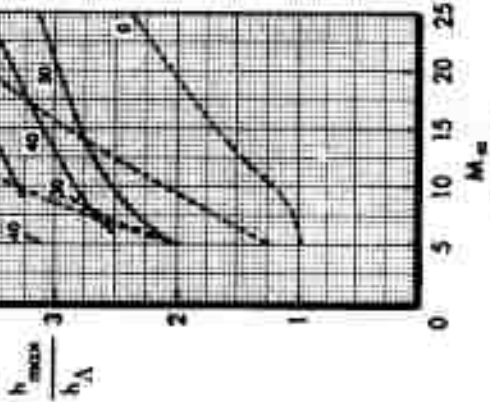
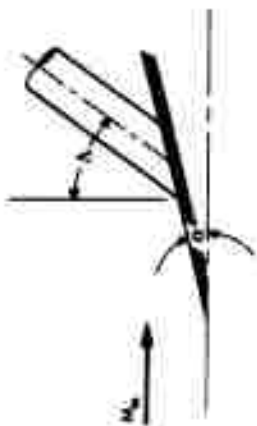
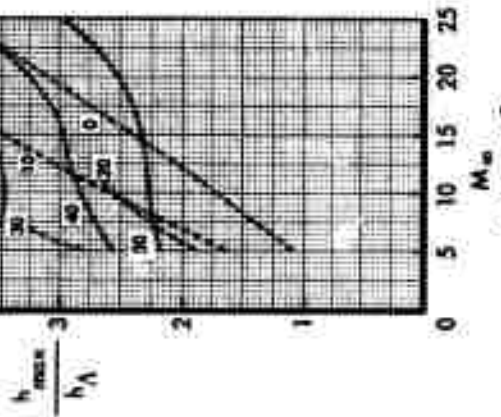


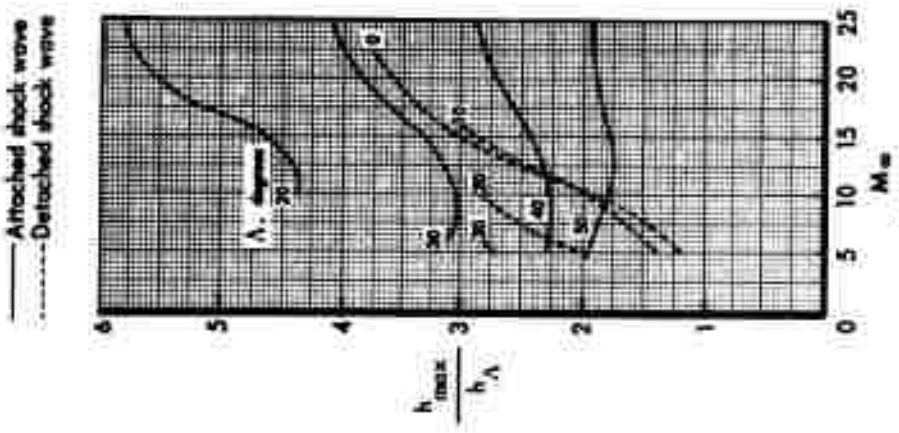
Figure 25: INTERFERENCE GEOMETRY MAXIMUM LAMINAR HEATING RATE RATIOS FOR FLIGHT CONDITIONS



a)  $\alpha = 10^\circ$



b)  $\alpha = 20^\circ$



c)  $\alpha = 30^\circ$

Figure 26: INTERFERENCE GEOMETRY MAXIMUM TURBULENT HEATING RATE RATIOS FOR FLIGHT CONDITIONS

- Orbital reentry
- - - - - Air and nitrogen ground facilities,  
( $i_o$ )<sub>WT</sub> / ( $i_o$ )<sub>FLT</sub>  $\approx$  0.25
- · - · - Helium

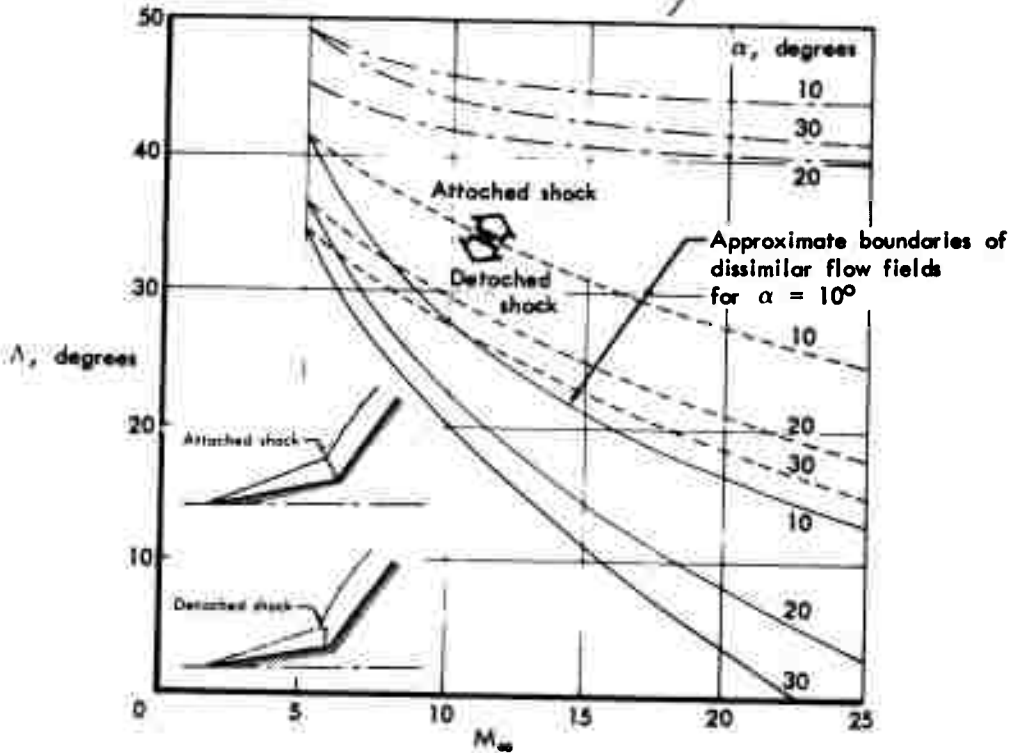
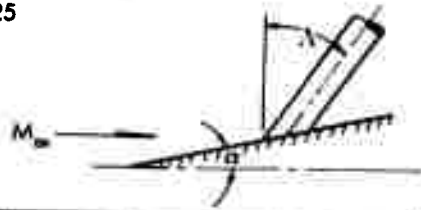


Figure 27: BOUNDARIES BETWEEN REGIONS OF ATTACHED AND DETACHED SHOCK WAVES FOR INTERFERENCE GEOMETRIES



$\delta_{eff}$   
 ——— 1.4  
 - - - 1.15

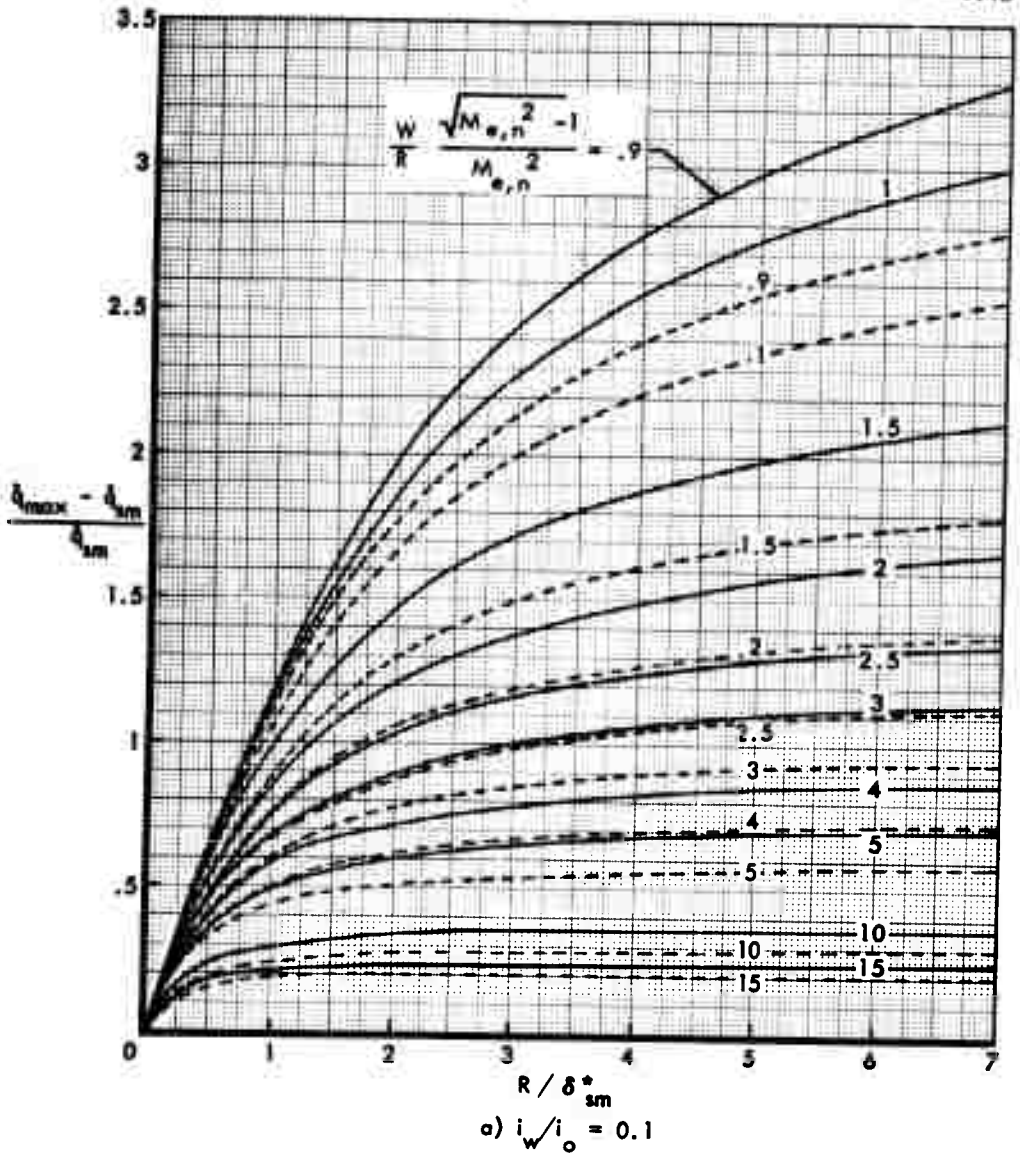


Figure 28: SHALLOW SURFACE WAVE LAMINAR HEATING

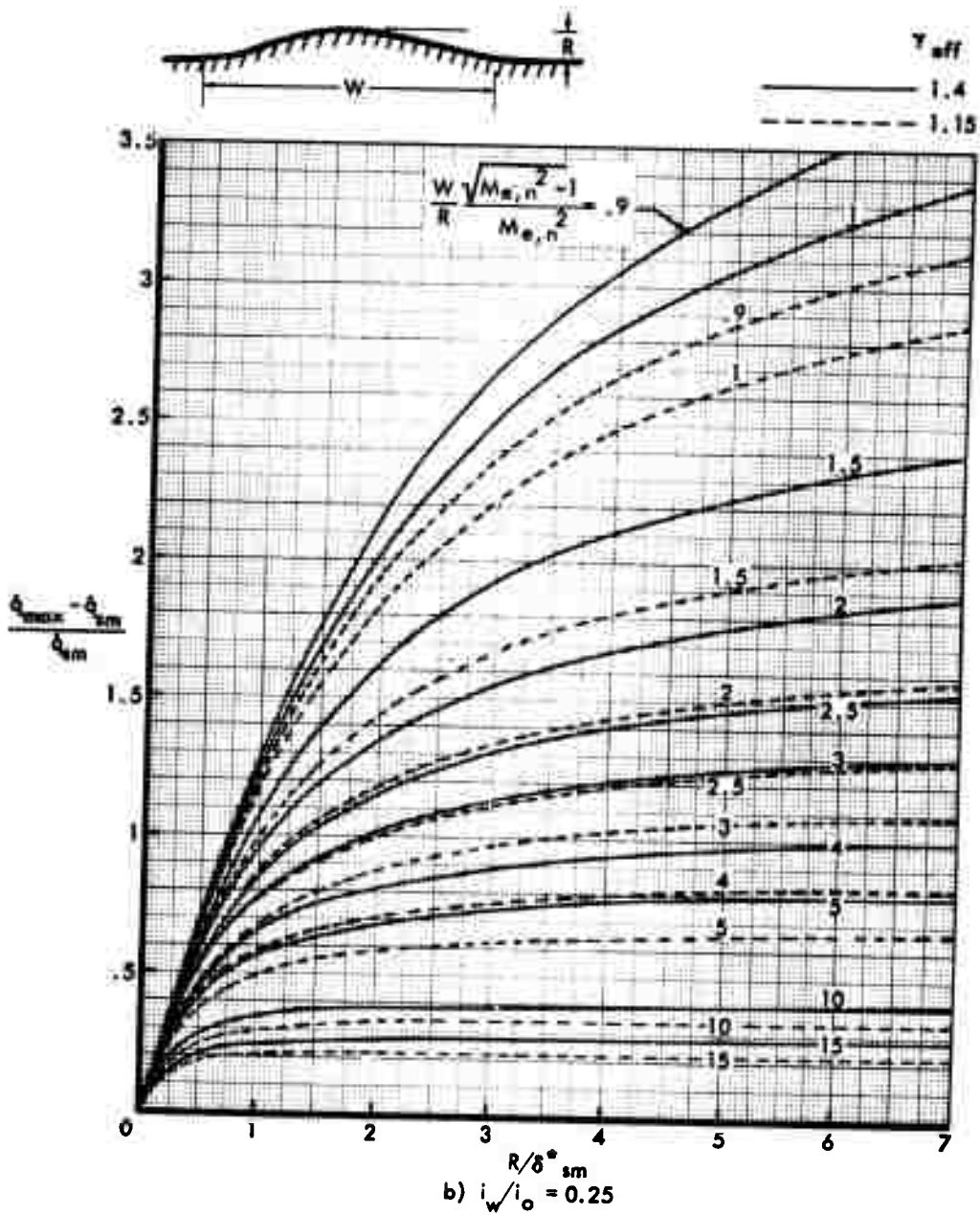
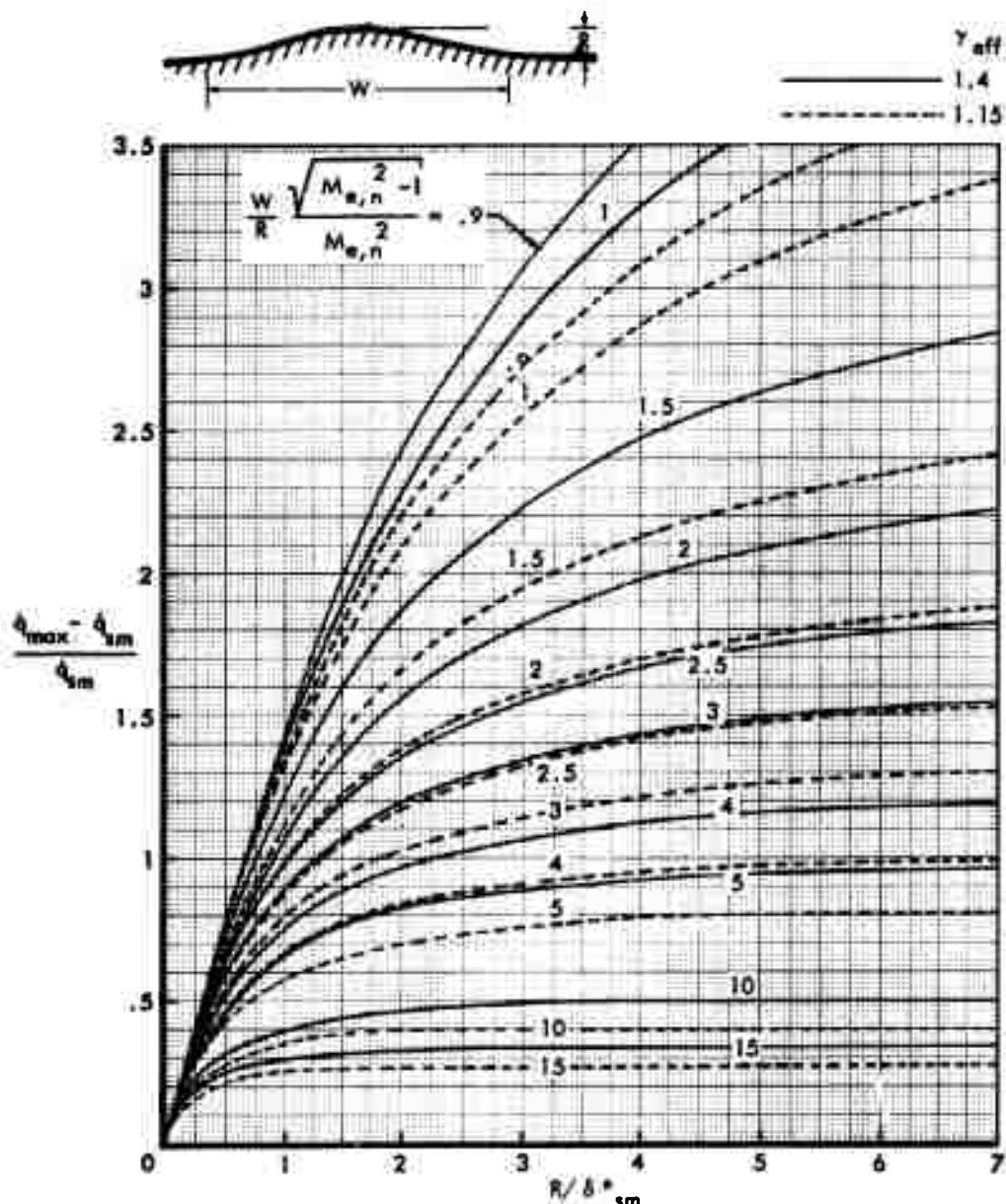
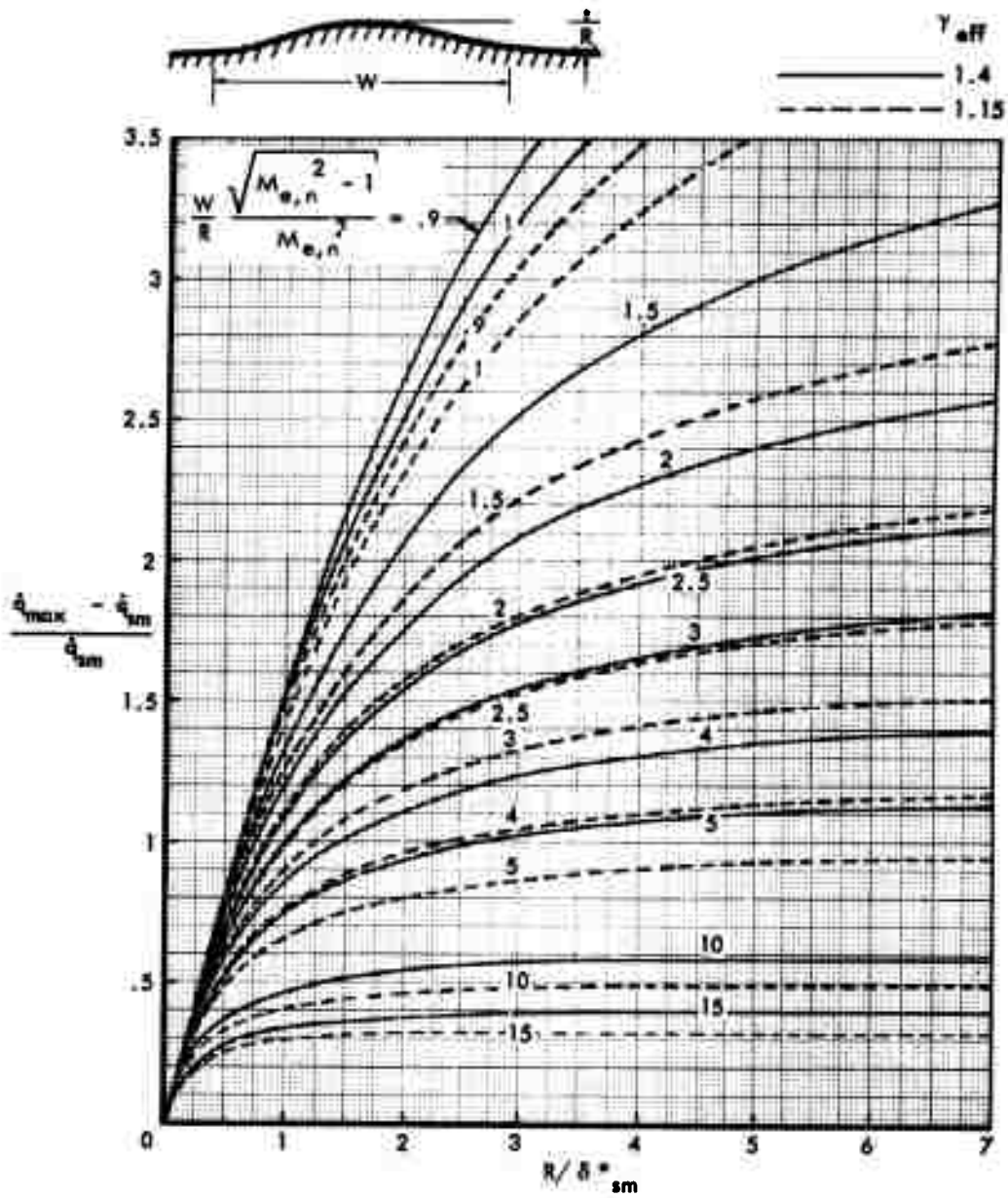


Figure 28: Continued



c)  $i_w/i_o = 0.5$

Figure 28: Continued



d)  $i_w/i_o = 0.75$

Figure 28: Concluded

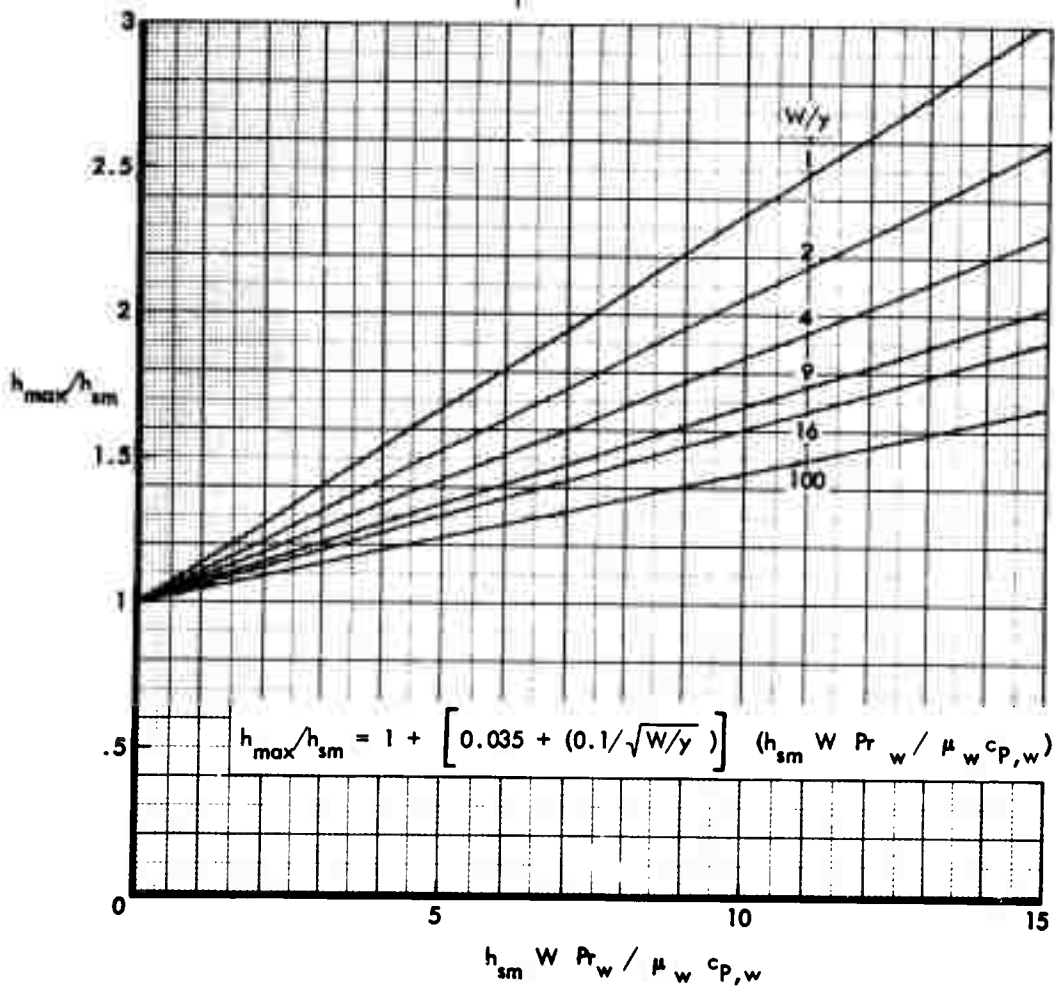
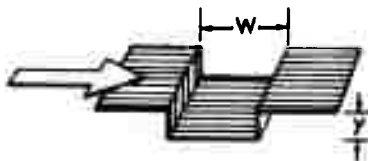


Figure 29: MAXIMUM LAMINAR HEATING NEAR RECTANGULAR GROOVES

## APPENDIX A

### HEAT TRANSFER PREDICTION METHOD FOR SHARP UNYAWED DELTA WINGS

The heat transfer analysis for the sharp unyawed delta wing is made using the  $\rho_r \mu_r$  momentum integral method described in references 2 and 18. A solution is obtained using this method by numerically evaluating integral functions along a streamline. This solution is dependent upon the thermodynamic gas properties, the wall temperature, the velocity, and the cross-flow pressure gradient along the streamline. When any one of these quantities varies with the streamline distance, the solution is also dependent upon the upstream history of the boundary layer flow.

Along streamlines with constant flow-field properties and with a finite, but constant, cross-flow pressure gradient, the integral functions are evaluated explicitly, and the entire integral solution is reduced to a point solution. These requirements are satisfied at the centerline of a sharp unyawed delta wing at angle of attack.

In the following discussion, the explicit form of the solution is developed from the integral form for the centerline of a sharp delta wing. The methods for calculating spanwise heating at both low and high angles of attack are described in the last section.

#### 1. METHOD AT THE CENTERLINE

The general expression for evaluation of laminar or turbulent heat transfer to an arbitrary geometry is

$$\frac{\dot{q}}{i_{aw} - i_w} = H = \frac{\mathcal{L} \mu_o Q_L F_x}{\sigma_r^{0.645} x_{eq, L}} f(R_r) \quad (A1)$$

where  $\dot{q}/i_{aw} - i_w$  is the enthalpy heat-transfer coefficient,  $\mathcal{L}$  is a diffusion parameter reflecting the effect of species diffusion on heat transfer in dissociated flow,  $\mu_o$  is the reference stagnation viscosity,  $\sigma_r$  is the reference partial Prandtl number,  $Q_L$  is a laminar streamwise pressure gradient profile parameter,  $F_x$  and  $x_{eq, L}$  are equivalent distance parameters, and  $f(R_r)$  is a Reynolds number function expressed as

$$f(R_r) = 0.332 \sqrt{R_r} \quad (A2a)$$

for laminar flow, and

$$f(R_r) = \frac{0.185 R_r}{\left[ \log_{10} (R_r + 3000) \right]^{2.584}} \quad (\text{A2b})$$

for turbulent flow.  $R_r$  is the local reference Reynolds number defined as

$$R_r = \frac{\rho_r \mu_r u_e x_{\text{eq}, L}}{\mu_o^2 F_x^2} \quad (\text{A3})$$

where  $\rho_r \mu_r$  is the reference density-viscosity product, and  $u_e$  is the boundary layer edge velocity.

In the reduction of the integral solution to a point solution, the parameters defined by equations (A2) and (A3) are not affected. The profile parameter,  $Q_L$ , and distance parameters,  $F_x$  and  $x_{\text{eq}, L}$ , however, are integral expressions which are modified in order that they can be solved explicitly. In the integral solution, the profile and distance parameters are expressed as

$$Q_L = J_L^{3/10} \quad (\text{A4a})$$

$$x_{\text{eq}, L} = J_L^{-4/10} [b_{\text{eq}, L}] \quad (\text{A4b})$$

$$F_x = J_L^{17/20} [b_{\text{eq}, T} / b_{\text{eq}, L}] \quad (\text{A4c})$$

where  $J_L$  is a streamwise pressure gradient parameter of relatively complex form. For the centerline of the sharp delta wing,  $J_L$  assumes the value unity and for that reason its definition is not shown. The expression for  $J_L$  is presented in reference 18. The parameters  $b_{\text{eq}, L}$  and  $b_{\text{eq}, T}$  are expressed as

$$b_{\text{eq}, L} = [x] \int_0^1 \overline{\rho_r \mu_r u_e (rf \bar{E}_L)^2} d\bar{x} \quad (\text{A5a})$$

$$b_{\text{eq}, T} = [x] \int_0^1 \overline{\rho_r \mu_r u_e (rf \bar{E}_T)^{5/4}} d\bar{x} \quad (\text{A5b})$$

where  $r$  and  $f$  are divergence parameters defined later in this Appendix,  $\bar{E}_L$  and  $\bar{E}_T$  are the laminar and turbulent spanwise pressure gradient parameters, respectively, and  $d\bar{x}$  is  $d(x/x_i)$ . The subscript,  $i$ , refers to the local point of interest. The bar above the integrand in the expressions for  $b_{\text{eq}, L}$  and  $b_{\text{eq}, T}$  indicates that the integrand is normalized with respect to the value at  $x = x_i$ .

At the centerline of a sharp delta wing the streamwise pressure gradient is zero, and the thermodynamic gas properties are constant. Hence,

$$J_L \equiv 1 \quad (A6)$$

and

$$(b_{eq, L/x})_i = \int_0^1 \left( \overline{rf} \overline{E}_L \right)_i^2 d\bar{x} \quad (A7a)$$

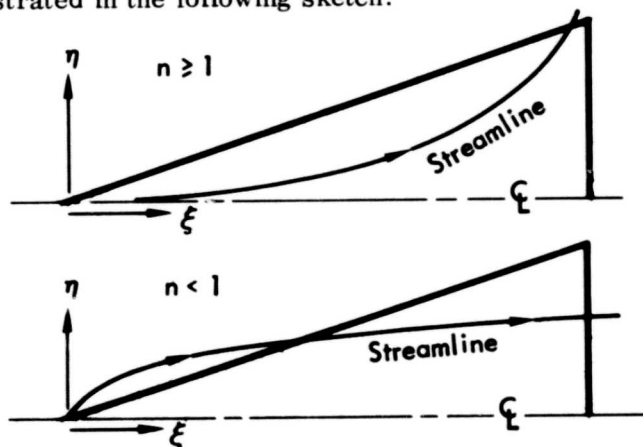
$$(b_{eq, T/x})_i = \int_0^1 \left( \overline{rf} \overline{E}_T \right)_i^{5/4} d\bar{x} \quad (A7b)$$

It remains to express the divergence parameters  $\bar{r}$  and  $\bar{f}$  in the integrands in terms of the variable  $\bar{x}$  and to evaluate these integrals.

Evaluation of  $\bar{r}$  and  $\bar{f}$  is made by assuming different functions of  $x$  that depend on the shape of the streamline patterns. In the vicinity of the centerline, the streamlines take the form

$$\eta \sim \xi^n$$

The exponent,  $n$ , is a crossflow pressure gradient divergence parameter evaluated at the centerline. It is defined in Appendix B. Possible streamline patterns are illustrated in the following sketch:



When  $n > 1$ , the delta wing streamline pattern is identical to the streamline pattern for a sharp yawed cone and the parameters  $\bar{f}$  and  $\bar{r}$  become

$$\left. \begin{aligned} \bar{f} &= \bar{x}^{n-1} \\ \bar{r} &= \bar{x} \end{aligned} \right\} n > 1 \quad (A8)$$

For values of  $n < 1$ , all delta-wing streamlines, except those coinciding with the centerline, originate at the leading edge of the wing rather than at the apex. These streamlines, therefore, pass through regions of varying pressure, and strictly speaking, cannot be treated using methods which assume that a zero streamwise pressure gradient exists. Sufficiently far downstream and near the

centerline, however, this effect can be neglected. All necessary flow-field requirements are satisfied by assigning the following relationships to  $\bar{r}$  and  $\bar{f}$ .

$$\left. \begin{aligned} \bar{f} &= \bar{x}^{n(n-1)} \\ \bar{r} &= \bar{x}^{n(2-n)} \end{aligned} \right\} n < 1 \quad (A9)$$

With the relationships shown in (A8) and (A9), equation (A7) reduces to

$$n \geq 1 \quad \left\{ \begin{aligned} (b_{\text{eq}, L/x}) &= (x_{\text{eq}, L/x}) = \left\{ 1 + 2 \left[ 1 + (n-1) \bar{E}_L \right] \right\}^{-1} & (A10a) \\ (b_{\text{eq}, T/x}) &= (x_{\text{eq}, T/x}) = \left\{ 1 + \frac{5}{4} \left[ 1 + (n-1) \bar{E}_T \right] \right\}^{-1} & (A10b) \end{aligned} \right.$$

$$n < 1 \quad \left\{ \begin{aligned} (b_{\text{eq}, L/x}) &= (x_{\text{eq}, L/x}) = \left\{ 1 + 2n \left[ 2 - n + (n-1) \bar{E}_L \right] \right\}^{-1} & (A10c) \\ (b_{\text{eq}, T/x}) &= (x_{\text{eq}, T/x}) = \left\{ 1 + \frac{5}{4} n \left[ 2 - n + (n-1) \bar{E}_T \right] \right\}^{-1} & (A10d) \end{aligned} \right.$$

$\bar{E}_L$  and  $\bar{E}_T$  are functions of thermodynamic variables only and can be evaluated at any point of interest by the relationships shown below.

$$\bar{E}_L = 1 + F_c \Gamma_c \quad (A11a)$$

$$\bar{E}_T = (1 + 0.7652 F_{k_o} \Gamma_o) \left[ \frac{1 + F_c \Gamma_c}{1 + F_{k_o} \Gamma_o} \right]^4 \quad (A11b)$$

where

$$\Gamma_c = 0.71764 \left[ \left( 1 + \frac{F_c}{0.4018} \right)^{1/2} - 1 \right] \quad (A12a)$$

$$\Gamma_o = 0.71764 \left[ \left( 1 + \frac{F_o}{0.4018} \right)^{1/2} - 1 \right] \quad (A12b)$$

$$F_c = (\Sigma_c - 0.294) \sigma_r^{0.355} \quad (A13a)$$

$$F_o = (\Sigma_o - 0.294) \sigma_r^{0.355} \quad (A13b)$$

$$\Sigma_c = \frac{(ZT)_{M,c}}{(ZT)_e} = \frac{(ZT)_{iM,o}}{(ZT)_{ie}} \quad (A14a)$$

$$\Sigma_o = \frac{(ZT)_{M,o}}{(ZT)_e} = \frac{(ZT)_{iM,o}}{(ZT)_{ie}} \quad (A14b)$$

$$i_{m,c} = 0.5(i_w + i_e) + 0.206(i_o - i_e) \sigma_r \sqrt{\frac{\rho_s \mu_s}{\rho_w \mu_w}} \quad (A15a)$$

$$i_{m,o} = 0.5(i_w + i_e) \quad (A15b)$$

For  $n \geq 1$ ,

$$F_k = (2\Sigma_c)^{0.194e^{-k}} \quad (A16a)$$

$$F_{k_o} = (2\Sigma_o)^{0.194e^{-k}} \quad (A16b)$$

$$k = \frac{2}{3} (n - 1) \quad (A16c)$$

and for  $n < 1$ ,

$$F_k = (2\Sigma_c)^{-0.194e^{-k}} \quad (A17a)$$

$$F_{k_o} = (2\Sigma_o)^{-0.194e^{-k}} \quad (A17b)$$

$$k = \frac{2}{3} n(n - 1) \quad (A17c)$$

Heat-transfer equations for laminar and turbulent flow are expressed in terms of the above parameters. The laminar heat-transfer expression is obtained by combining equations (A1), (A2a), and (A3). With a slight rearrangement this reduces to the form

$$H_L = \frac{0.332 \mathcal{L}}{\sigma_r^{0.645}} \left[ \frac{\rho_r \mu_r u_e}{x} \right]^{0.5} \left( \frac{x_{eq,L}}{x} \right)^{-0.5} \quad (A18)$$

where  $x$  is the centerline distance measured from the apex and  $(x_{eq,L}/x)$  is obtained using equation (A10).

In the absence of cross-flow pressure gradients,  $n=0$  and  $(x_{eq,L}/x) = 1$ . It is seen that the expression for heat transfer at the centerline of a sharp delta wing is composed of an expression without the cross-flow pressure gradient effect which is multiplied by the factor  $(x_{eq,L}/x)^{-0.5}$ . This distance factor is the only factor which incorporates the cross-flow pressure gradient effect and it is evaluated using the streamline divergence parameter,  $n$ .

The turbulent heat-transfer expression is based upon a relationship between the laminar and turbulent forms of the Reynolds number function expressed by equation (A2a) and (A2b). Laminar heat-transfer coefficients obtained using equation (A18) are modified to obtain the turbulent heat-transfer coefficient, by the following expression

$$H_T = H_L \left\{ \frac{0.185\sqrt{R_r}}{0.332 \left[ \log_{10} (R_r + 3000) \right]^{2.584}} \right\} \quad (A19)$$

where  $R_r$  is evaluated using equation (A3). Equation (A3) after slight modification, can be expressed as

$$R_r = \frac{\rho_r \mu_r u_e x}{\mu_o^2 F_x^2} \left( \frac{x_{eq,L}}{x} \right) \quad (A20)$$

where  $F_x$  is evaluated by the expression

$$F_x = \left[ \frac{(x_{eq,T}/x)}{(x_{eq,L}/x)} \right]^{1/3} \quad (A21)$$

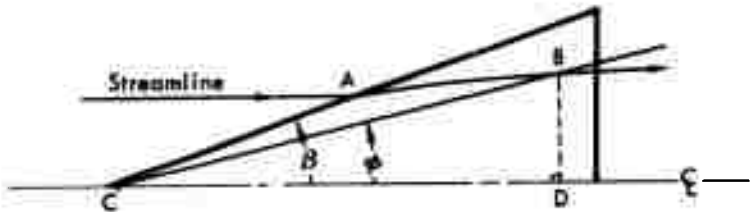
The reference Reynolds number is also dependent on the streamline divergence parameter  $n$ .

## 2. METHOD AT SPANWISE LOCATION

### a. At Low Angles of Attack

The spanwise heating distribution at low angles of attack can be expressed in terms of centerline heating using geometric considerations alone. Thermodynamic gas properties and the velocity are assumed to be constant on the lower surface so that the heat-transfer decay is a function of distance only.

Consider the streamline "AB" in the following sketch:



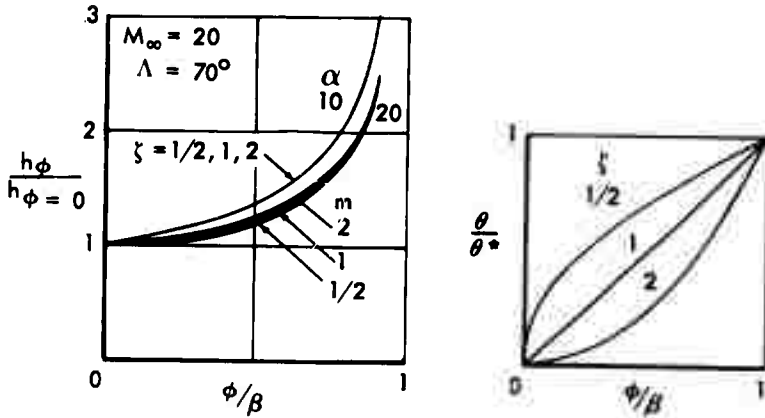
The point on the centerline corresponding to the point "B" is at "D" so that the comparable centerline distance is CD. Because all properties have been assumed constant, the heat transfer relationship at "B" which intersects the ray angle  $\phi$

in terms of that at "D" which lies along the ray angle  $\phi = 0$  can be written as:

$$\frac{h_\phi}{h_{\phi=0}} = \left(\frac{CD}{AB}\right)^m \quad (A22)$$

where  $m$  has the value 0.5 in laminar flow and 0.2 in turbulent flow as in classical flat plate theory.

The distance "AB" can be calculated once the spanwise distribution of the outflow angle,  $\theta$ , is known. The outflow angle distribution is assumed to vary according to the relationship  $\theta/\theta^* = (\theta/\beta)^\zeta$ . At low angles of attack, the spanwise heat transfer distributions are relatively insensitive to the value of the exponent  $\zeta$ , in this expression within the limits  $0.5 \leq \zeta \leq 2$ . This is illustrated in the sketch below for three values of  $\zeta$ , at  $M_\infty = 20$  and  $\alpha = 10$  degrees and 20 degrees.



The differences between the distributions computed for the range of  $\zeta$  between 0.5 and 2 are typical for the range of sweep angles and Mach numbers considered in this study. In extrapolation factor computations, the same value of the exponent  $\zeta$  was used for calculation of spanwise heat-transfer at wind-tunnel and flight conditions

b. At High Angles of Attack

The  $\rho_r \mu_r$  momentum integral method is applied in the analysis of spanwise heat transfer at high angles of attack. The solution is obtained numerically by forward integration because the boundary-layer edge properties and the cross-flow pressure gradient are no longer constant along the streamline. The computation is made in two parts. First, a streamline is calculated on the lower surface and the thermodynamic gas properties, the velocity, and the cross-flow parameters

along this streamline are determined. Second, these variables are used to compute the heat-transfer distribution along the streamline using the integral form of the  $\rho_r \mu_r$  heat-transfer method. The streamline is calculated from the distributions of the local outflow angle shown in Appendix C. In most cases, a number of streamlines must be calculated in order to obtain solutions for all spanwise locations.

## APPENDIX B

### METHOD OF FLOW FIELD SOLUTION IN PROXIMITY TO THE CENTERLINE FOR SHARP UNYAWED DELTA WINGS

Previous methods for computing thermodynamic gas properties on sharp delta wings employed Newtonian or modified-Newtonian techniques which neither differentiated between real and ideal-gas flows nor accounted for variations in leading-edge sweep angles.

The method presented in this appendix was developed to compute thermodynamic gas properties at the surface in proximity to the centerline of a sharp unyawed delta wing at angle of attack. It is strictly applicable to delta wings having leading-edge sweep angles in the range 70 to 80 degrees in ideal or real-gas flows and thermochemical equilibrium. This method makes use of a similarity parameter which in essence permits the calculation of the gas properties near the centerline without using the method of characteristics. The value of the similarity parameter is based upon correlations of analytic and experimental results.

Additionally, a technique is developed for evaluating cross-flow pressure gradient effects at the centerline.

#### 1. DEVELOPMENT OF THE SIMILARITY PARAMETER

Flow-field solutions are normally difficult to obtain for complex geometries without some idealization or mathematical simplification. Quite often a complex flow field can be separated into parts, where each part can be analyzed using an idealized flow-field model. For example, the unyawed sharp-cone flow field can be separated into two parts, a two-dimensional shock wave and an isentropic shock layer between the shock and the body surface. Normally, solutions for sharp-cone flows require the use of the method of characteristics and standard shock crossing relationships (see for example references 40 and 41). Both flow-field parts must be solved simultaneously. If, however, some information about each of the parts were known beforehand, a solution could be obtained in a simpler manner.

Upon examination of existing solutions across shock waves generated by wedges and sharp unyawed cones, it was observed that the parameter denoted by  $S$  as shown below assumes a unique numerical value for each geometry.

$$S = \frac{\rho_2}{\rho_\infty} \frac{\tan(\theta - \alpha)}{\tan \theta} \quad (B1)$$

where  $\rho$ ,  $\theta$ , and  $\alpha$  are the density, the shock wave angle, and the deflection angle, respectively. These parameters are illustrated for wedges and sharp cones in the sketches below:



The subscript 2 denotes conditions immediately downstream of the shock wave. For wedge flows,  $S$  always assumes a value of unity because the expression for it is a form on the continuity equation for steady two-dimensional oblique shock flows. Values of  $S$  calculated from exact solutions for sharp cones are shown in figure B1 as a function of the Mach number normal to the body surface. In the regime where the flow normal to the body is supersonic, it is seen that the value of  $S$  is approximately 0.5.

The similarity parameter,  $S$ , when once defined for a particular geometric element can be used to predict some surface gas property. In the present analysis surface pressure is correlated to  $S$ . This correlation is discussed later in this section.

The fact that  $S$  is nearly constant and independent of real-gas effects for both wedges and sharp cones suggests that it may also be independent of real-gas effects for a sharp delta-wing flow field in proximity to the centerline where the shock wave has zero curvature. For sharp delta wings at high angles of attack, outflow occurs over the leading edges and affects the flow field at the centerline. The volume of outflow is dependent upon real-gas effects so that a change in out-flow can change the value of  $S$  at the centerline. It will be shown that while the real-gas effect on  $S$  is significant at high angles of attack, the resultant effect on thermodynamic gas properties at the surface is not. Despite this relatively small resultant effect, a real-gas correction to  $S$  has been used in the real-gas analysis.

#### a. Similarity Parameter for Sharp Delta Wings

Variation of the similarity parameter for sharp delta wings is shown in figure B2. At high angles of attack, the values for the similarity parameter were correlated to flow-field solutions obtained using the method of reference 36. At low angles of attack, values for  $S$  were obtained through correlations of surface pressure data (references 42 and 43) and schlieren photographs of shock shape (reference 44). Because pressure data generally is accurate to about  $\pm 5\%$ , some scatter in the values calculated for  $S$  can be expected. The values calculated for  $S$  are very sensitive to pressure. This is shown in

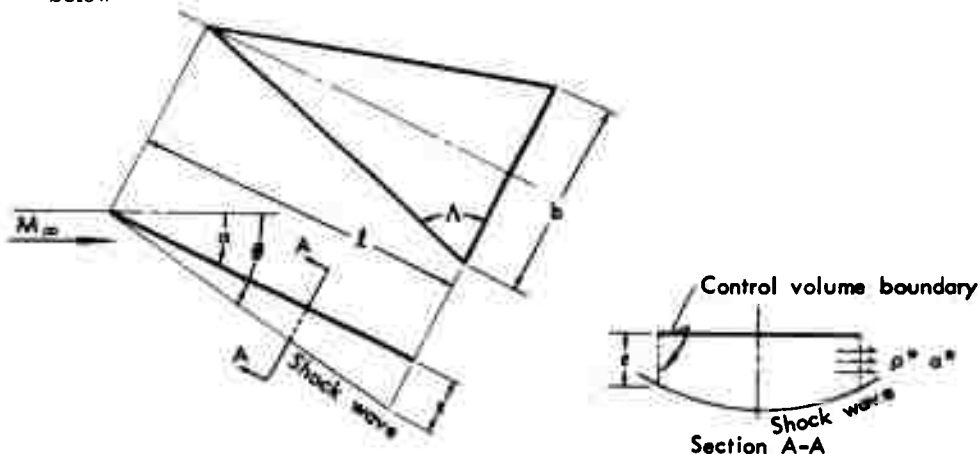
figure B2 by the band that indicates the variation in  $S$  due to a 5% change in surface pressure. Nevertheless, this sensitivity indicates that a high degree of accuracy in  $S$  is not necessary, since a sizable error in  $S$  will only produce a moderate error in flow-field and surface properties.

At low angles of attack,  $S$  approaches unity (i. e., the conical shock wave and flow field begin to resemble a wedge shock wave and flow field). Also, at low angles of attack, the pressure data indicate that viscous effects have become significant. These effects tend to increase the value of the similarity parameter. Analytic methods for determining these effects on delta-wing flow fields are not yet available. The analysis presented here neglects viscous effects.

### b. Real-Gas Effect on the Similarity Parameter

The value of the similarity parameter on delta wings is increased by real-gas effects. This increase is due to a reduction in the amount of mass that leaves the lower surface over the leading edges. An estimate of the increase in  $S$  is obtained using the following analysis.

Assume that a sharp flat delta wing at angle of attack  $\alpha$  generates a flat shock wave at an angle  $\theta$  to the free-stream flow as illustrated in the sketch below



Also assume that the density  $\rho_2$  in the shock layer is constant and that the lower surface velocity  $u_2$  in the streamwise direction is constant and of a magnitude equal to that at the centerline. Assume that the flow in the plane normal to the lower surface at the leading edge is sonic and directed outward. This model is reasonable at high angles of attack where the delta wing resembles a blunt body in the plane normal to the wing surface.

The mass rate entering into the shock layer is

$$\dot{m}_{in} = \rho_{\infty} (u_{\infty} \sin \theta) \frac{b f}{2 \cos(\theta - \alpha)} \quad (B2)$$

The mass rate leaving at the trailing edge is

$$\dot{m}_{te} = \rho_2 u_2 b \epsilon \quad (B3)$$

The mass rate leaving at the leading edge is

$$\dot{m}_{le} = \frac{1}{2} b \epsilon (\rho^* a^* / \cos \Lambda - \rho_2 u_2) \quad (B4)$$

where the asterisk indicates sonic conditions. Balancing the mass flow, we get

$$\dot{m}_{in} = \dot{m}_{te} + \dot{m}_{le} \quad (B5a)$$

$$\rho_{\infty} u_{\infty} \sin \theta \frac{b f}{2 \cos(\theta - \alpha)} = \rho_2 u_2 b \epsilon + \frac{1}{2} b \epsilon (\rho^* a^* / \cos \Lambda - \rho_2 u_2) \quad (B5b)$$

Now make the assumption that  $\rho^* \approx \rho_2$ . For purposes in this analysis, this assumption will intensify the expected differences.

Divide the above equation by  $\rho_2 u_2 b \epsilon$

$$\frac{\rho_{\infty} u_{\infty}}{\rho_2 u_2} \frac{f}{\epsilon} \frac{\sin \theta}{\cos(\theta - \alpha)} = 1 + \frac{a^*}{u_2 \cos \Lambda} \quad (B6)$$

Because  $\epsilon / f = \tan(\theta - \alpha)$  and  $u_2 / u_{\infty} \approx \cos \theta / \cos(\theta - \alpha)$ , then

$$\frac{\rho_2 \tan(\theta - \alpha)}{\rho_{\infty} \tan \theta} = \frac{1}{1 + \frac{a^*}{u_2} \sec \Lambda} \quad (B7)$$

The left-hand side of the above equation, by definition, is the similarity parameter so that

$$S = \frac{1}{1 + \frac{a^*}{u_2} \sec \Lambda} \quad (B8)$$

A more accurate relationship for S was developed by correlating sharp delta wing flow field results obtained using the method of reference 36. This correlation resulted in the expression

$$S = \frac{1}{1 + 0.6 \frac{a^*}{u} \sec \Lambda} \quad (\text{B9})$$

where u is the centerline velocity.

The factor, 0.6, in equation (B9) takes into account the changes in velocity, density in the shock layer, and the shock-wave profile in the spanwise direction. Equation (B9) is compared to the results of reference 36 in figure B3. The symbols shown in this figure represent solutions for sharp delta wings at various angles of attack, angles of leading edge sweep, Mach numbers, and ratios of specific heats,  $\gamma$ . Independence of  $\gamma$  indicates that the correlation is applicable to real-gas flows. Because  $a^*$  can be significantly smaller in a real gas than it is in an ideal gas at high angles of attack, the real-gas value for S can be substantially larger than the ideal-gas value. Results shown in figure B4 indicate that changes in S are significant at high angles of attack, but the resulting change in the shock-wave angle is small.

At low angles of attack, values for S obtained using equation (B9) are slightly higher than those proposed in figure B2. At low angles of attack, however, equation (B9) is not expected to be valid because  $\frac{a^*}{u} \sec \Lambda$  is no longer a characteristic parameter of the flow field. Also, real-gas effects on S at low angles of attack are small. S is obtained directly from figure B2 at low and moderate angles of attack.

The ratio of the differences in S that can be expected for real-gas flows and flows at  $\gamma = 1.4$  has been correlated in terms of the leading edge sweep angle,  $\Lambda$ , angle of attack,  $\alpha$ , and the edge enthalpy,  $i_e$ , in Btu/lbm. This correlation is represented by the relationship

$$\frac{S_{\text{real}}}{S_{\text{ideal}}} = 1 + 0.385 \left( \frac{\Lambda}{70^\circ} \right) \left( \frac{\alpha}{60^\circ} \right)^2 \left[ \log_{10} i_e - 2.7 \right] \quad (\text{B10})$$

which is compared with analytical data in figure B5.

## 2. SOLUTION FOR THERMODYNAMIC GAS PROPERTIES

The method used to obtain gas properties along the centerline of the sharp delta wing surface consists of two parts. First, shock-wave inclination and the corresponding properties downstream of the shock wave are determined in the

plane normal to the delta-wing surface at the centerline. Second, the properties at the delta-wing surface are calculated by using the similarity parameter in evaluating the surface pressures. Each of the processes is discussed in subsequent sections.

a. Shock-Wave Solution

The solution across the shock wave is obtained by simultaneously satisfying the standard shock relationships

$$\rho_{\infty} u_{\infty} = \rho_2 u_2 \quad (B11)$$

$$P_{\infty} + \rho_{\infty} u_{\infty}^2 = P_2 + \rho_2 u_2^2 \quad (B12)$$

$$i_{\infty} + \frac{u_{\infty}^2}{2} = i_2 + \frac{u_2^2}{2} \quad (B13)$$

and the expression for the similarity parameter defined by equation (B1). The symbols  $\rho$ ,  $P$ , and  $i$  represent density, pressure, and enthalpy, respectively,  $u$  is the velocity normal to the shock wave, and the subscripts  $\infty$  and 2 refer to conditions in the free-stream and immediately downstream of the shock wave, respectively.

b. Compression Technique Through the Shock Layer

After the shock-wave angle is determined and the gas properties downstream of the shock wave evaluated, compression through the shock layer to the surface of the delta wing must be computed. For conical flows, the compression takes place isentropically. To evaluate this compression, however, one of the gas properties at the surface must be known.

Surface properties for the delta wing can be determined analytically using the method of characteristics, but because such a method is very difficult, an approximate technique was developed.

This technique is based on a correlation between the pressure ratio ( $P_e/P_s$ ) on a delta wing, the pressure ratio on a cone, and the similarity parameter. The similarity parameter  $S$  was developed because a correlation equation such as the one proposed, which shows real-gas and leading-edge sweep-angle effects on a surface gas property, was desired. A correlation equation in terms of these three parameters is expressed as

$$(P_e/P_s)_{\text{Delta wing}} = 1 + 2 \left[ (P_e/P_s)_{\text{Cone}} - 1 \right] (1 - S) \quad (B14)$$

Equation (B14) is justified using the following physical reasoning and analytic solutions.

Figure B6 shows a ratio of pressures at the body surface and at the shock wave for sharp cones, as a function of Mach number normal to the shock wave. The curves shown on this figure represent solutions using the method of characteristics. Because sharp delta wing flows at high angles of attack are also conical, it can be expected that the value of the pressure ratio  $(P_e/P_s)$ , for the sharp delta wing will be of the same order as that for the sharp cone. In addition, pressure ratios obtained using the method of reference 36 can be correlated in terms of  $S$  to those obtained for a cone using the method of characteristics.

A comparison of equation (B14) and analytic delta wing data is presented in figure B7 for an ideal gas with  $\gamma = 1.4$ . Values for  $(P_e/P_s)$  in a real-gas flow are obtained using this correlation by first determining  $(P_e/P_s)_{\text{Cone}}$  and  $S$  in a real-gas flow.

### 3. PRESSURE COMPARISON

Surface pressures at the centerline of a sharp delta wing obtained using the method described above are compared with pressures calculated using the Boeing modified Newtonian method in figure B8. Comparisons are shown for a 70-degree swept sharp delta wing, a wedge, and a sharp cone as a function of the surface deflection angle. Differences between the two methods result in pressure differences on the delta wing on the order of 2-4% in a real gas and 7% in an ideal gas.

### 4. STREAMLINE DIVERGENCE PARAMETER

Sharp delta wing centerline heating is influenced by the cross-flow pressure gradient at the centerline. A method for determining this influence in an ideal gas was presented in reference 18 in terms of a streamline divergence parameter,  $n$ , defined as

$$n = \left( \frac{d\theta}{d\phi} \right)_{\phi=0} \quad (\text{B15})$$

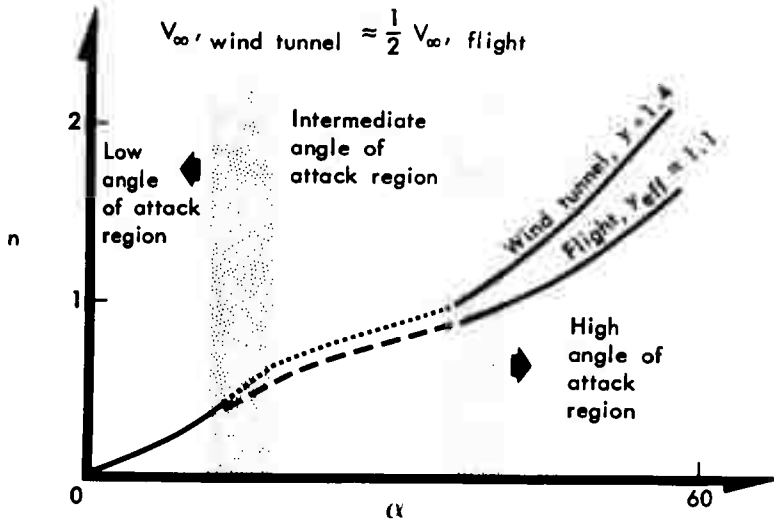
where  $\theta$  is the local outflow angle,  $\phi$  is the local ray angle and the subscript,  $\phi = 0$ , denotes that evaluation of the derivative is made at the centerline. The streamline divergence parameter appears explicitly in the heat-transfer relationships at the centerline, as was shown in Appendix A. In this report, results of reference 18 have been extended to include real-gas effects.

A correlation for  $n$  at high angles of attack was obtained from analytic solutions of reference 36 and is shown in figure B9. This correlation can be represented by the expression

$$n = 0.53 \left( \frac{1.4}{\gamma} \right)^{\frac{1}{3}} \left[ \frac{a^*}{u} \sec \Lambda \right] \quad (\text{B16})$$

where  $a^*$  is the sonic velocity at the leading edge,  $u$  is the centerline velocity,  $\Lambda$  is the sweep angle, and  $\gamma$  is the ratio of specific heats. The parameter  $a^*/u \sec \Lambda$  is the same parameter that appears in the correlation for  $S$  at high angles of attack.

The variation in  $n$  is illustrated schematically in terms of angle of attack in the following sketch.



In the high angle of attack region, equation (B16) is applicable. Values for  $n$  in this region are shown for typical wind-tunnel and flight conditions at a Mach number on the order of 20. The value for  $n$  is smaller for flight because the quantity  $a^*/u$  in equation (B16) is smaller in flight. At low angles of attack,  $n$  is calculated by the ideal-gas method proposed in reference 18. That method consists of a two-dimensional flow analysis near the leading edges for the angle of attack region where the shock wave is attached to the leading edge. Because shock waves are attached only at very low angles of attack, the method is strictly valid only in that region. Typical values are shown for this region in the left-hand portion of the preceding sketch.

In the intermediate angle of attack region, no theoretical solution for  $n$  is available. In reference 18, an interpolation between the solutions at low and high angles of attack was proposed. The high angle of attack solution is that of reference 36 for an ideal gas with  $\gamma = 1.4$ . The low and high angle of attack solutions were "fitted" to one another so that the interpolation resulted in the

most probable value for  $n$  in the intermediate angle of attack region. Values obtained in this way are illustrated by the dotted lines in the sketch. The above method was also used to evaluate  $n$  in the present study at intermediate angles of attack. Results for  $n$  at low and at intermediate angles of attack are shown in figure B10. Values obtained by this method have been corrected for real-gas effects by the equation shown below.

$$n_{\text{real}} = n_{\text{ideal}} \left\{ 1 - \frac{1}{2} (1 - C) [1 + \sin (3.6 \alpha - 90^\circ)] \right\} \quad (7)$$

In this equation,  $n_{\text{ideal}}$  is the value of the divergence parameter obtained by the ideal-gas method of reference 18 and  $C$  is a correction factor based on equation (B16) and defined as

$$C = \frac{\left(\frac{a^*}{u}\right)_{\text{real}}}{\left(\frac{a^*}{u}\right)_{\text{ideal}}} \left(\frac{1.4}{\gamma}\right)^{\frac{1}{3}} \quad (\text{B18})$$

Equation (B17) is tailored so that it fairs smoothly into real gas values for  $n$  at high angles of attack and also provides a diminishing amount of correction to  $n$  with decreasing angle of attack. At zero-degrees angle of attack, no correction is made. The "sine" function in equation (B17) provides a satisfactory "weighting" to the correction over the angle of attack range considered. The resulting distribution for  $n$ , obtained by equation (B17) for a typical flight case, is shown by the dashed line in the preceding sketch. The maximum differences in laminar centerline heating, with and without real-gas corrections to  $n$ , are approximately 7% in the intermediate angle of attack region.

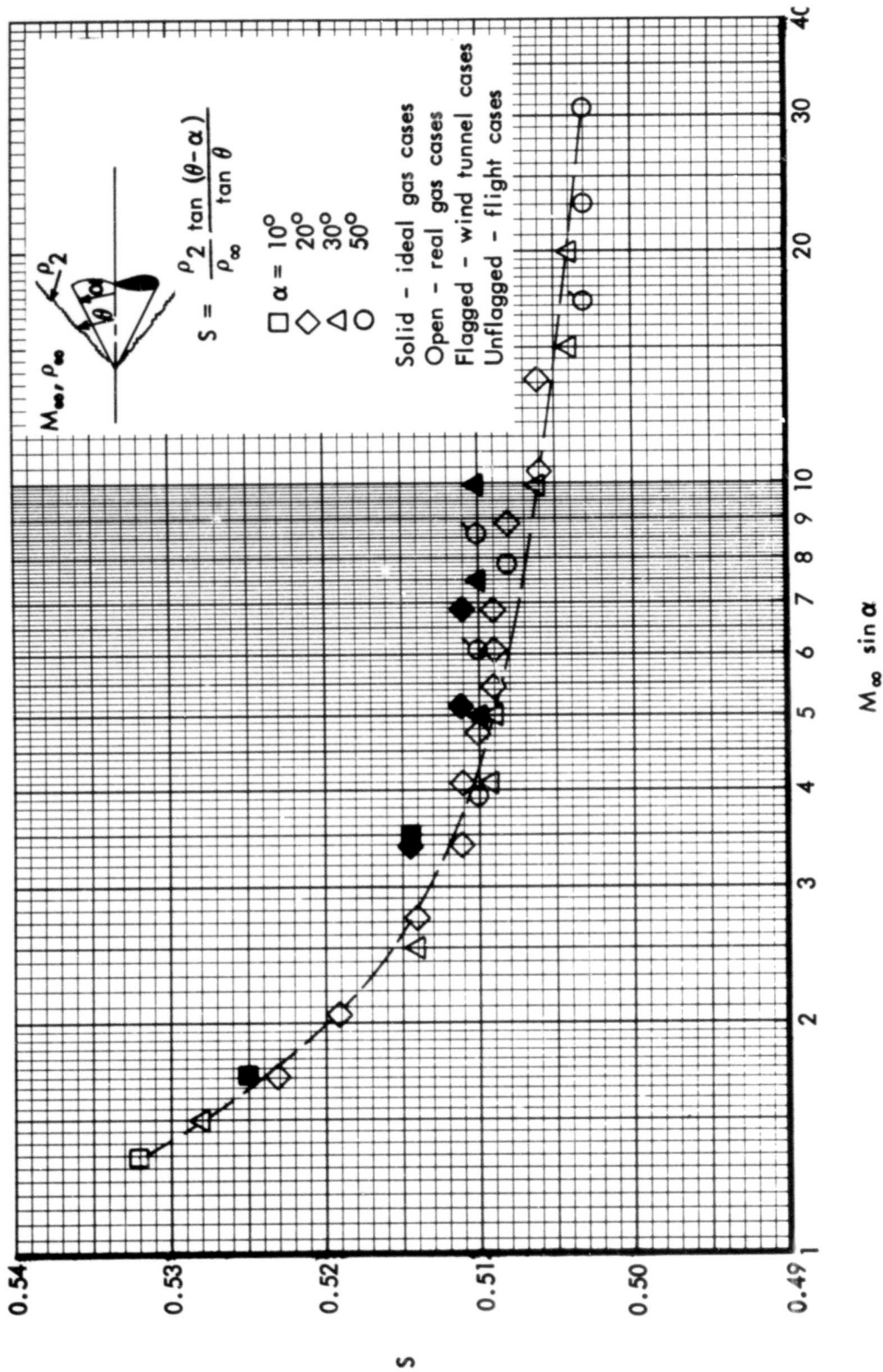


Figure B1: SIMILARITY PARAMETER FOR SHARP UNYAWED CONES

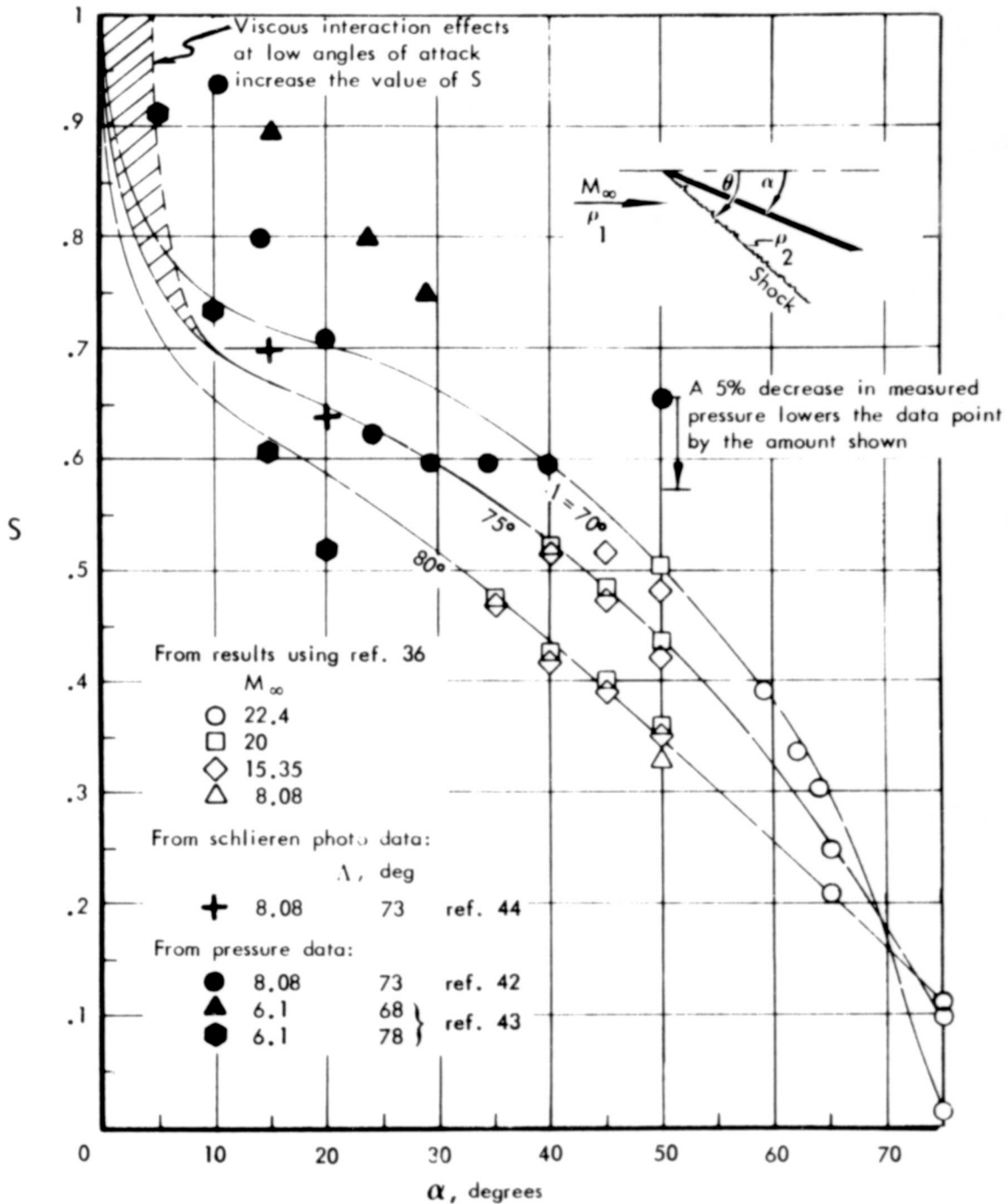


Figure B2: SIMILARITY PARAMETER FOR SHARP UNYAWED DELTA WINGS

Angles of attack range from 50° to 70°

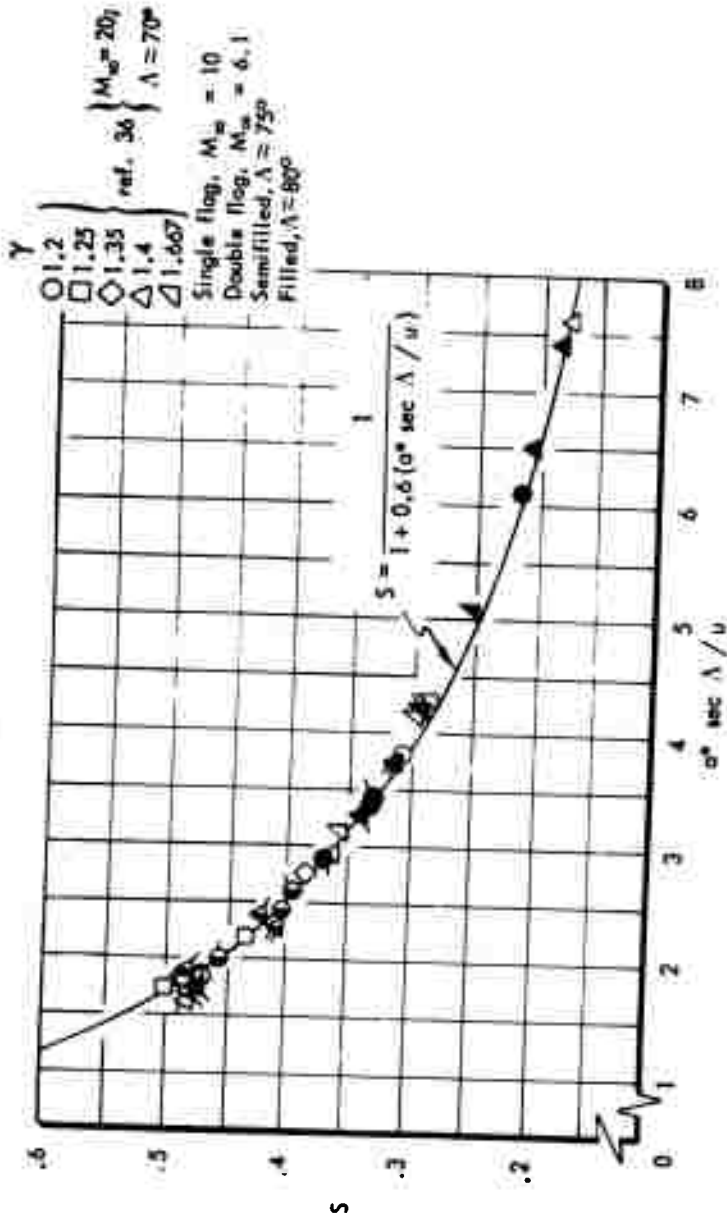
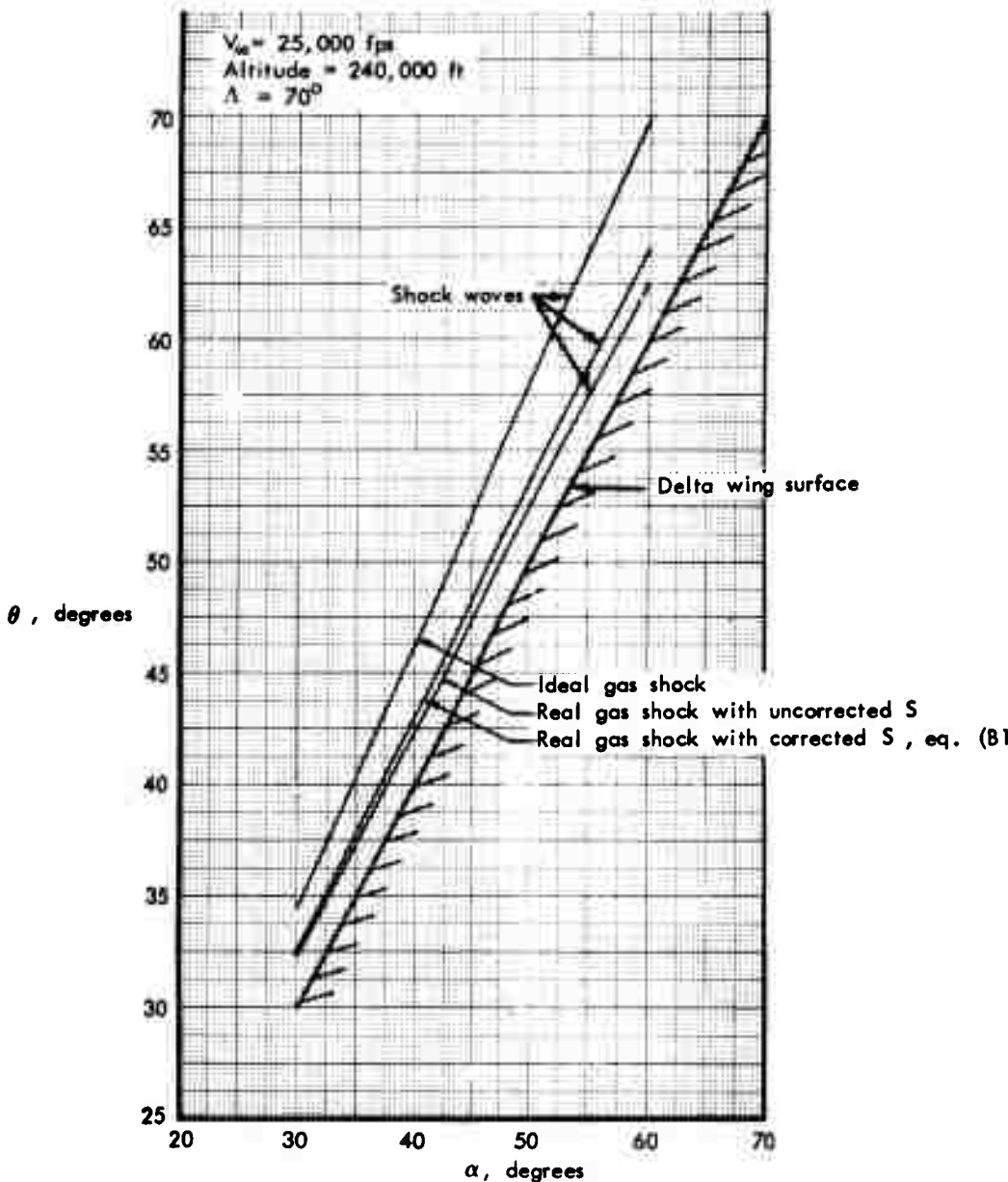


Figure B3: CORRELATION OF SIMILARITY PARAMETER FOR SHARP DELTA WINGS AT HIGH ANGLES OF ATTACK



**Figure B4: EFFECT OF CHANGES IN SIMILARITY PARAMETER ON CENTERLINE SHOCK WAVE GEOMETRY FOR SHARP DELTA WINGS**

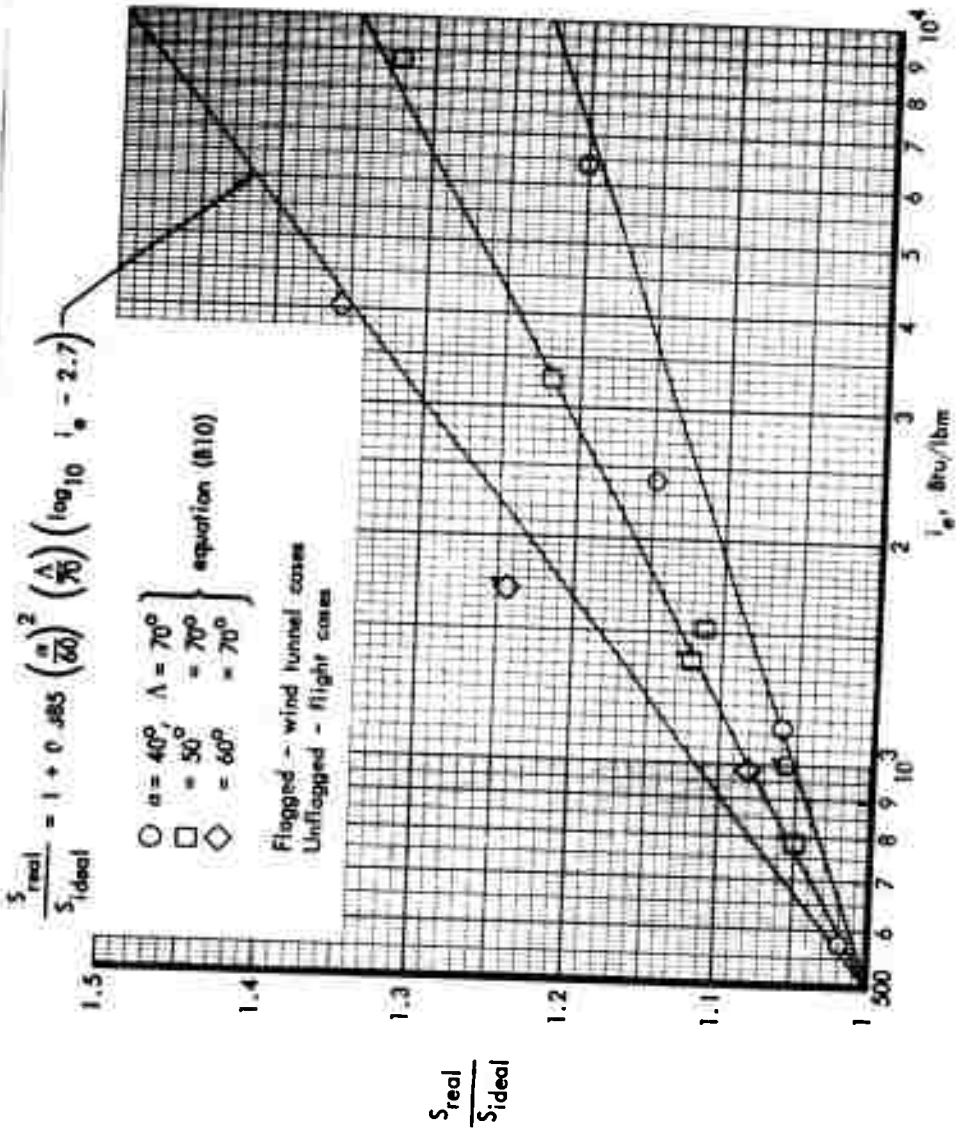


Figure B5: REAL-GAS CORRECTION TO SIMILARITY PARAMETER FOR SHARP DELTA WINGS

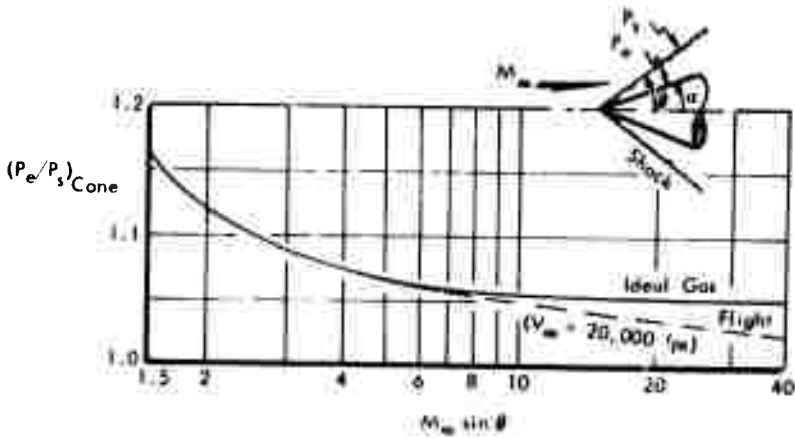


Figure B6: SHOCK LAYER PRESSURE RATIO FOR SHARP UNYAWED CONES

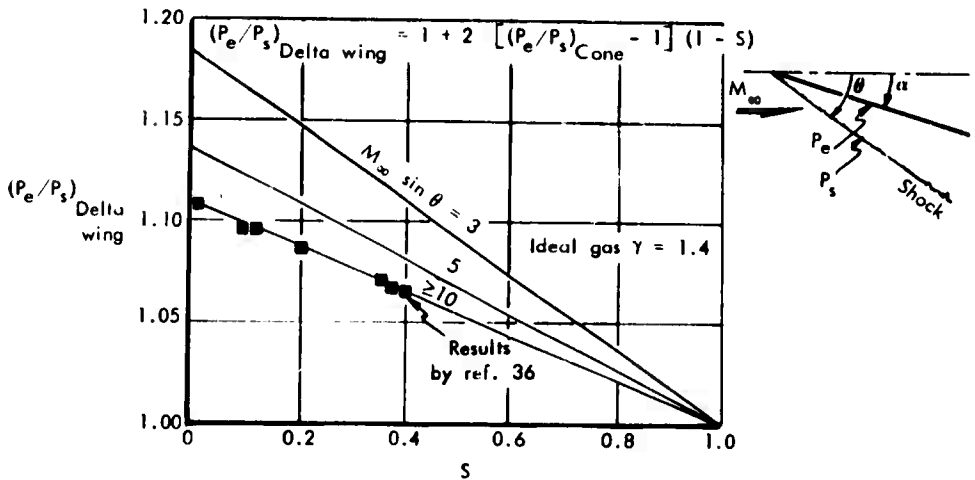


Figure B7: SHOCK LAYER PRESSURE RATIO FOR SHARP UNYAWED DELTA WINGS

P - Surface pressure by present technique

$P_{mN}$  - Surface pressure by Boeing modified Newtonian method (reference 2)

———— Ideal gas,  $M_\infty = 21.86$ ,  $\gamma = 1.4$

----- Real gas,  $V_\infty = 20,700$  fps, altitude = 240,000 ft ( $M_\infty = 21.86$ )

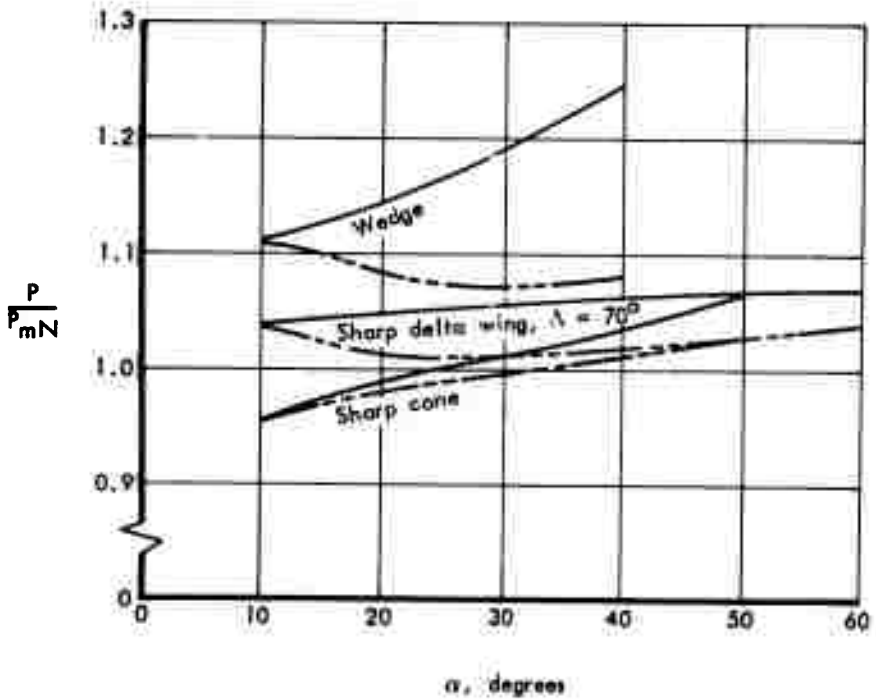


Figure B8: COMPARISON OF SURFACE PRESSURE WITH MODIFIED NEWTONIAN VALUES

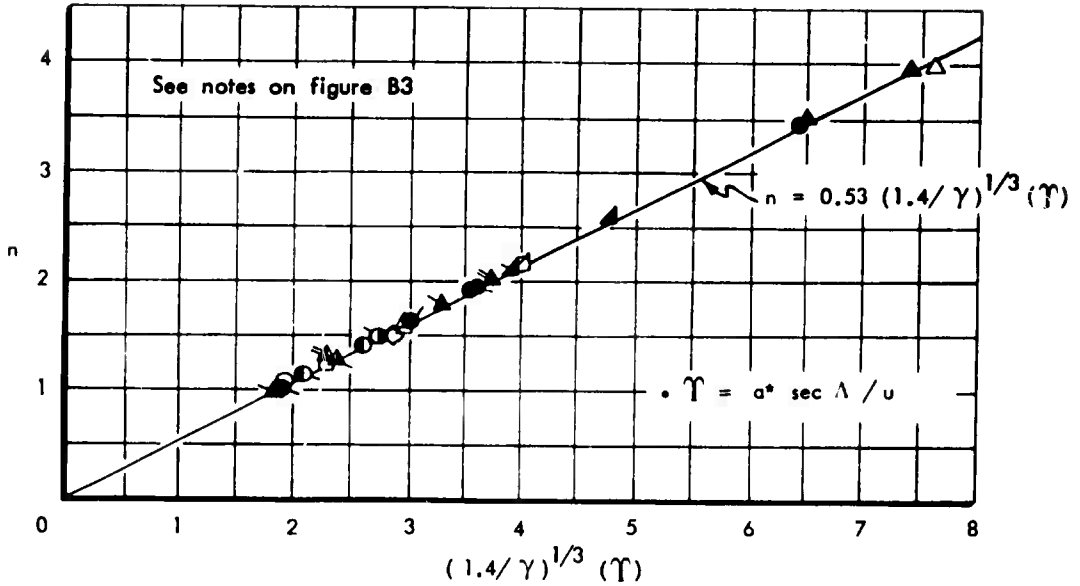


Figure B9: CORRELATION OF DIVERGENCE PARAMETER FOR SHARP DELTA WINGS AT HIGH ANGLES OF ATTACK

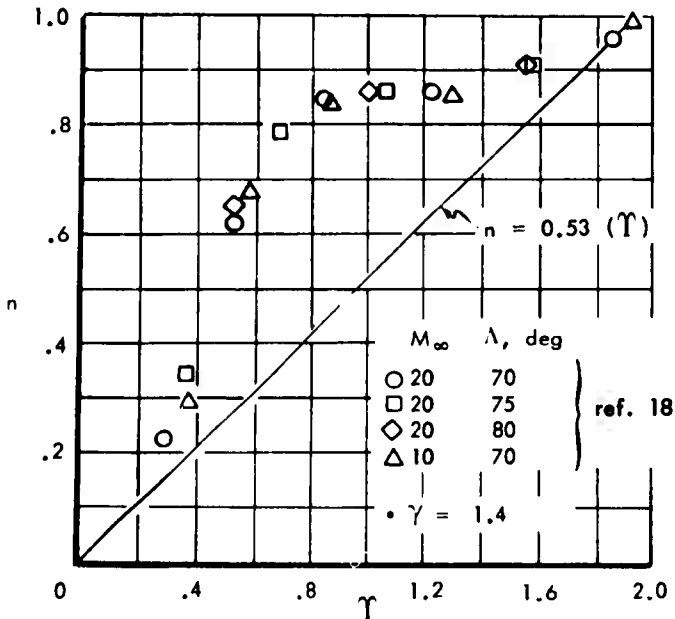


Figure B10: DIVERGENCE PARAMETER FOR SHARP DELTA WINGS AT LOW AND INTERMEDIATE ANGLES OF ATTACK

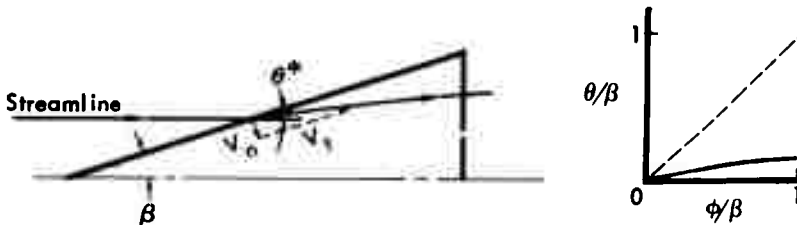
## APPENDIX C

### METHOD OF SPANWISE FLOW-FIELD SOLUTION FOR SHARP UNYAWED DELTA WINGS

Spanwise flow-field distributions are developed for the low and the high angle of attack regions for an infinitely thin sharp unyawed delta wing in an inviscid flow field. In the intermediate angle of attack region, an interpolation between the low and the high angle of attack distributions is proposed and discussed.

#### 1. LOW ANGLE OF ATTACK SOLUTIONS

At zero-degrees angle of attack in an inviscid flow field, the streamlines cross the leading edges of a thin sharp delta wing and always remain parallel to the centerline of the wing. The thermodynamic gas properties and the streamline direction on the lower surface are everywhere constant. With a slight increase in the angle of attack, however, the flow field begins to undergo a change. At the leading edge, the streamlines are deflected slightly away from the centerline by an angle  $\theta^*$  as illustrated in the sketch below:



When the shock wave is attached to the leading edges,  $\theta^*$  can be determined from the relationship

$$\theta^* = \beta - \tan^{-1} \left( \frac{V_n}{V_t} \right) \quad (C1)$$

where  $V_n$  and  $V_t$  are the velocity components on the surface perpendicular and parallel to the leading edge, respectively. The velocity component  $V_n$  is determined using the oblique-shock method with effective values for the Mach number and the flow-deflection angle. The effective values can be expressed in terms of the free-stream Mach number,  $M_\infty$ , angle of attack,  $\alpha$ , and geometric sweep angle,  $\Lambda$ , by the equations shown below:

$$M_{\text{eff}} = M_\infty \sqrt{1 - \cos^2 \alpha \sin^2 \Lambda} \quad (C2)$$

$$\delta_{\text{eff}} = \tan^{-1} (\tan \alpha \cdot \sec \Lambda) \quad (C3)$$

The velocity component  $V_t$  can also be expressed in terms of  $M_\infty$ ,  $\alpha$ , and  $\Lambda$  by the relationship

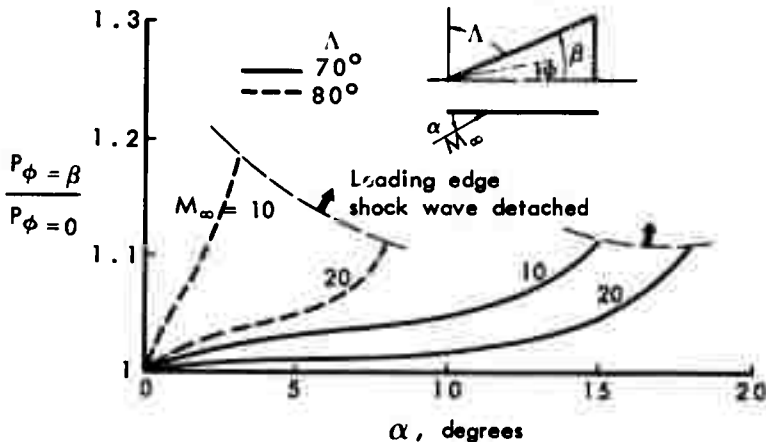
$$V_t = (M_\infty)(\cos \alpha)(\sin \Lambda) \quad (C4)$$

At the centerline, the local streamline angle,  $\theta$ , is zero because of symmetry. In reference 18,  $\theta$  was assumed to be constant within a region near the leading edge. This region was bounded by the outer Mach line of the velocity vector at the leading edge and the leading edge itself. Between the inner boundary of this region and the centerline, a sinusoidal variation of  $\theta$  was assumed. In this study,  $\theta$  was assumed to vary according to the relationship

$$\frac{\theta}{\theta^*} = \left(\frac{\phi}{\beta}\right)^\zeta \quad (C5)$$

where  $\zeta$  is on the order of unity or less. A value  $\zeta = 0.5$  approximates the distribution proposed in reference 18 reasonably well. It was shown in Appendix A that at low angles of attack the value of  $\zeta$  does not affect the heat-transfer results appreciably.

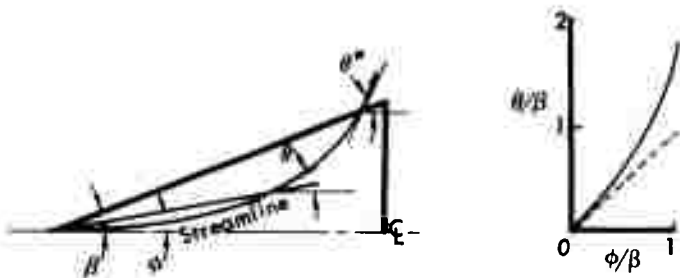
Pressure on the surface can be calculated by using an oblique-shock method at the leading edge and at the centerline for those cases where the shock wave is attached to the leading edge. Typical values of the ratio of leading-edge pressure to centerline pressure are shown in the following sketch.



The spanwise distribution of pressure must have a zero slope at the centerline because of symmetry. At the leading edge the slope must also be zero because of the assumption of oblique-shock flow in that region.

## 2. HIGH ANGLE OF ATTACK SOLUTIONS

At high angles of attack, spanwise flow-field solutions can be obtained using the analytical method of reference 36. In that reference, it is shown that the flow in the plane perpendicular to the delta wing surface can be treated as flow over a blunt body having a cross-flow velocity at the leading edge equal to the local sonic velocity. Because of conical symmetry, all properties along ray lines emanating from the apex are constant and the calculation involves only two dimensions. All streamlines along the surface appear to emanate at the apex of the wing as shown on the left in the sketch below. The corresponding distribution of the local streamline angle is shown on the right.



In the subsequent development of spanwise distributions, knowledge of the value of the streamline angle,  $\theta^*$ , at the leading edge is essential. A correlation for  $\theta^*$  from the analytic solutions has been made in terms of the parameter  $a^*/u$  and  $\beta$ , where  $a^*$  is the local sonic velocity at the leading edge,  $u$  is the centerline velocity, and  $\beta$  is defined as  $(90^\circ - \Lambda)$ . This correlation is shown in figure C1 for several values of  $M_\infty$ ,  $\alpha$ ,  $\Lambda$ , and  $\gamma$ .

$$\theta^* = \tan^{-1} \left[ \left( \frac{a^*}{u} \right) - 0.07 \left( \frac{a^*}{u} \right)^2 \right] + \beta \quad (C6)$$

The parameter  $\theta^*$  serves as both a normalizing and a correlating factor for the local pressure and the local streamline angle. The spanwise pressure distribution is required to determine the local thermodynamic gas properties, whereas the local streamline angle is essential in determining the amount of the local flow divergence. Distributions for these parameters are shown in figures C2 and C3 in terms of the parameter,  $n/[\theta^* \sec \Lambda]$ . The correlations which these distributions are based on are shown in figures C4 and C5.

The distributions for  $n/[\theta^* \sec \Lambda] > 1$  are shown by dashed lines. Physically, it is unlikely that values of  $n/[\theta^* \sec \Lambda] > 1$  can occur. This conclusion may be reached by recognizing that the local slope of the streamline angle distribution must decrease in the spanwise direction when  $n/[\theta^* \sec \Lambda] > 1$ . Correspondingly, the pressure must increase in the spanwise direction which is in opposition to the results obtained by blunt-body analogy. Solutions

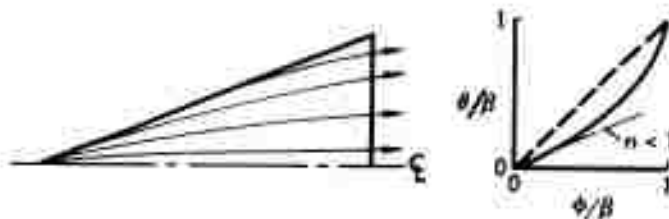
with  $n / [ \theta^* \sec \Lambda ] > 1$  indicate that some of the assumptions in the method are not satisfied. However, we are using the best available method and it would be a major task to improve on these solutions.

### 3. INTERMEDIATE ANGLE OF ATTACK SOLUTIONS

The lower-surface flow-field results at high and low angles of attack have been discussed in previous sections and may be summarized as follows. The streamline angle at the leading edge increases from the value zero at zero-degrees angle of attack to a value greater than  $\beta$  at high angles of attack. Physically, at low angles of attack, the flow enters over the leading edge and is discharged over the trailing edge. At high angles of attack, the surface flow behaves as if it originated at the apex of the wing. It flows downstream, diverging away from the centerline and eventually discharges over the leading edge. The streamline angle and pressure distributions can be expressed in terms of the local ray angle,  $\phi$ , and at high angles of attack are uniquely defined by an additional parameter  $n / [ \theta^* \sec \Lambda ]$ .

A spanwise distribution of the local streamline angle,  $\theta$ , may be constructed in the intermediate angle of attack region using the preceding development. By knowing both the value and the slope of the distribution at the centerline and the value at the leading edge, a distribution profile between the leading edge and the centerline can be assumed. Values for the slope,  $n$ , and the streamline angle,  $\theta^*$ , may be obtained using correlations developed previously in the text. The streamline angle at the centerline is zero because of symmetry.

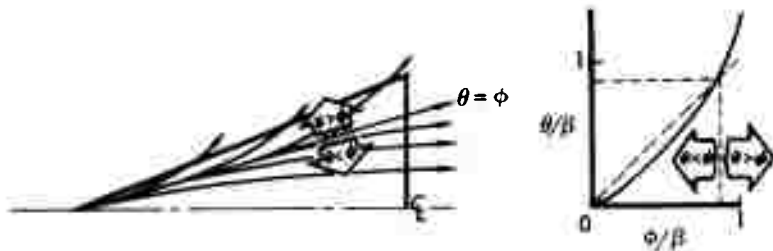
At some intermediate angle of attack,  $\alpha_1$ , the streamline angle,  $\theta^*$ , at the leading edge is equal to the leading-edge ray angle,  $\beta$ . For all angles of attack greater than the angle  $\alpha_1$ , flow is "expelled" over the leading edge (i.e.,  $\theta^* > \beta$ ). For all  $\alpha < \alpha_1$ , flow enters the lower surface by crossing the leading edge (i.e.,  $\theta^* < \beta$ ). The streamline pattern and the corresponding streamline angle distribution for the case where  $\theta^* = \beta$  are illustrated in the sketch below.



The slope  $n$  at the centerline is less than unity.

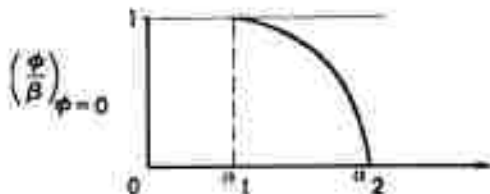
With increasing angle of attack, outflow occurs over the leading edges (i.e.,  $\theta^* > \beta$ ). The correlation for  $n$  indicates that the value of  $n$  remains below unity for a range of angles of attack above  $\alpha_1$ . The angle of attack at

which  $n = 1$  can be denoted by  $\alpha_2$ . In the angle of attack region between  $\alpha_1$  and  $\alpha_2$ ,  $\theta^* > \beta$  and  $n < 1$ . The streamline pattern and the streamline angle distribution in the region  $\alpha_1 < \alpha < \alpha_2$  are typified in the sketch below.



The flow field has a "parting line" which is defined by the ray angle,  $\theta = \phi$ . The flow outboard of this parting line spills over the leading edges of the wing. The flow on the inboard side passes over the trailing edges. A particle at the location where  $\theta = \phi$  remains at that angular location with increasing distance from the apex. In order for the streamlines to assume a pattern as shown in the sketch above, pressure must be a maximum at the parting line. The slope at the centerline must be zero and the value at the leading edge must be on the order of the pressure which corresponds to the local sonic pressure.

The change in location of the "parting line" with angle of attack is shown schematically in the following sketch:



At the angle of attack  $\alpha_1$ , the dividing streamline is located at the leading edge, i.e.,  $\theta^* = \beta$ . With increasing angle of attack, this dividing streamline shifts inward and eventually reaches the centerline at an angle of attack,  $\alpha_2$ . Above  $\alpha_2$ , and below  $\alpha_1$ , there is no dividing streamline. Between the limits  $\alpha_1$  and  $\alpha_2$ , however, the dividing streamline plays an important part in determining the flow-field and heat-transfer distributions.

#### 4. FLOW-FIELD REGIONS

A composite of all types of flow-field patterns is shown schematically in figure C6 in terms of angle of attack and Mach number. In this figure, the first flow-field region is bounded by  $\alpha = 0$  and the angle of attack at which the leading-edge streamline angle,  $\theta^*$ , coincides with the leading edge (i.e.,  $\theta^* = \beta$ ). Within this region, flow passes over the leading edge onto the lower

surface. This condition is illustrated by the lower three sketches on the right-hand portion of this figure. Sketch 1 illustrates the lower-surface streamline pattern at  $\alpha = 0$ , sketch 2 shows a typical pattern in this flow-field region, and sketch 3 indicates the pattern when  $\theta^* = \beta$ . The next region has an upper bound defined by  $(d\theta/d\phi)_{\phi=0} = 1$ , a lower bound defined by  $\theta^* = \beta$ , and a flow field characterized by a "parting line" or dividing streamline. This condition is illustrated in sketch 4. At the upper boundary, the parting line has reached the centerline of the lower surface and all flow emanates from the apex of the wing and away from the centerline. The third and fourth regions occur at high angles of attack and are characterized by the condition  $\theta > \phi$  for all spanwise locations other than the centerline. The third region corresponds to flows which are everywhere supersonic on the lower surface. It is in this region where the method of reference 36 is valid. The fourth region occurs at very high angles of attack where some portion of the lower-surface flow-field velocity is sonic or subsonic. The lower bound of this region is defined by the condition where the Mach number at the centerline is unity. At higher angles of attack, the total velocity component becomes subsonic at the centerline and moves the sonic line further outboard. At 90-degree angle of attack, the sonic line would coincide with the leading edge. The subsonic region of flow is outside the limits of the present analysis.

Streamline angle profiles over the lower surface of the sharp delta wing are shown schematically in figure C7. These profiles have been drawn to correspond to the flow-field regions shown on figure C6. At  $\alpha = 0$ , the streamline angle,  $\theta$ , is zero, and all streamlines are parallel to the centerline. This is depicted in sketch 1. As the angle of attack is increased, the streamlines are deflected away from the centerline as they cross the leading edge. This is shown by the streamline angle profiles pertaining to sketch 2. The situation where the leading-edge streamline angle,  $\theta^*$ , is equal to the leading-edge sweep angle,  $\beta$ , is depicted by the distribution corresponding to sketch 3. At this point, the dividing streamline coincides with the leading edge. As the angle of attack of the delta wing is increased  $\theta^*$  becomes larger than  $\beta$  and the lower surface assumes a streamline angle distribution like that shown for sketch 4. The dividing streamline has shifted away from the leading edge and is located at  $(\phi/\beta)_{\theta=\phi}$ . With increasing angle of attack, the dividing line shifts more and more toward the centerline. The point at which the dividing streamline has just reached the centerline is defined by  $(d\theta/d\phi)_{\phi=0} = 1$ . The flow field for this situation is typified in sketch 5. At still higher angles of attack,  $(d\theta/d\phi)_{\phi=0} > 1$  and the streamline angle distribution is like that shown for sketch 6.

Spanwise pressure profiles corresponding to the flow regions discussed in the previous paragraphs are shown in figure C8. At zero degrees angle of attack, no flow divergence is encountered and the pressure distribution is constant. At low and intermediate angles of attack the pressure increases in the spanwise direction. This is illustrated by the distributions pertaining to sketches 2 and 3 in the figure. For a flow field with a parting streamline,

pressure is at a maximum at the parting streamline. This is indicated by the distribution pertaining to sketch 4. For this case, the pressure at the leading edge is on the order of the local sonic pressure. At high angles of attack, the pressure distributions are typified by those pertaining to sketches 5 and 6 in the figure. The pressures at the leading edge are equal to the local sonic pressures.

The location of the dividing streamline, defined by the ray angle  $\theta = \phi$ , is sensitive to the angle of sweep, the free-stream Mach number, and the total enthalpy. This is depicted in figure C9 for a delta wing of 70-degrees sweep at free-stream Mach numbers of 10 and 20. The important feature to be recognized in this figure is the marked difference in location of the dividing streamline between flows of different total enthalpies.

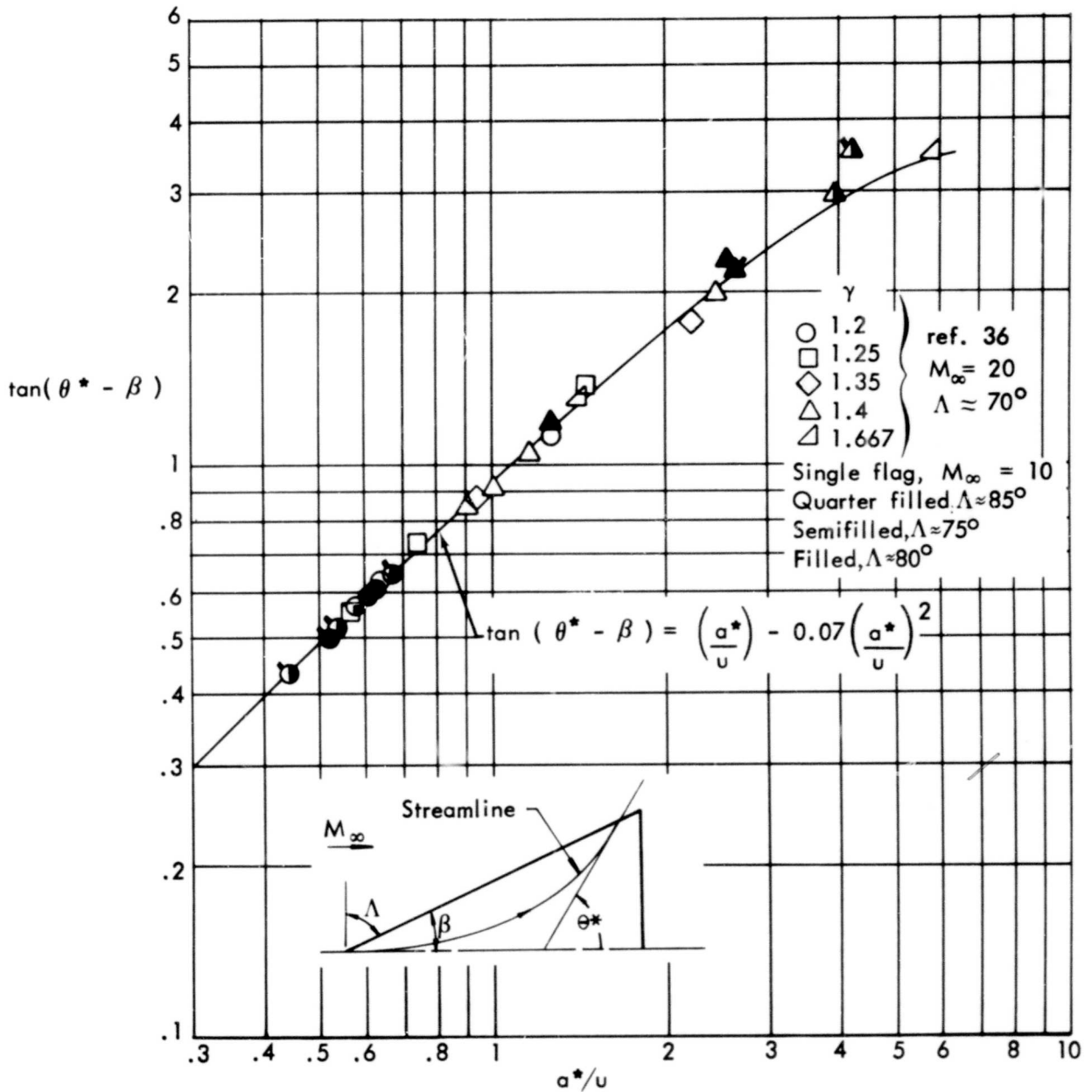


Figure C1: CORRELATION FOR LEADING EDGE STREAMLINE ANGLES AT HIGH ANGLES OF ATTACK

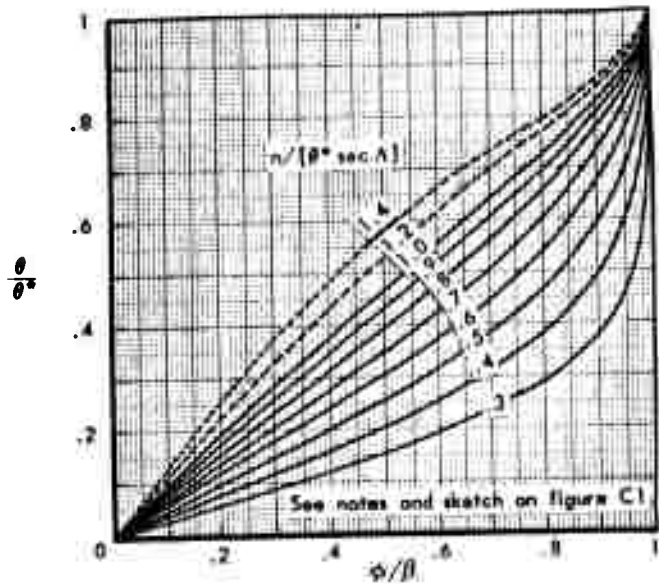


Figure C2: SPANWISE STREAMLINE ANGLE DISTRIBUTION AT HIGH ANGLES OF ATTACK

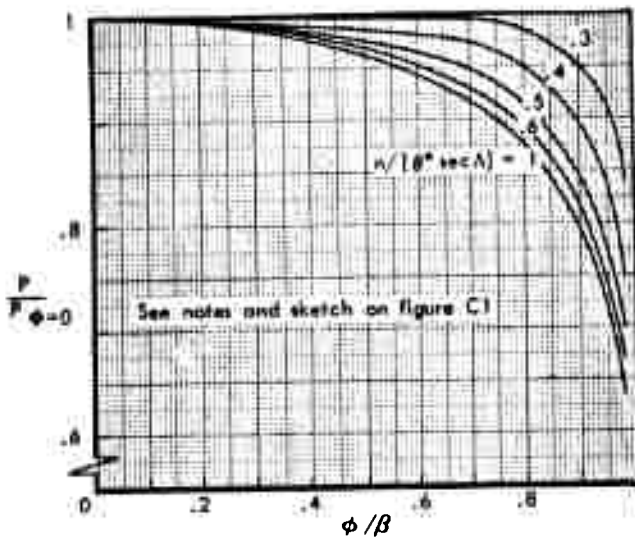


Figure C3: SPANWISE PRESSURE DISTRIBUTION AT HIGH ANGLES OF ATTACK

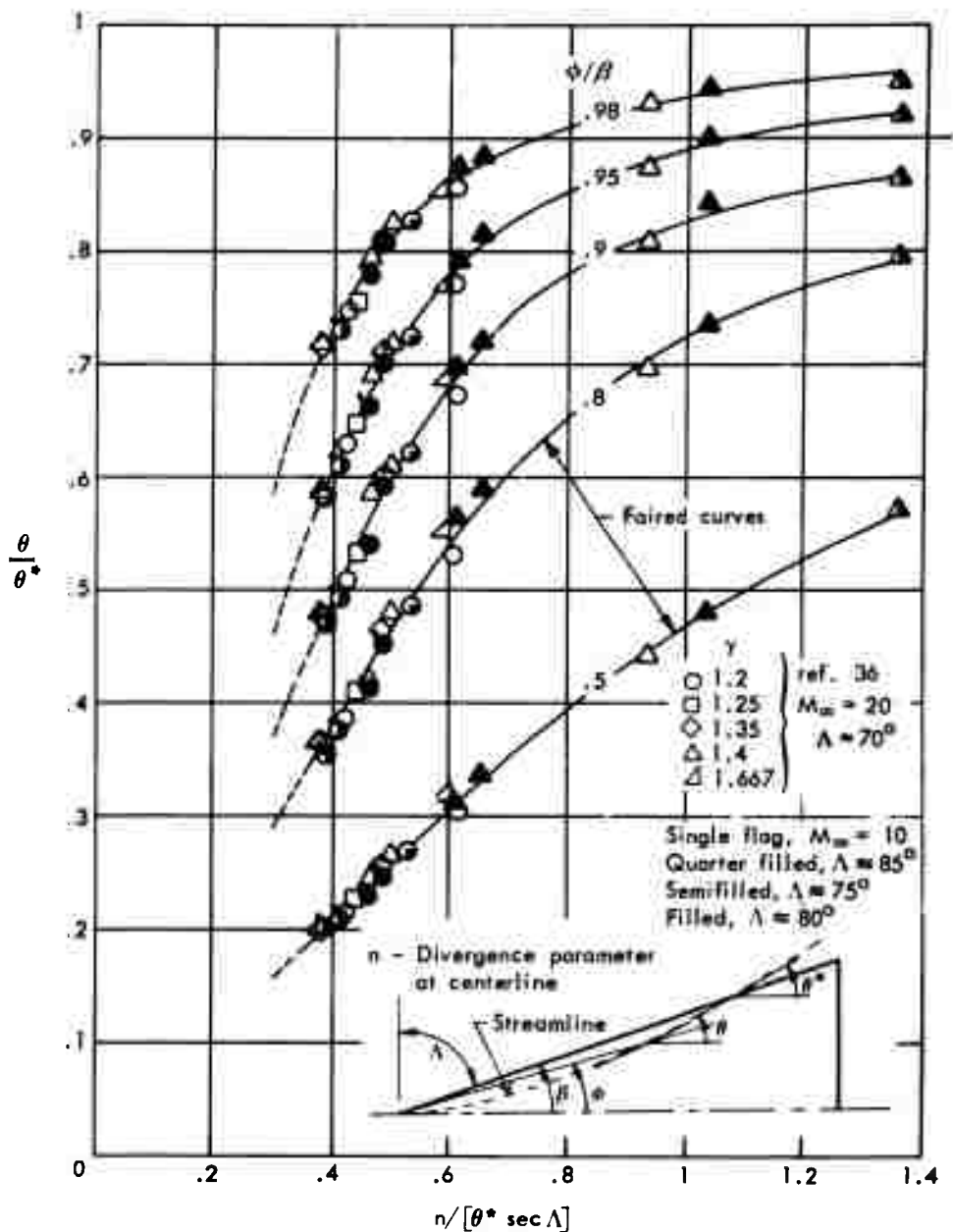


Figure C4: CORRELATION FOR SPANWISE STREAMLINE ANGLES AT HIGH ANGLES OF ATTACK

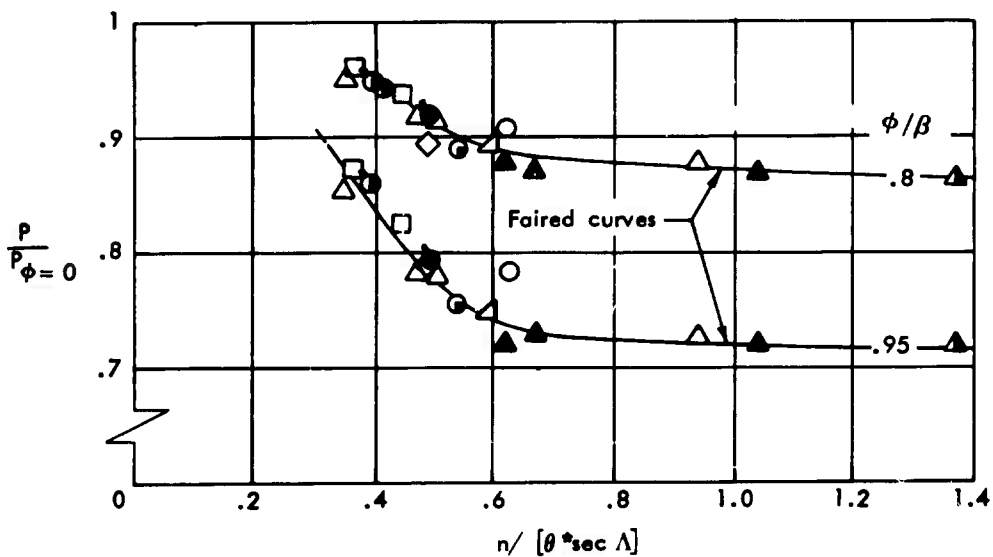
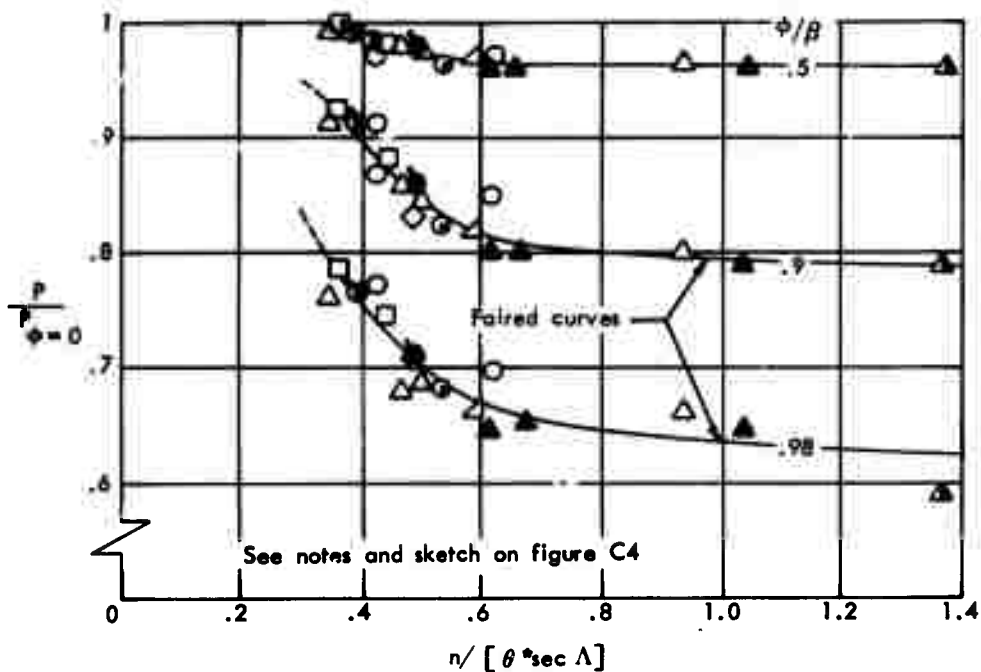
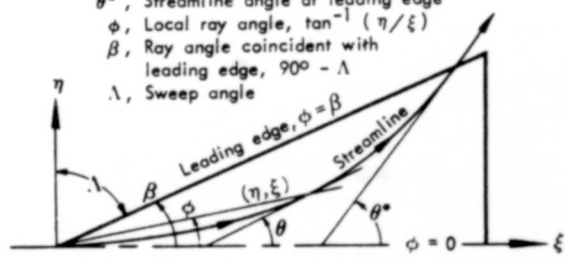


Figure C5: CORRELATION FOR SPANWISE PRESSURE AT HIGH ANGLES OF ATTACK

$\theta$ , Local streamline angle  
 $\theta^*$ , Streamline angle at leading edge  
 $\phi$ , Local ray angle,  $\tan^{-1}(\eta/\xi)$   
 $\beta$ , Ray angle coincident with leading edge,  $90^\circ - \Lambda$   
 $\Lambda$ , Sweep angle



Lower surface flow-field streamline pattern

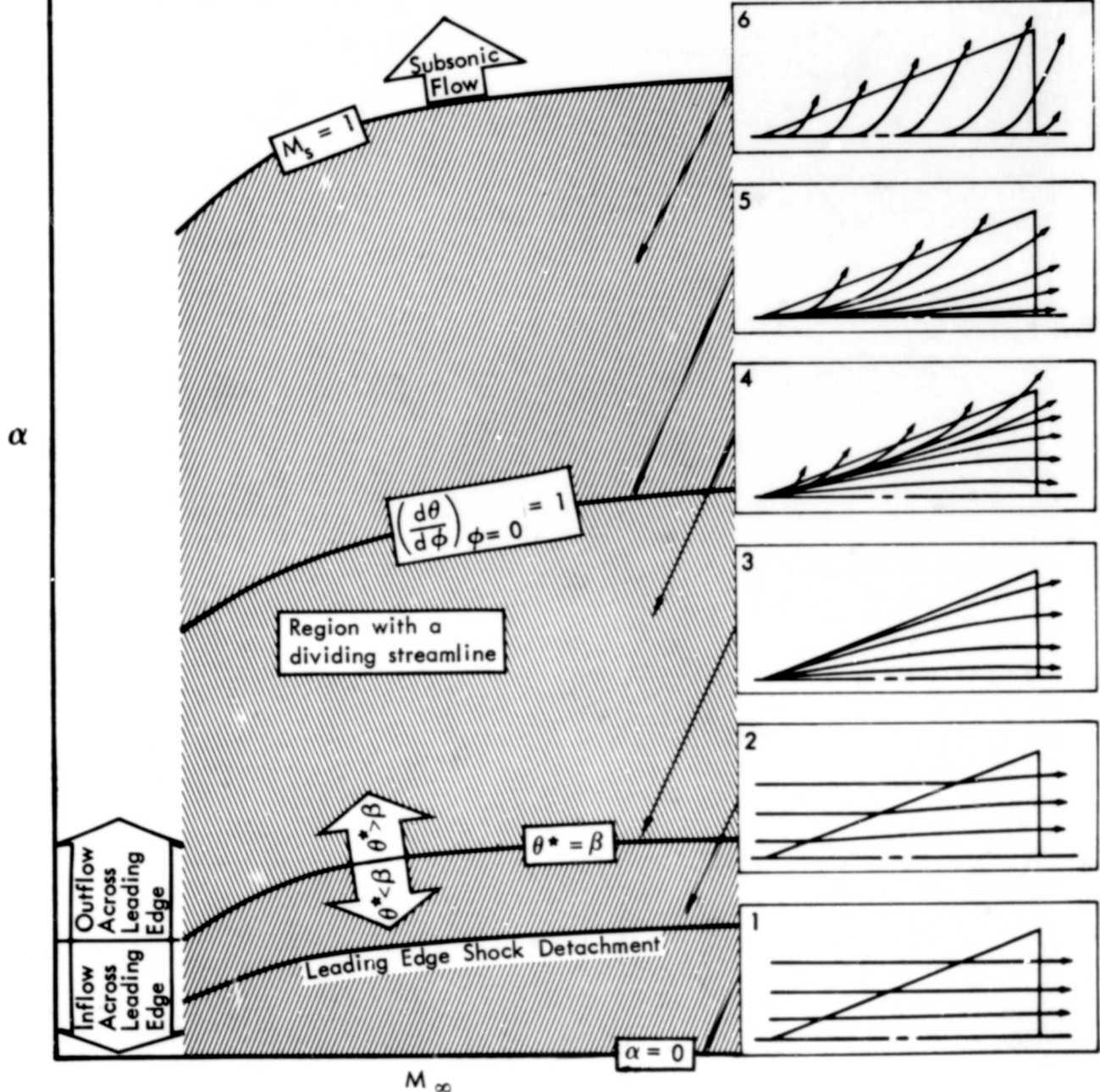


Figure C6: LOWER SURFACE FLOW FIELD REGIMES

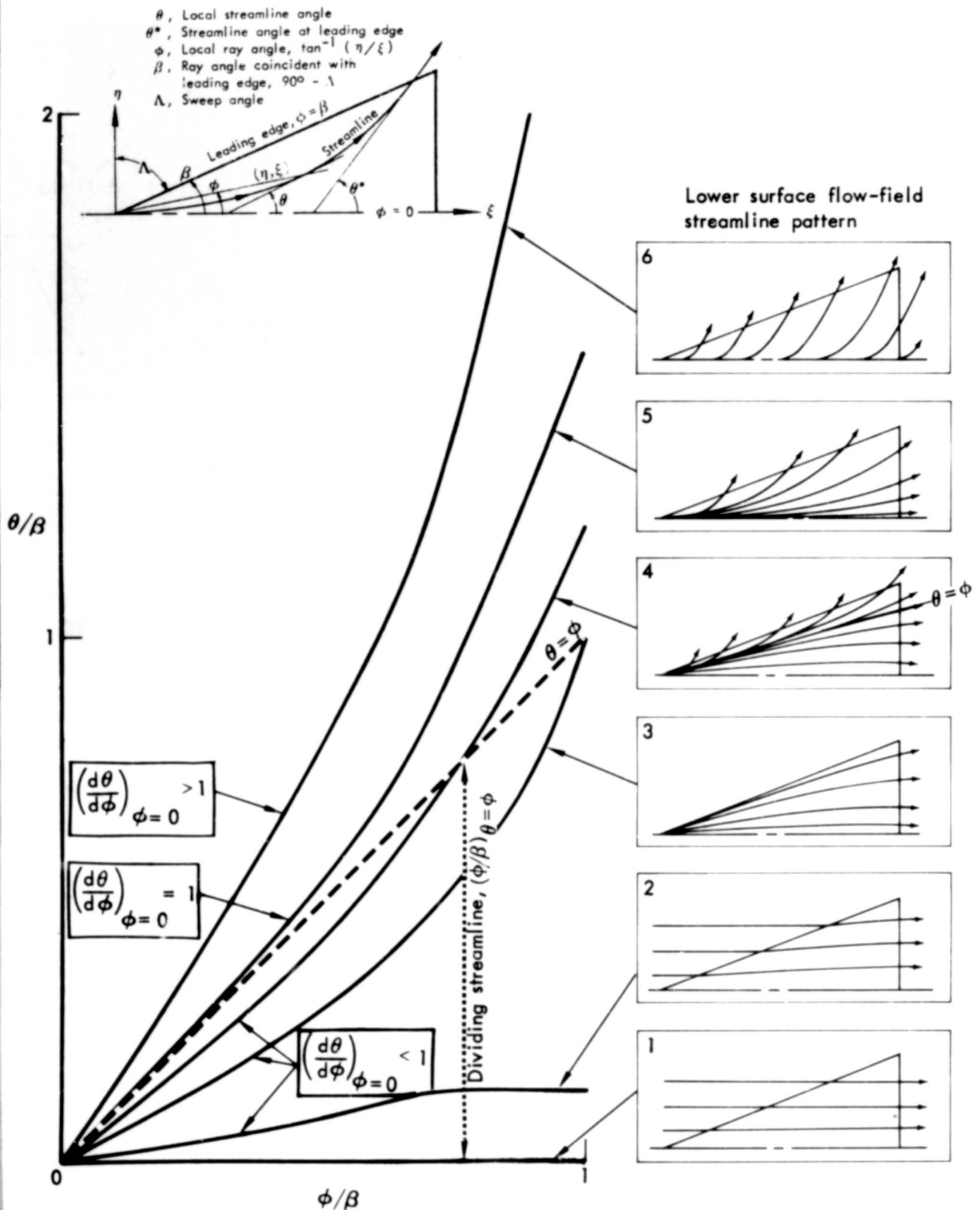


Figure C7: LOWER SURFACE STREAMLINE ANGLE PROFILES

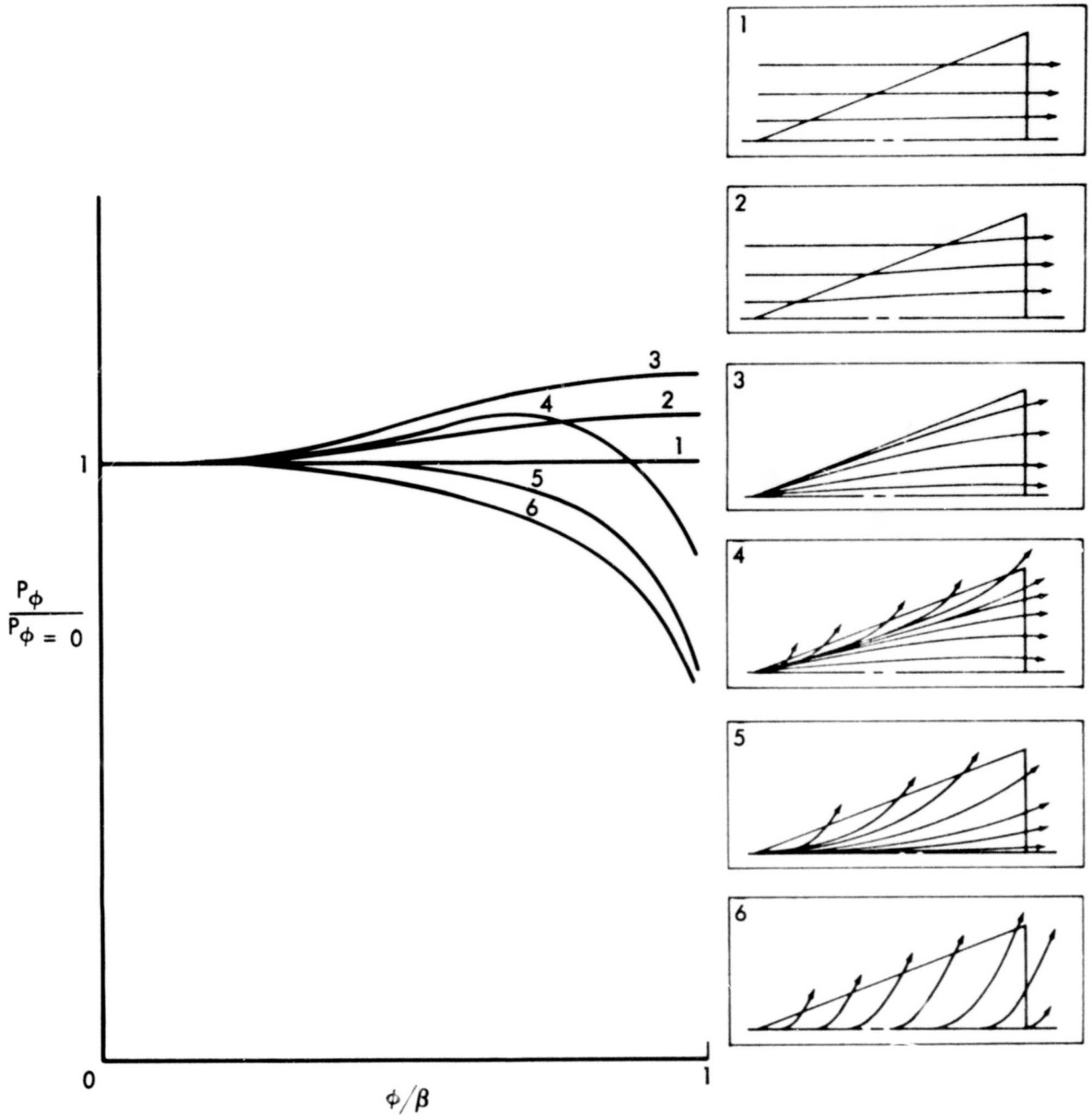


Figure C8: SPANWISE PRESSURE PROFILES

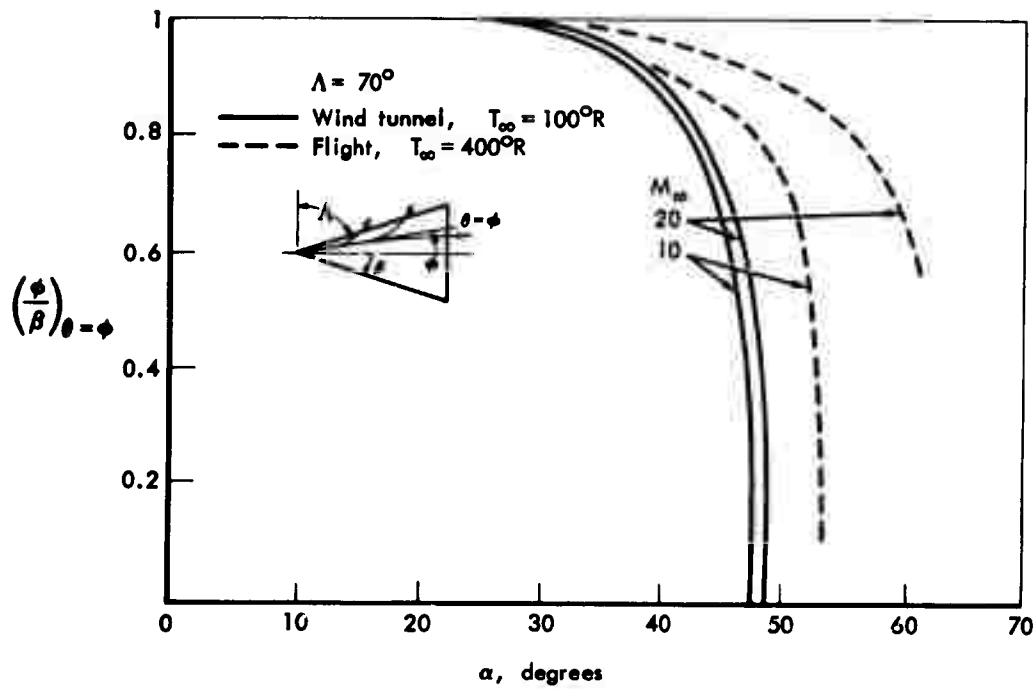


Figure C9: SPANWISE LOCATION OF DIVIDING STREAMLINE

## REFERENCES

1. Nagel, A. L.; and Thomas, A. C.: Analysis of the Correlation of Wind Tunnel and Ground Test Data to Flight Test Results. AIAA Paper No. 65-208, AIAA/NASA Flight Testing Conference, Huntsville, Ala., February 15-17, 1965.
2. Thomas, A. C.; Perlbachs, A.; and Nagel, A. L.: Advanced Reentry Systems Heat Transfer Manual for Hypersonic Flight. AFFDL-TR-65-195, June 1966.
3. Staff of AEDC: Test Facilities Handbook. Arnold Engineering Development Center, July 1963.
4. Experimental Facilities Division, Hypersonic Shock Tunnel: Description and Capabilities. Cornell Aeronautical Laboratory, Inc., October 1964.
5. Glass, I. I.; and Hall, J. Gordon: Handbook of Supersonic Aerodynamics. Section 18 "Shock Tubes." NAVORD Report 1488, Vol. 6, 1955.
6. Fay, J. A.; and Riddell, F. R.: Theory of Stagnation Point Heat Transfer in Dissociated Air. Research Report No. 1, AVCO Research Laboratory, April 1957.
7. Brokaw, R. S.: "The Lewis Number." Progress in International Research on Thermodynamic and Transport Properties. J. F. Masi and D. H. Tsai, editors, ASME and Academic Press, January 1962, pp. 271-287.
8. Hansen, C. Frederick: Approximation for the Thermodynamic and Transport Properties of High Temperature Air. NASA TR-R50, 1959.
9. Gilmore, F. R.: Equilibrium Composition and Thermodynamic Properties of Air to 24,000 °K. The Rand Corp. RM-1543, August 1955.
10. Nagamatsu, H. T.; Workman, J. B.; and Sheer, R. E., Jr.: "Hypersonic Nozzle Expansion of Air with Atom Recombination Present." *JAS*, Vol. 28, No. 11, November 1961.
11. Bray, K. N. C.: "Departure from Dissociation Equilibrium in a Hypersonic Nozzle." *British ARC* 19983, March 1958.
12. Jorgensen, Leland H.; and Baum, Gayle M.: Charts for Equilibrium Flow Properties of Air in Hypersonic Nozzles. NASA TN D-1333, September 1962.
13. Arave, R. J.: Approximate Thermodynamic, Transport, and Electrical Properties of High Temperature Air. Boeing Document D2-11781, January 1963.
14. Giles, H. L.; and Thomas, J. W.: Analysis of Hypersonic Pressure and Heat Transfer Tests on a Flat Plate with a Flap and a Delta Wing with a Body, Elevons, Fins, and Rudders. NASA CR-536, August 1966.

REFERENCES (Continued)

15. Chapman, D. R.: A Theoretical Analysis of Heat Transfer in Regions of Separated Flow. NACA TN-3792, October 1956.
16. Larson, H. K.: Heat Transfer in Separated Flows. IAS Paper No. 59-37, January 1959.
17. Holloway, P. F.; Sterrett, J. R.; and Creekmore, H. S.: An Investigation of Heat Transfer within Regions of Separated Flow at a Mach Number of 6.0. NASA TN D-3074, November 1965.
18. Hanks, R. A.; and Savage, R. T.: Thermal Design Methods for Recoverable Launch Vehicles with Consideration of Arbitrary Wall Temperatures and Surface Conditions. NASA CR-74714, August 1965.
19. Jaeck, C. L.: Analysis of Pressure and Heat Transfer Tests on Surface Roughness Elements with Laminar and Turbulent Boundary Layers. NASA CR-537, August 1966.
20. Bushnell, Dennis M.: Interference Heating on a Swept Cylinder in Region of Intersection with a Wedge at Mach Number 8. NASA TN D-3094, December 1965.
21. Gulbran, C. E.; Redeker, E.; Miller, D. S.; and Strack, S. L.: Heating in Regions of Interfering Flow Fields. Parts II, III, IV and V, AFFDL-TR-65-49, July 1966.
22. Beckwith, Ivan E.: Experimental Investigation of Heat Transfer and Pressure on a Swept Cylinder in the Vicinity of its Intersection with a Wedge and Flat Plate at Mach Number 4.15 and High Reynolds Number. NASA TN D-2020, July 1964.
23. Price, E. A.; Howard, P. W.; and Stallings, R. L., Jr.: Heat-Transfer Measurements on a Flat Plate and Attached Fins at Mach Numbers of 3.51 and 4.44. NASA TN D-2340, June 1964.
24. Jones, Robert A.: Heat-Transfer and Pressure Investigation of a Fin-Plate Interference Model at a Mach Number of 6. NASA TN D-2028, July 1964.
25. Newlander, Robert A.: Effect of Shock Impingement on the Distribution of Heat-Transfer Coefficients on a Right Circular Cylinder at Mach Numbers of 2.65, 3.51, and 4.44. NASA TN D-642, January 1961.
26. Ray, A. D.; and Palko, R. L.: An Investigation of the Effects of Shock Impingement on a Blunt Leading Edge. AEDC-TR-65-153, July 1965.
27. Siler, L. G.; and Deskins, H. E.: Effect of Shock Impingement on the Heat-Transfer and Pressure Distributions on a Cylindrical-Leading-Edge Model at Mach Number 19. AEDC-TDR-64-228, November 1964.
28. Miller, D. S.; and Redeker, E.: "Three-Dimensional Flow Separation." Bumblebee Aerodynamics Panel, Minutes of the 48th Meeting, Johns Hopkins University, Applied Physics Laboratory Report No. TG 14-43, September 1963.

REFERENCES (Continued)

29. Beckwith, Ivan E.; and Cohen, C. B.: Application of Similar Solutions to Calculation of Laminar Heat Transfer on Bodies with Yaw and Large Pressure Gradient in High-Speed Flow. NASA TN D-625, January 1961.
30. Beckwith, Ivan E.; and Gallagher, J. J.: Local Heat Transfer and Recovery Temperatures on a Yawed Cylinder at a Mach Number of 4.15 and High Reynolds Number. NASA Memo 2-27-596, 1959.
31. Chung, P. M.: "Chemically Reacting Nonequilibrium Boundary Layers." *Advances in Heat Transfer*, Vol. II, Academic Press, 1965.
32. Tong, H.: Nonsimilar-Nonequilibrium Boundary Layer Program. Boeing Document D2-23861-1, March 1965.
33. Moore, J. A.; and Pallone, A. J.: Similar Solutions to the Laminar Boundary Layer Equations for Nonequilibrium Air. AVCO RAD-TM-62-59, July 30, 1962.
34. Blottner, F. G.: "Chemical Nonequilibrium Boundary Layer." *AIAA Journal*, Vol. 2, No. 2, February 1964.
35. Kulgein, N. G.: "Heat Transfer from a Nonequilibrium Turbulent Boundary Layer to Catalytic Surfaces." *AIAA Journal*, Vol. 3, No. 2, February 1965.
36. Kennet, Haim: The Inviscid Hypersonic Flow on the Windward Side of a Pointed Lifting Delta Wing. IAS Paper No. 63-55, January 21, 1963.
37. Lees, Lester; and Reeves, B. L.: Supersonic Separated and Reattaching Laminar Flows: I, General Theory and Application to Adiabatic Boundary Layer-Shock Wave Interactions. AIAA Preprint No. 64-4, 1964.
38. Reeves, B. L.: Separated Flow Solutions by Integral Techniques. AFFDL-TDR-63-4140, August 1965.
39. Cohen, Clarence B.; and Reshotko, Eli: Similar Solutions for the Compressible Laminar Boundary Layer with Heat Transfer and Pressure gradient. NACA Report 1293, 1956.
40. Hayes, W. D.; and Probstein, R. F.: Hypersonic Flow Theory. Academic Press, 1959.
41. Shapiro, A. H.: The Dynamics and Thermodynamics of Compressible Fluid Flow. Vol. I, The Ronald Press, 1953.
42. Nagel, A. L.; Fitzsimmons, H. D.; and Doyle, L. B.: Analysis of Hypersonic Pressure and Heat Transfer Tests on Delta Wings with Laminar and Turbulent Boundary Layers. NASA CR-535, August 1966.
43. Data Report — BHWT Test No. 044 on the AD-483M-1 Parametric Model for the Dyna Soar Program, To Study the Effect of Sweepback on Heat Transfer and Pressure Distribution at  $M = 6.1$ . Boeing Document D2-80049, September 1961.

REFERENCES (Concluded)

44. Cornelius, James R.: AEDC Tunnel B, Boeing Company Test No. 15, Mach 8 Heat Transfer and Pressure Test on AD-477M-1, A 73-Degree Sweepback Delta Wing Bi-Radial Leading Edge Research Model. Boeing Document D2-8206, May 1961.

UNCLASSIFIED

Security Classification

DOCUMENT CONTROL DATA - R&D

(Security classification of title, body of abstract and indexing annotation must be entered when the overall report is classified)

1 ORIGINATING ACTIVITY (Corporate author) The Boeing Company Seattle, Washington		2a REPORT SECURITY CLASSIFICATION <b>Unclassified</b>
2b GROUP		
3 REPORT TITLE <b>APPLICATION OF GROUND TEST DATA TO REENTRY VEHICLE DESIGN</b>		
4 DESCRIPTIVE NOTES (type of report and inclusive dates) <b>Final Report, June 1965 to December 1966</b>		
5 AUTHOR(S) (Last name, first name, initial) <b>Thomas, Alfred C. Perlbachs, Andrew</b>		
6 REPORT DATE <b>January 1967</b>	7a TOTAL NO. OF PAGES <b>xiv + 122</b>	7b NO. OF REFS <b>44</b>
8a CONTRACT OR GRANT NO. <b>AF33(615)-2516</b>	9a ORIGINATOR'S REPORT NUMBER(S) <b>AFFDL-TR-66-229</b>	
b PROJECT NO. <b>1366</b>	9b OTHER REPORT NO(S) (Any other numbers that may be assigned this report)	
c Task: <b>136607</b>		
d BPSN5(61136607-62405334)		
10 AVAILABILITY/LIMITATION NOTICES <b>Distribution of this document is unlimited.</b>		
11 SUPPLEMENTARY NOTES	12 SPONSORING MILITARY ACTIVITY <b>Air Force Flight Dynamics Laboratory Research and Technology Division Wright-Patterson Air Force Base, Ohio 45433</b>	
13 ABSTRACT <p>Methods and procedures have been developed for extrapolating ground-test aerothermodynamic data to flight conditions for four geometric elements. These elements are a sharp unyawed delta wing, deflected control surfaces in compression and expansion, surface roughness elements typified by shallow convex surface waves and rectangular grooves, and a yawed circular cylinder intersecting a sharp flat plate. Graphs and charts are provided for rapid numerical computation of factors to be used in extrapolating the wind-tunnel data for these geometric elements to flight conditions. An evaluation of the simulation capabilities of operational hypersonic ground facilities is also included.</p>		

UNCLASSIFIED

Security Classification

14 KEY WORDS	LINK A		LINK B		LINK C	
	ROLE	WT	ROLE	WT	ROLE	WT
Heat-Transfer Data Extrapolation Factors						
Ground-Facility Simulation Capability						
Real-Gas Effects						
Chemical Nonequilibrium Effects						
Sharp Delta-Wing Flow Fields						

INSTRUCTIONS

1. **ORIGINATING ACTIVITY:** Enter the name and address of the contractor, subcontractor, grantee, Department of Defense activity or other organization (corporate author) issuing the report.

2a. **REPORT SECURITY CLASSIFICATION:** Enter the overall security classification of the report. Indicate whether "Restricted Data" is included. Marking is to be in accordance with appropriate security regulations.

2b. **GROUP:** Automatic downgrading is specified in DoD Directive 5200.10 and Armed Forces Industrial Manual. Enter the group number. Also, when applicable, show that optional markings have been used for Group 3 and Group 4 as authorized.

3. **REPORT TITLE:** Enter the complete report title in all capital letters. Titles in all cases should be unclassified. If a meaningful title cannot be selected without classification, show title classification in all capitals in parenthesis immediately following the title.

4. **DESCRIPTIVE NOTES:** If appropriate, enter the type of report, e.g., interim, progress, summary, annual, or final. Give the inclusive dates when a specific reporting period is covered.

5. **AUTHOR(S):** Enter the name(s) of author(s) as shown on or in the report. Enter last name, first name, middle initial. If military, show rank and branch of service. The name of the principal author is an absolute minimum requirement.

6. **REPORT DATE:** Enter the date of the report as day, month, year, or month, year. If more than one date appears on the report, use date of publication.

7. **TOTAL NUMBER OF PAGES:** The total page count should follow normal pagination procedures, i.e., enter the number of pages containing information.

7b. **NUMBER OF REFERENCES:** Enter the total number of references cited in the report.

8a. **CONTRACT OR GRANT NUMBER:** If appropriate, enter the applicable number of the contract or grant under which the report was written.

8b, 8c, & 8d. **PROJECT NUMBER:** Enter the appropriate military department identification, such as project number, subproject number, system numbers, task number, etc.

9a. **ORIGINATOR'S REPORT NUMBER(S):** Enter the official report number by which the document will be identified and controlled by the originating activity. This number must be unique to this report.

9b. **OTHER REPORT NUMBER(S):** If the report has been assigned any other report numbers (either by the originator or by the sponsor), also enter this number(s).

10. **AVAILABILITY LIMITATION NOTICES:** Enter any limitations on further dissemination of the report, other than those imposed by security classification, using standard statements such as:

- (1) "Qualified requesters may obtain copies of this report from DDC."
- (2) "Foreign announcement and dissemination of this report by DDC is not authorized."
- (3) "U.S. Government agencies may obtain copies of this report directly from DDC. Other qualified DDC users shall request through \_\_\_\_\_."
- (4) "U.S. military agencies may obtain copies of this report directly from DDC. Other qualified users shall request through \_\_\_\_\_."
- (5) "All distribution of this report is controlled. Qualified DDC users shall request through \_\_\_\_\_."

If the report has been furnished to the Office of Technical Services, Department of Commerce, for sale to the public, indicate this fact and enter the price, if known.

11. **SUPPLEMENTARY NOTES:** Use for additional explanatory notes.

12. **SPONSORING MILITARY ACTIVITY:** Enter the name of the departmental project office or laboratory sponsoring (paying for) the research and development. Include address.

13. **ABSTRACT:** Enter an abstract giving a brief and factual summary of the document indicative of the report, even though it may also appear elsewhere in the body of the technical report. If additional space is required, a continuation sheet shall be attached.

It is highly desirable that the abstract of classified reports be unclassified. Each paragraph of the abstract shall end with an indication of the military security classification of the information in the paragraph, represented as (TS), (S), (C), or (U).

There is no limitation on the length of the abstract. However, the suggested length is from 150 to 225 words.

14. **KEY WORDS:** Key words are technically meaningful terms or short phrases that characterize a report and may be used as index entries for cataloging the report. Key words must be selected so that no security classification is required. Identifiers, such as equipment model designation, trade name, military project code name, geographic location, may be used as key words but will be followed by an indication of technical context. The assignment of links, roles, and weights is optional.